Max-Planck-Institut für Kolloid- und Grenzflächenforschung

Fragments of the Human Antimicrobial LL-37 and their Interaction with Model Membranes

Dissertation

zur Erlangung des akademischen Grades

doctor rerum naturalium

(Dr. rer. nat.)

in der Wissenschaftsdisziplin

Biophysik

eingereicht an der

Mathematisch-Naturwissenschaftlichen Fakultät

der Universität Potsdam

von

Claudia Dannehl

Potsdam, Mai 2013

Published online at the
Institutional Repository of the University of Potsdam:
URL http://opus.kobv.de/ubp/volltexte/2013/6814/
URN urn:nbn:de:kobv:517-opus-68144
http://nbn-resolving.de/urn:nbn:de:kobv:517-opus-68144

In Erinnerung an Dr. Olaf Zschörnig

Summary

A detailed description of the characteristics of antimicrobial peptides (AMPs) is highly demanded, since the resistance against traditional antibiotics is an emerging problem in medicine. They are part of the innate immune system in every organism, and they are very efficient in the protection against bacteria, viruses, fungi and even cancer cells. Their advantage is that their target is the cell membrane, in contrast to antibiotics which disturb the metabolism of the respective cell type. This allows AMPs to be more active and faster. The lack of an efficient therapy for some cancer types and the evolvement of resistance against existing antitumor agents make AMPs promising in cancer therapy besides being an alternative to traditional antibiotics.

The aim of this work was the physical-chemical characterization of two fragments of LL-37, a human antimicrobial peptide from the cathelicidin family. The fragments LL-32 and LL-20 exhibited contrary behavior in biological experiments concerning their activity against bacterial cells, human cells and human cancer cells. LL-32 had even a higher activity than LL-37, while LL-20 had almost no effect. The interaction of the two fragments with model membranes was systematically studied in this work to understand their mode of action. Planar lipid films were mainly applied as model systems in combination with IR-spectroscopy and X-ray scattering methods. Circular Dichroism spectroscopy in bulk systems completed the results.

In the first approach, the structure of the peptides was determined in aqueous solution and compared to the structure of the peptides at the air/water interface. In bulk, both peptides are in an unstructured conformation. Adsorbed and confined to at the air-water interface, the peptides differ drastically in their surface activity as well as in the secondary structure. While LL-32 transforms into an α-helix lying flat at the water surface, LL-20 stays partly unstructured. This is in good agreement with the high antimicrobial activity of LL-32.

In the second approach, experiments with lipid monolayers as biomimetic models for the cell membrane were performed. It could be shown that the peptides fluidize condensed monolayers of negatively charged DPPG which can be related to the thinning of a bacterial cell membrane. An interaction of the peptides with zwitterionic PCs, as models for mammalian cells, was not clearly observed, even though LL-32 is haemolytic.

In the third approach, the lipid monolayers were more adapted to the composition of human erythrocyte membranes by incorporating sphingomyelin (SM) into the PC monolayers. Physical-chemical properties of the lipid films were determined and the influence of the peptides on them was studied. It could be shown that the interaction of the more active LL-32 is strongly increased for heterogeneous lipid films containing both gel and fluid phases, while the interaction of LL-20

with the monolayers was unaffected. The results indicate an interaction of LL-32 with the membrane in a detergent-like way.

Additionally, the modelling of the peptide interaction with cancer cells was performed by incorporating some negatively charged lipids into the PC/SM monolayers, but the increased charge had no effect on the interaction of LL-32. It was concluded, that the high anti-cancer activity of the peptide originates from the changed fluidity of cell membrane rather than from the increased surface charge. Furthermore, similarities to the physical-chemical properties of melittin, an AMP from the bee venom, were demonstrated.

Zusammenfassung

Aufgrund der steigenden Resistenzen von Zellstämmen gegen traditionelle Therapeutika sind alternative medizinische Behandlungsmöglichkeiten für bakterielle Infektionen und Krebs stark gefragt. Antimikrobielle Peptide (AMPs) sind Bestandteil der unspezifischen Immunabwehr und kommen in jedem Organismus vor. AMPs lagern sich von außen an die Zellmembran an und zerstören ihre Integrität. Das macht sie effizient und vor allem schnell in der Wirkung gegen Bakterien, Viren, Pilzen und sogar Krebszellen.

Das Ziel dieser Arbeit lag in der physikalisch-chemischen Charakterisierung zweier Peptidfragmente die unterschiedliche biologische Aktivität aufweisen. Die Peptide LL-32 und LL-20 waren Teile des humanen LL-37 aus der Kathelizidin-Familie. LL-32 wies eine stärke Aktivität als das Mutterpeptid auf, während LL-20 kaum aktiv gegen die verschiedenen Zelltypen war. In dieser Arbeit wurde die Wechselwirkung der Peptide mit Zellmembranen systematisch anhand von zweidimensionalen Modellmembranen in dieser Arbeit untersucht. Dafür wurden Filmwaagenmessungen mit IR-spektroskopischen und Röntgenstreumethoden gekoppelt. Circulardichroismus-Spektroskopie im Volumen komplementierte die Ergebnisse.

In der ersten Näherung wurde die Struktur der Peptide in Lösung mit der Struktur an der Wasser/Luft-Grenzfläche verglichen. In wässriger Lösung sind beide Peptidfragmente unstrukturiert, nehmen jedoch eine α-helikale Sekundärstruktur an, wenn sie an die Wasser/Luft-Grenzfläche adsorbiert sind. Das biologisch unwirksamere LL-20 bleibt dabei teilweise ungeordnet. Das steht im Zusammenhang mit einer geringeren Grenzflächenaktivität des Peptids.

In der Zweiten Näherung wurden Versuche mit Lipidmonoschichten als biomimetisches Modell für die Wechselwirkung mit der Zellmembran durchgeführt. Es konnte gezeigt werden, dass sich die Peptide fluidisierend auf negativ geladene Dipalmitylphosphatidylglycerol (DPPG) Monoschichten auswirken, was einer Membranverdünnung an Bakterienzellen entspricht. Eine Interaktion der Peptide mit zwitterionischem Phosphatidylcholin (PC), das als Modell für Säugetierzellen verwendet wurde, konnte nicht klar beobachtet werden, obwohl biologische Experimente das hämolytische Verhalten zumindest von LL-32 zeigten.

In der dritten Näherung wurde das Membranmodell näher an die Membran von humanen Erythrozyten angepasst, indem gemischte Monoschichten aus Sphingomyelin (SM) und PC hergestellt wurden. Die physikalisch-chemischen Eigenschaften der Lipidfilme wurden zunächst ausgearbeitet und anschließend der Einfluss der Peptide untersucht. Es konnte anhand verschiedener Versuche gezeigt werden, dass die Wechselwirkung von LL-32 mit der Modellmembran verstärkt ist, wenn eine Koexistenz von fluiden und Gelphasen auftritt.

Zusätzlich wurde die Wechselwirkung der Peptide mit der Membran von Krebszellen imitiert, indem ein geringer Anteil negativ geladener Lipide in die Monoschicht eingebaut wurde. Das hatte allerdings keinen nachweislichen Effekt, so dass geschlussfolgert werden konnte, dass die hohe Aktivität von LL-32 gegen Krebszellen ihren Grund in der veränderten Fluidität der Membran hat und nicht in der veränderten Oberflächenladung. Darüber hinaus wurden Ähnlichkeiten zu Melittin, einem AMP aus dem Bienengift, dargelegt. Die Ergebnisse dieser Arbeit sprechen für einen Detergenzien-artigen Wirkmechanismus des Peptids LL-32 an der Zellmembran.

Content

1 Introduction 15

1.1 Cell Membranes 15

1.1.1 Mammalian Cells 15

1.1.2 Cancer Cells 16

1.1.3 Bacteria Cells 16

1.2 Modeling of Cell Membranes 16

1.2.1 Phase Behavior of Lipids 17

1.3 Antimicrobial Peptides 18

1.3.1 Anti-Cancer Effects of AMPs 19

1.3.2 Antimicrobial Peptide Resistance 19

1.3.3 Amphipathic, Cationic, α-helical Antimicrobial Peptides 20

1.3.4 hCAP18/ LL-37 21

1.4 Motivation of this Work 23

1.4.1 Fragments of LL-37 Used in this Work 24

2 Methods and Materials 27

2.1 Circular Dichroism Spectroscopy 27

2.1.1 Estimation of the Secondary Structure 27

2.2 Langmuir Film Balance 28

2.3 InfraRed Reflection Absorption Spectroscopy (IRRAS) 29

2.4 Surface Sensitive X-ray Scattering 33

2.4.1 Grazing-Incidence X-ray Diffraction (GIXD) 33

2.4.2 X-ray Reflectivity (XR) 35

2.5 Chemicals and Sample Preparation 35

3 Surface Activity and Structures of the Two Peptides 37

Abstract 37

3.1 Peptides in Water 38

3.2 Peptides at the Air/water Interface 38

3.2.1 Infrared Reflection Absorption Spectroscopy (IRRAS) 39

3.2.2 X-Ray Reflectivity 41

3.3 Discussion 43

4 The Influence of the Peptides on Lipid Monolayers 45

Abstract 45
4.1 Interaction of the Peptides with Lipid Monolayers 46
4.1.1 Interaction with Pre-Compressed Monolayers: the Fluid Phase is Preferred 46
4.1.1.1 Maximum Insertion Pressure Measurements 46
4.1.1.2 Infrared-Reflection-Absorption Spectroscopy with LL-32 49
4.1.2 Interaction of LL-32 and LL-20 with Uncompressed Monolayers: 52
Condensation and Fluidization are Key Effects 52
4.1.2.1 Infrared-Reflection-Absorption Spectroscopy 53
4.1.2.2 Grazing Incidence X-ray Diffraction 57
4.1.2.3 Specular X-Ray Reflectivity 58
4.2 Comparison to Measurements in Bulk 61
4.3 Discussion 62
5 Peptide Interaction with Mixed Lipid Monolayers Containing Sphingomyelin 65
Abstract 65
5.1 Characterization of the Mixed Lipid Films 66
5.1.1 SM Influences the DPPC Phase Transition 66
5.1.1.1 IRRAS 67
5.1.1.2 GIXD 67
5.1.2 Incorporation of 10 mol % DOPS Reduces Strong Packing 68
5.2 Influence on the Peptide Interaction 70
5.2.1 How SM and DOPS Incorporation into DPPC Monolayers Influence the Interaction with the Peptides 70
5.2.1.1 GIXD 72
5.2.1.2 Injection under Pre-Compressed Monolayers: Dependence on the Lipid Phase State 73
5.2.2 SM Addition to Fluid DOPC Monolayers Has no Effect on the Peptide Interaction 74
5.2.2.1 IRRAS 75
5.2.2.2 Injection Under Pre-compressed Monolayers 75
5.3 Discussion 76
5.3.1 Structure of the Lipid Films 76
5.3.2 Influence of SM and DOPS on the Peptide Interaction 78
6 General Discussion/Conclusion 81

6.1 Peptides at the Air/water Interface 81
6.2 Interaction of the Peptides with Vesicles 82
6.3 Interaction of the Peptides with Lipid Monolayers 83
6.4 Interaction of the Peptides with Mixed Lipid Monolayers Containing SM and DOPS 84
6.5 Similiarities of LL-32 and LL-37 to Melittin 87
7 References 89
VIII. Appendix 107
VIII.1 Simulation of LL-32 at the Air/water Interface 107
VIII.2 Secondary Structure Calculation with DICHROWEB 108
VIII.3 Effect of SDS and CTAB on LL-20 and LL-32 109
VIII.4 Isotherms 111
VIII.5 GIXD Data and Calculated Lattice Parameters 112
VIII.6 IRRA Spectra 119
Danksagung 123
Eigenständigkeitserklärung 125

Abbreviations

AMP	antimicrobial peptide
Chol	cholesterol
CAP, CAP18	cathelicidin antimicrobial peptide
CTAB	cetyl trimethyl ammonium bromide
cmc	critical micelle concentration
DMPA	1,2-dimyristoyl-*sn*-glycero-3-phosphate
DMPC	1,2-dimyristoyl-*sn*-glycero-3-phosphocholine
DOPC	1,2-dioleoyl-*sn*-glycero-3-phosphocholine
DOPS	1,2-dioleoyl-*sn*-glycero-3-phospho-L-serine
DPPC	1,2-dipalmitoyl-sn-glycero-3-phosphocholine
DPPG	1,2-dipalmitoyl-sn-glycero-3-phosphoglycerol
EP	Exclusion Pressure
HEPES	N-2-hydroxyethyl-piperazin-N'-2-ethansulfonic acid
hCAP18	human cathelicidin antimicrobial peptide
GUV	giant unilamellar vesicles
Fmoc	fluorenylmethoxycarbonyl
LC	(liquid-) condensed
LE	(liquid-) expanded
LPS	lipopolysaccharide
MIP	Maximum Insertion Pressure
NN	nearest neighbor
NNN	next-nearest neighbor
PE	phosphatidylethanolamine
PC	phosphatidylcholine
PG	phosphatidylglycerol
PS	phosphatidylserine
POPC	1-palmitoyl-2-oleoyl-***sn***-glycero-3-phosphocholine
POPG	1-palmitoyl-2-oleoyl-***sn***-glycero-3-phosphoglycerol
p-polarized	parallel polarized
PS	phosphatidylphoserine
RA	reflection-absorption
R, R_0	single beam spectrum of the sample and the reference trough, respectively
SDS	sodium dodecyl sulfate

SM	sphingomyelin
s-polarized	vertical polarized

Physical quantities

A	area
A_0	cross-sectional area of an aliphatic chain
A_{xy}	projected in-plane area of an aliphatic chain
a, b, c	cell vectors of the primitive unit cell
h, k, l	Miller indices
FWHM	full-width-at-half-maximum
ΔG	change in Gibbs free energie
ΔG_{wif}	free energy of transfer from water to POPC interface
$\boldsymbol{k}$	reciprocal scattering vector
L_{xy}	in-plane correlation length
L_z	thickness of the diffracted layer
mH, mH_{rel}	mean hydrophobic moment, and normalized to a perfect amphipathic helix, respectively
Q_{xy}	in-plane scattering vector
Q_z	out-of-plane scattering vector
t	time
T	temperature
w	width
z	vertical distance from the interface
[θ]	mean molar ellipiticity
ν	stretching vibration
π	surface pressure
π_{eq}	equilibrium surface pressure
π_i	initial surface pressure
$\Delta\pi$	change in surface pressure
ρ	electron density
σ	surface tension

Methods

AFM	Atomic Force Microscopy
CD	Circular Dichroism

DSC	Differential Scanning Calorimetry
ESR	Electron Spin Resonance
FRET	Förster Resonance Energy Transfer
FT-IR	Fourier Transform-Infrared Spectroscopy
IRRAS	Infrared Reflection Absorption Spectroscopy
GIXD	Grazing Incidence X-ray Diffraction
SAXS	Small Angle X-ray Scattering
XR	X-ray Reflectivity

1 Introduction

1.1 Cell Membranes

The cell membrane is a highly dynamic barrier. It protects the cell compartments from the environment and is involved in signaling, communication, solute transport, DNA replication, cell-cell recognition, secretion and is a target of drugs, hormones and proteins [1-3]. Natural membranes contain a mixture of more than thousand different lipids and proteins [4]. They are arranged in a bilayer with an asymmetric contribution. This bilayer can be considered as a two dimensional solution of lipids and proteins, whose components can freely diffuse and flip-flop [5] (Figure 1).

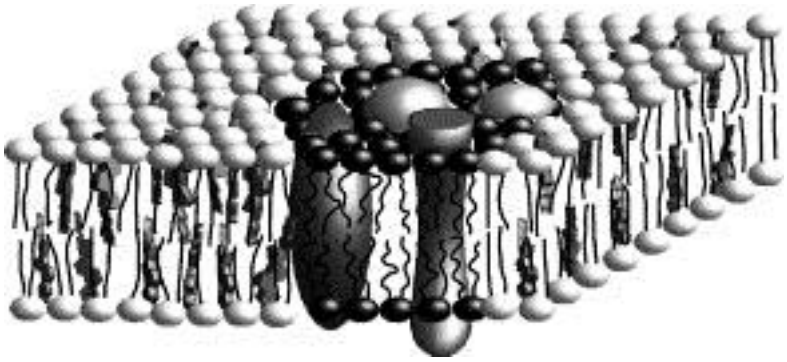

Figure 1: Schematic representation of a biological membrane. The lipids are mainly in the L_d phase. Dispersed L_o domains, where integral and peripheral proteins partition preferentially, form rafts. Adapted from [6].

Based on the miscibility gap in phase diagrams of some lipids [6], the fluid-mosaic-model was extended to a raft-model [7-10]. Especially cholesterol, glycosphingolipids and some membrane proteins form transient, co-existing, small (50 nm in diameter), dynamic, liquid-ordered microdomains in the liquid-disordered environment. These so-called rafts are involved in many biochemical processes. They influence the membrane fluidity and the trafficking of membrane proteins, and regulate different cellular processes such as neurotransmission and receptor trafficking. [11] Also, many viral pathogen infections and inflammations take place at the site of lipid rafts (a review can be found in [12]).

1.1.1 Mammalian Cells

Two major components of mammalian cells are phosphatidylcholines (PCs) and sphingolipids [13]. Together they make more than 80% of the total lipid amount in the outer leaflet [14]. 30% of the total lipid amount is the sphingolipid spingomyelin (SM) [15]. SM carries like PC a

phosphocholine head group, but has a sphingosine backbone which is connected with the fatty acid via an amide bond. While PC has only H-bond acceptors, SM has both, H-donors and -acceptors, so it can form as well inter- and intramolecular hydrogen bonds [16; 17]. Other important components are cholesterol, phosphatidylethanolamine (PE) and phoshphatidylserine (PS). PE and PS are restricted to the inner leaflet [18].

1.1.2 Cancer Cells

Beside the increased elasticity of the whole cell [19], cancer cell membranes have no bilayer asymmetry and contain an increased level of negatively charged PS in the outer leaflet of the membrane [20; 21]. The increased PS content usually triggers apoptosis, which is somehow circumvented by cancer cells [22]. A PS content of 10% was found in the outer leaflet of leukemia cells, which is 10 times higher compared to lymphocytes [23]. Tumor cell membranes are more fluid and have an increased cell surface area compared to healthy cells. Also, some cancer cell types contain an increased amount of cholesterol and cholesterol-rich rafts [22].

1.1.3 Bacteria Cells

Bacterial membranes are composed mainly of negatively charged phosphatidylglycerols (PG) and cardiolipin (CL) [23; 24]. In *Staphylococcus aureus*, the PG content is up to 80% [25] while in *Escherichia coli* it is only 15%. From zwitterionic lipids, phosphatidylethanolamine (PE) is the most prominent lipid in bacterial membranes. The membrane is surrounded by a peptidoglycan layer. But bacteria must be divided into two groups: Gram-negative and Gram-positive bacteria. The membrane of these two types differs in composition. The membrane of Gram-positive is rich in lipoteichoic acids (LTA). The membrane of Gram-negative bacteria is more complex, because it is composed of two bilayers. The outer membrane contains mainly lipopolysaccharides (LPS) in the outer leaflet [26].

1.2 Modeling of Cell Membranes

From the mixture of components within the membrane, it is not possible to get insight into the interaction with peptides or proteins on the molecular level. Using membrane models reduces the interaction partners to a few defined lipid species. Several membrane models with both, advantages and limitations exist. Lipid vesicles are one possibility, because the curvature can correspond to a shape of a cell, but it is difficult to control the lipid phase state in the membrane and the lipid composition exposed to the medium in mixtures in unknown [27]. Biological membranes can be considered as two weakly coupled monolayers [28; 29]. By using lipid

monolayers, the dependence on the curvature can be eliminated [30], which can influence peptide binding properties. Experiments with lipid monolayers are the first step in understanding the interaction of peptides with membranes [31-35]. The surface pressure, lipid packing and the area per lipid can be controlled additionally to the subphase composition and the temperature. Before interacting with the bilayer core, peptides have to adsorb to the lipid interface [36], to the head group region, to be more precise. So a lipid monolayer is a good approach to investigate the transition from solution to the membrane interface. This model can be more simplified, with the bare air/water interface. It is the simplest model to investigate peptide-membrane interactions with absence of lipid charges, since the interface to the membrane can be regarded as an interface between a hydrophilic and a hydrophobic environment. The hydrophobic effect is a main motif in inducing an ordered structure in a peptide [1]. Natural phospholipids have one or two double bonds in the aliphatic region. These generally create disorder and reduce the transition temperatures for bilayers, equivalently the transition pressures for Langmuir monolayers [29]. There is a direct relation between the lateral pressure in a membrane and lipid monolayers. This was found to be 30…35 mN/m [37; 38]. The disadvantage of using monolayers is that processes involving the complete bilayer, like membrane spanning or pore formation, cannot be followed.

An overview of other membrane models can be found in reviews [39; 40]. Beside vesicles and lipid monolayers, supported and tethered bilayers are common models for a cell membrane, but they were not used in this study.

1.2.1 Phase Behavior of Lipids

The phase behavior of the lipids (Figure 2) depends on parameters like the head group size, its ability to form hydrogen bonds, the length and saturation of the fatty acid chains, the presence of counterions, and the temperature. The most rigid structure, which can be found in a natural membrane, is the *gel* (*solid-ordered*) *phase* S_o (*untilted* L_β or *tilted* $L_{\beta'}$) with an all-trans configuration of the chains which allows a strong packing. Upon heating, solid-ordered lipids melt at T_m to a *fluid* (*liquid-disordered*) *phase* L_d. This phase is rich in trans-gauche isomerized chains, creating a chain disorder in the packing. A kind of mixture of these phases is the *liquid-ordered phase* L_o. The conformational order corresponds more to the S_o phase, but the lateral and rotational diffusion is more similar to the L_d phase [40]. Incorporation of cholesterol or lipids with saturated chains can promote the L_d phase.

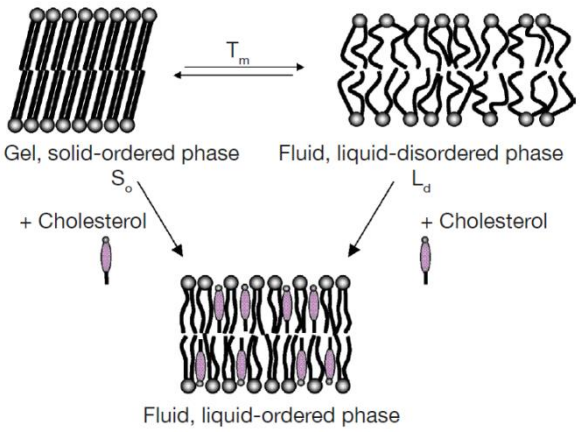

Figure 2: Schematic representation of the most relevant lipid phases in bilayers, taken from [40].

Immisicibility of two components leads to a phase separation which results in coexistence of two phases and domain formation. The phase behavior of lipids is highly investigated for PC/SM/Chol mixtures, since this mixture is prominent for lipid rafts [7; 8; 10]. Lipid domains can be described as fluctuations near the critical miscibility point within the membrane [41-43]. These fluctuations occur over a correlation length ξ, both above and below the critical temperature T_c. If T approaches T_c,

$$\xi \approx |T - Tc|^{-\nu} \tag{1}$$

with ν being the critical exponent. For $T<T_c$, domain boundaries fluctuate. If T approaches T_c from below, the composition of the two phases becomes similar until they coincide at the critical point, meaning that the order parameter $m \rightarrow 0$, which is defined by

$$m \approx |Tc - T|^{\beta}. \tag{2}$$

Also, at the critical point, the line tension $\lambda \rightarrow 0$, which is defined by

$$\lambda \approx |Tc - T|^{\nu} \tag{3}$$

This critical behavior is well-described by the two-dimensional Ising-model, considering nearest neighbor interactions, with the critical exponents $\nu=1$ and $\beta=1/8$ and $\lambda\xi=k_B T_c$.

1.3 Antimicrobial Peptides

Antimicrobial peptides (AMPs) are part of the immune defense system and they are found in every organism [44-46]. In higher organisms, AMPs are produced on epithelial surfaces or directly in endothelial and phagocytic cells [47], leading to an effective protection against infection. Beyond their antibacterial, antifungal and antiviral activities [48; 49] they are also involved in immunomodulatory activities and inflammatory processes [50-52]. There exists a certain degree of coupling between the innate and adaptive immune systems: antimicrobial

peptides influence both, the quality and effectiveness of immune and inflammatory responses [53]. AMPs kill bacteria within 15 to 90 minutes [54; 55] and their target is the membrane. Besides that, antimicrobial peptides can also be involved in biochemical processes like the inactivation of nucleic acids and cytoplasmic proteins [54].

1.3.1 Anti-Cancer Effects of AMPs

Many AMPs are active against cancer cells [22; 23; 47; 56; 57]. For example melittin (from the bee venom) inhibits tumor cell metastasis by reducing cell motility and migration [58]. The NK-2 (derivative from the porcine NK-lysin) killing activity correlates with the membrane exposure of negatively charged PS on the surface of cancer cells [23]. Magainin II (from frog skin) inhibited cell proliferation of bladder cancer cells in a dose-dependent manner [59], Gomesin (from the spider *Acanthoscurria gomesiana*) significantly delayed subcutaneous murine melanoma development and increased the number of living treated animals with tumors below the allowed maximal size limit [60].

It is still unclear why some AMPs kill cancer cells when others do not [61]. Beside the effect of opposite charges of the peptides and the membrane, differences in the fluidity and/or morphological changes of the membrane could be involved, as well as increased levels of sialic acid of glycolipids [22]. Probably, it is more an interplay between the peptide and membrane-based factors [56].

1.3.2 Antimicrobial Peptide Resistance

AMPs are thought to bring the way-out of the resistance problem of traditional antibiotics (‘the antibiotic crisis’ [62]). It was argued that a resistance against AMPs could only be attained by a change of the lipid composition (different charge, changed fluidity). That would mean a change in cell viability and can thus evolving resistance against AMP is excluded [55]. This is too simple and unfortunately not true. Alterations of net surface charges, structural alterations in LPS, changes in the membrane proteins, increased production of proteolytic enzymes or glycocalyx shielding can inactivate AMPs (for detailed discussion see the reviews [48; 49; 54]). A prospective resistance against AMPs in a broad medical use never can be excluded [63], but the structure-activity-relationship of natural AMPs should more serve as a template for the design of new peptides.

1.3.3 Amphipathic, Cationic, α-helical Antimicrobial Peptides

More than thousand AMPs are yet identified and published in databases [64; 65], but their mode of action is still not completely understood [54; 66; 67]. One class are the cationic, amphipathic, and alpha-helical peptides. These peptides are typically 12–37 residues in length, and may have a kink or a central hinge region [49]. But their sequence and their activity differs markedly [64; 68; 69]. Since bacteria cells are mainly composed of negatively charged lipids, electrostatic interactions must be involved in the cell-disrupting mechanism. But an interaction based only on electrostatics ignores additional molecular mechanisms, which can influence the peptide activity after binding to the membrane [70]. Due to the different composition of eukaryotic compared to vertebrate host cell membranes, most of the AMPs can distinguish between the target membranes [71], making them cell-selective. But also non-cell selectivity was observed for some AMPs, like melittin [72], LL-37 [73] and dermaseptin S4 [74].
Several modes of action are predicted for AMPs, including a 'carpet model', where the peptides interact primarily with the lipid head groups, or the formation of 'barrel-stave' or 'toroidal pores', where the peptides penetrate the lipid bilayer [52; 64; 69; 75] (see Figure 3). For the formation of pores, an aggregation of the peptide has to precede, making the formation of pores concentration dependent [76] or even target charge-dependent [75]. The disorganization of the membrane is accompanied by a change in the orientation of the peptide and a formation of pores, as seen for cardiotoxins [77] and other AMPs, like protegrin, alamethicin, melittin, and magainin [78-80]. While for the formation of a'torroidal pore' the peptides interact only with the head groups of the lipids, for the formation of a 'barrel-stave pore' the peptides permeate the bilayer.

For an interaction with the membrane via a 'carpet mechanism', the peptides cover the membrane and interact only with the lipid head groups. Therefore, the peptides are oriented parallel to the surface. The adoption of a secondary structure and a penetration of the peptides into the hydrophobic core of the bilayer is not mandatory. The membrane is disrupted in a detergent-like way. Polymyxin B is thought to act via that mechanism [81]. It is discussed that the formation of toroidal pores is part of the carpet mechanism (see Figure 3) [66]. Magainin [76; 79], almethicin [82], melittin [24; 79; 82] and some channel peptides [83] can be bound in two states and the formation of pores is transient [24; 84], meaning a mixed mechanism in the peptide activity. This makes the formation of pores not sufficient in their antimicrobial activity. The peptides can induce lesions by arranging parallel to the membrane, even without forming pores. But the exact mechanism is still unclear.

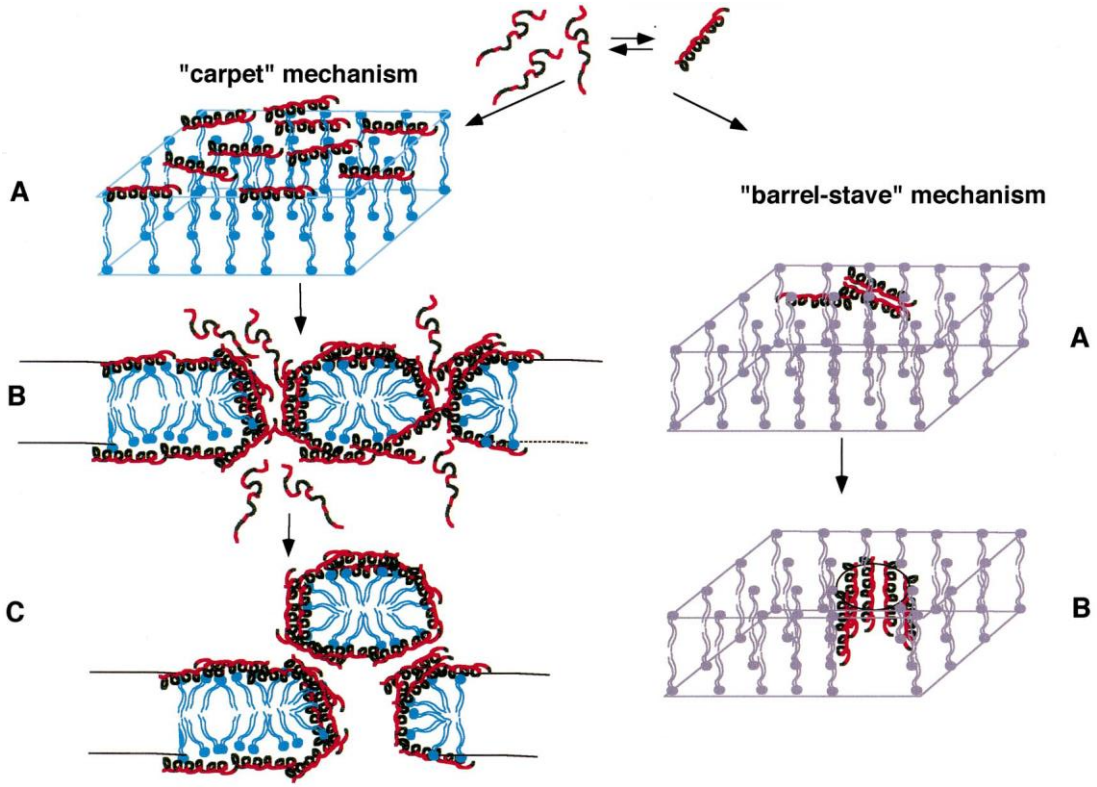

Figure 3: Membrane permeation of antimicrobial peptides, taken from [66]. For an interaction via a 'carpet' mechanism (left), the peptides bind parallel to the head groups of the lipids (A). After reaching a threshold concentration, the membrane is disrupted. A formation of transient torroidal pores is possible (B and C). Peptides acting via the 'barrel stave' mechanism (right) bind also parallel to the membrane (A), but change the orientation to build a pore which spans the bilayer (B). A certain concentration of neighboring peptides, which can build a pore, is necessary.

1.3.4 hCAP18/ LL-37

One class of amphipathic, cationic, α-helical AMPs is the class of the cathelicidins. They contain a highly conserved N-terminal domain called cathelin and a C-terminal domain that comprises an antimicrobial peptide [85]. In humans, only one AMP from this class is found, namely LL-37 [86; 87]. LL-37 is released from its precursor hCAP18 by proteases [88] and stored in the intracellular granules of neutrophilic granulocytes [89]. Initially identified solely as an antimicrobial protein, hCAP18/LL-37 is multifunctional with diverse and significant effects on eukaryotic cells [90]. It exhibits hemolytic activity [73; 91] and is cytotoxic against Gram-positive, Gram-negative bacteria [87; 91] and tumor cells [92]. LL-37 is also active against viruses [93]. It is not active against fungi, but can inhibit the growth [94] and the adhesion of *Candida albicans* to cell surfaces [95]. Some effects of LL-37 against biofilm formation were also reported (a review can be found in [96]). Furthermore, LL-37 can bind and neutralize lipopolysaccharides (LPS) from the cell membrane of Gram-negative bacteria [97; 98].

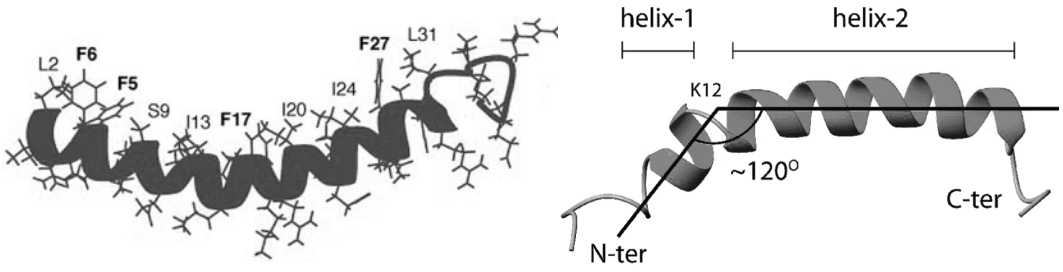

Figure 4: NMR resolved membrane stucture of LL-37 from different research groups [88; 99]

LL-37 is found on the skin, in sweat, and wound fluids (for review see [100]). LL-37 is found in the lung [101], where it induces wound healing, proliferation, and migration of airway epithelial cells [102]. Beside the antibiotic and wound healing features of the peptide, LL-37 is up-regulated in inflammations [52; 103], but also in some cancer types, like human prostate [104], breast [90; 105], ovarian [106] and lung cancer cells [107]. This is not surprising, since a correlation between inflammations and cancer is more widely accepted [108; 109]. On the other hand, LL-37 suppresses tumorigenesis in gastric cancer [110] and oral squamous cell carcinoma [92].

LL-37 binds as oligomers to zwitterionic membranes [111], but dissociates into monomers when in contact with negatively charged membranes [73]. An orientation of the helix parallel to the membrane [73; 111; 112] and a disruption of the membrane in a detergent-like carpet mechanism was proposed for LL-37 [73], but even formation of transmembrane pores has been reported [113; 114]. A mixed mechanism in the membrane disruption of LL-37 is likely [66; 115].

LL-37 adopts mainly an alpha-helical conformation, when in contact with a membrane mimetic environment [73; 88; 99; 116] (Figure 4). As resolved by NMR, a bend between Gly14 and Glu15 was proposed [88], but also a kink at Lys12, which breaks the helix into two helices with an angle of 120° [99]. An antimicrobial core was identified between the residues 18- 29, but is less active and only active against Gram-negative bacteria [88; 117]. The residues 1-12 are inactive against any cell type [110]. The residues 32-37 are unstructured [88], but involved in the proteolytic resistance and the haemolytic activity [73]. The fragment $LL37_{7-27}$ exhibits a good activity against microbes, but not against erythrocytes [118].

On the one hand, it was considered for the peptide that the interaction with the membrane is not mandatory based on electrostatics [119; 120] and that the helical content correlates with the antibacterial activity [121]. On the other hand the non-cell selectivity of the peptide implies the involvement of hydrophobic interactions [75] and no structure parameters can be defined that explain the strong interaction of LL-32 compared to other fragments [85].

1.4 Motivation of this Work

A detailed description of the characteristics of antimicrobial peptides (AMPs) is highly demanded, because AMPs are thought to provide a way-out of the 'the antibiotic crisis' [62], since the resistance against traditional antibiotics is an emerging problem in medicine. The lack of an efficient therapy for some cancer types (like malignant melanoma) and the evolvement of resistance against existing antitumor agents [22] make AMPs promising in cancer therapy, beside as an alternative to traditional antibiotics [122; 123]. Nowadays, nanocarriers filled with AMPs are investigated for cancer therapy [124; 125] and medical relevant materials can be coated with AMPs to suppress biofilm formation [126; 127]. But it is still not clear, which parameters influence the antibacterial and anti-cancer activities of many AMPs and how the peptides disturb the cell membrane integrity.

LL-37, a peptide from the human cathelicin family, and its antibacterial properties were discovered in the middle of the 1990s [97] and investigated frequently. Since cathelicidin-derived peptides can bind LPS, these peptides are of special interest [128]. LPS can be released upon infection and lead to the gram-negative sepsis with a shock in the host organism. The over-reaction of the immune defense system leads to death even after medical treatment in more than 20 % of the cases [129]. In the last 5 years, the peptide became a coveted research object when its involvement in cancer was discovered [90; 92; 104-107; 110].

The aim of this work was to find decisive differences between the membrane interactions of two peptide fragments of LL-37, which exhibit contrary behavior in biological experiments. It was shown that not only the antibacterial activity, but also the mode of action for fragments of LL-37 can be different [130]. The interaction of two fragments of LL-37 with model membranes was systematically studied in this work. Planar lipid films provide a useful model to study thermodynamical variables in two dimensions. Moreover, experiments on planar films are very suitable in the combination with surface sensitive methods to study peptide-lipid interactions (reviews can be found in [27; 30; 131; 132]). Planar lipid films have been mainly applied in this work, in combination with IR-spectroscopy and X-ray scattering methods.

In the first approach, the structure of the peptides in solution was compared to the structure of the peptides at the air/water interface. This interface is the simplest model for investigating the hydrophilic-hydrophobic interactions of peptides at the membrane and was already successfully employed for many other peptides [31; 32; 133]. Because of the presence of LL-37 in the lung, on the skin, in sweat, and wound fluids (for review see [100]), the air/water interface receives even a biological relevance. When the peptide is adsorbed to the air/water interface, surface sensitive Infrared Reflection Absorption Spectroscopy (IRRAS) measurements can reveal the secondary structure of the peptide at the water surface [134]. Additionally, X-ray Reflectivity (XR)

experiments can be performed to obtain more details of the peptide film [135] as the electron density profile perpendicular to the interface can be calculated.

In the second approach, experiments with lipid monolayers as biomimetic models for the cell membrane have been performed. The presence of the peptide at lipid monolayers can change the organization of the lipid film [136], which can be examined by controlling the surface pressure of the mixed film, performing IRRAS and Grazing Incidence X-ray Diffraction (GIXD) [34; 137]. In addition, Circular Dichroism (CD) experiments with vesicles have been performed, since the optical activity of peptides depends on the arrangement of the peptide bonds in different structures (α-helices, β-sheets etc.) [138]. CD spectroscopy complements the monolayer experiments.

In the third approach, the lipid monolayers were more adapted to human erythrocytes by incorporating sphingomyelin (SM) [139] to the PC monolayers. SM can lead to phase separation within the membrane [140-142] and is, together with cholesterol, involved in the formation of rafts [10], highly ordered microdomains which are involved in many biochemical processes [7; 11; 12]. Physical-chemical properties of the lipid films have been characterized and the influence of the peptides on them has been worked out. Additionally, the modelling of the peptide interaction with cancer cells was performed by incorporating some negatively charged lipids [23] to the PC/SM monolayers.

1.4.1 Fragments of LL-37 Used in this Work

In our study, two fragments of LL-37, named LL-20 and LL-32 have been used. Their helical wheel projection is shown in Figure 5. Both fragments lack the unstructured C-terminal part of the peptide and correspond to the residues 1-20 and 1-32, respectively. The peptides showed contrary behavior in biological experiments: the antibacterial and anticancer activity of LL-32 is increased compared to LL-37 [85; 87; 143]. On the contrary, LL20 exhibits reduced antibacterial [143; 144], anticancer and cytotoxic activity [143; 145] compared to LL-37. A reason for this might be the lack of the assumed antimicrobially active core LL-$37_{18\text{-}29}$ [88; 117].

LL-32 carries a positive net charge of 6+, like LL-37, while LL-20 carries a positive net charge of 4+. The formation of an α-helix leads to the amphipathic structure of the peptide. The *relative hydrophobic moment*[1] mH_{rel} can be calculated with the help of MPex [147; 148], applying the Eisenberg-scale [146], to $mH_{\text{rel,LL-20}}$ =0.47 and $mH_{\text{rel,LL-32}}$ =0.51, showing only slight differences for the two fragments.

[1] Relative to a perfect amphipathic α-helix with mH=0.8

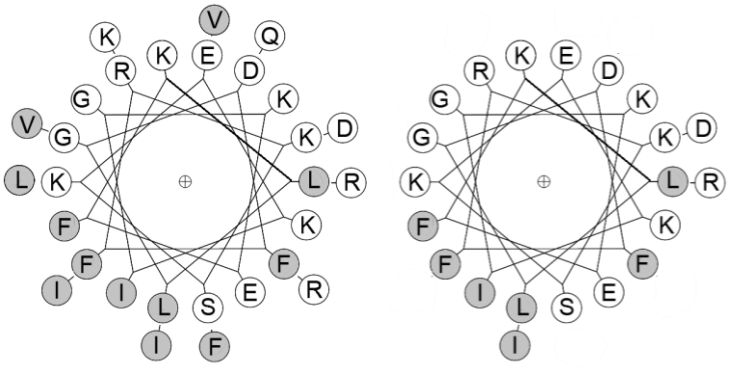

Figure 5: Helical wheel projection of LL-32 (left) and LL-20 (right). To emphasize the amphipathic structure of the peptides, hydrophobic amino acids are colored in grey (Eisenberg scale [146]).

2 Methods and Materials

2.1 Circular Dichroism Spectroscopy

The circular dichroism (CD) of a peptide is based on electronic transitions in the peptide bond. The difference in the absorbance between the left (L)- and right (R)- circularly polarized light is measured as a function of the exciting wavelength. It depends on the conformation of each bond (torsion angles) and is thus related to the secondary structure of the peptide.

CD spectra of the studied solutions were recorded on a Jasco J-715 (Japan) spectrometer in the wavelength interval from 190 to 260 nm with 0.2 nm step resolution using quartz cuvettes with an optical path length of 0.1 cm. The signal-to-noise ratio was improved by accumulating at least 4 scans. The peptide concentration was 63 µM in all experiments. Data processing was carried out using the J-700 software package. The spectra of the pure subphase were subtracted and the measured CD signal θ was transformed to mean residue molar ellipticity $[\theta]$

$$[\theta] = 100\frac{\theta}{Cl} \tag{4}$$

C is the molecular mass/concentration divided by the number of peptide bonds; l is the path length in the cuvette in cm.

2.1.1 Estimation of the Secondary Structure

Even though every conformation shows special absorption bands, the estimation of the content of helices, sheets and turns is quite sophisticated. Some algorithms are provided by the DICHROWEB [149; 150], like CONTINLL or SELCON. They are based on the known structure of proteins, resolved by NMR. The comparison with the measured spectrum gives the composition of the secondary structure of the sample. This comparison does not consider that also aromatic side chains can contribute to the spectrum. Also, the spectrum of a peptide bound in a vesicle can be different from the solution structure, even if the secondary structure is unchanged, as it was observed for helical peptides building transmembrane pores [34; 151]. An oligomerization can also lead to a change in the spectra [152]. Nevertheless, a shading of bigger particles (like vesicles or aggregated peptides) can lead to a signal decrease [153]. Therefore, CD spectroscopy was mainly applied to see the change in the secondary structure. The results obtained with the DICHROWEB are shown in the appendix but were not used for interpretation.

The experiments were done in water due to the strong absorption of Cl^- ions and the HEPES buffer [154], which were used in the other experiments.

2.2 Langmuir Film Balance

In this work, mixtures of peptides and lipids were investigated in planar films. Langmuir monolayers provide a useful model to study ordering in 2D [29]. The confined rotational and translational diffusion makes in some cases chemical reactions occur much faster at the 2D interface than in 3D bulk media [155]. The ratio of surface area per volume is high, so only few amounts of the sample are needed.

With a Langmuir film balance, the surface pressure is measured by using filter paper as a Wilhelmy plate, in order to ensure zero contact angle. Film balance measurements were coupled with InfraRed Reflection Absorption Spectroscopy (IRRAS), Grazing Incidence X-ray Diffraction (GIXD) or X-ray Reflectivity (XR) to obtain more detailed information about the structure of the film on a molecular scale.

Amphiphilic molecules adsorb to the air/water interface, and form a film which reduces the surface tension σ. The change in σ is defined as

$$\pi = \sigma_{water} - \sigma_{film} \tag{5}$$

with π being the surface pressure. π can be monitored time-dependent and isothermal in a Langmuir trough. The formed film of amphiphiles can be stable with a constant concentration of adsorbed molecules (Langmuir layer) or in equilibrium with adsorbed and desorbed molecules from the interface (Gibbs layer). Amphiphiles used in this work, are lipids and peptides. Lipids are spread on the surface from a chloroform solution to form Langmuir monolayers. After the solvent is evaporated, the film can be compressed and depending on the geometry of the molecules exhibit phase transitions. The characteristic isotherm gives information about the phase state and the packing behavior at the air/water interface. Amphiphilic peptides can be dissolved in the subphase and adsorb to the air/water interface. Peptides can also be spread on the surface, but there they form a metastable state [30]. In the thermodynamical equilibrium with the bulk phase, π_{eq} denotes the equilibrium surface pressure.

In lipid monolayer experiments, the observed phases range from a gaseous (G) to a liquid-expanded (LE)/ fluid, liquid-condensed (LC)[2] and solid (S) phase (see Figure 6). The main phases can be attributed to bilayer phases: the expanded phase is analogous to a fluid phase and the condensed phase is analogous to the gel phase. Phase transitions are indicated by the discontinuous behavior of the first derivative of the isotherm.

[2] The term "liquid-condensed" is mainly eliminated from the literature. As proposed by Kaganer *et al.*, in the further text the liquid-condensed phase is denoted as "condensed phase" (V.M. Kaganer, H. Mohwald, P. Dutta. Structure and Phase Transitions in Langmuir Monolayers. Reviews of Modern Physics,71 (1999), 779-819)

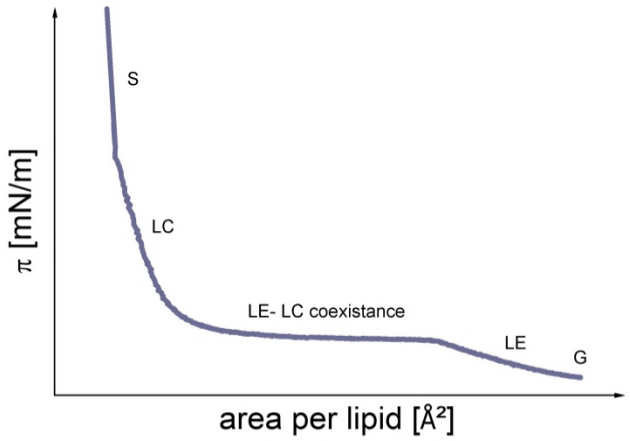

Figure 6: Isotherm of a lipid monolayer exhibiting phase transitions from the gaseous (G) to the liquid-expanded (LE), liquid-condensed (LC) and the solid (S) phase

The transition enthalpy $\Delta Q = T\,\Delta S$ between two phases of a first-order transition (like from the expanded to the condensed phase) can be described with a 2D Clausius-Clapeyron-equation:

$$\Delta S = \frac{d\pi_{PT}}{dT}\Delta A, \tag{6}$$

with π_{PT} being the critical surface pressure for the phase transition.

2.3 InfraRed Reflection Absorption Spectroscopy (IRRAS)

At the air/water interface, Infrared Reflection Absorption Spectroscopy (IRRAS) measurements can be applied to study the conformation of adsorbed molecules. Details of the technique can be found in the works of Flach and Mendelsohn *et al.* [134; 137]. The principle setup is shown in Figure 7. The IR beam is directed on the water surface at a certain angle of incidence, between 30° and 70°. The reflected beam is detected from the water surface at the same angles. The intensity of the evanescent wave travels along the surface and decays exponentially with the penetration depth, making this method very surface sensitive. The absorption by functional groups leads to distinctive bands in the IR-spectrum. Some typical vibrational modes for peptides and lipids are listed in Table 1.

Due to the strong and broad absorption of water, a trough shuttle technique was employed. A spectrum of the bare subphase R_0 was measured right before every sample spectrum R. The reflection absorption spectra RA was subsequently calculated with

$$RA = -\lg\frac{R}{R_0}. \tag{7}$$

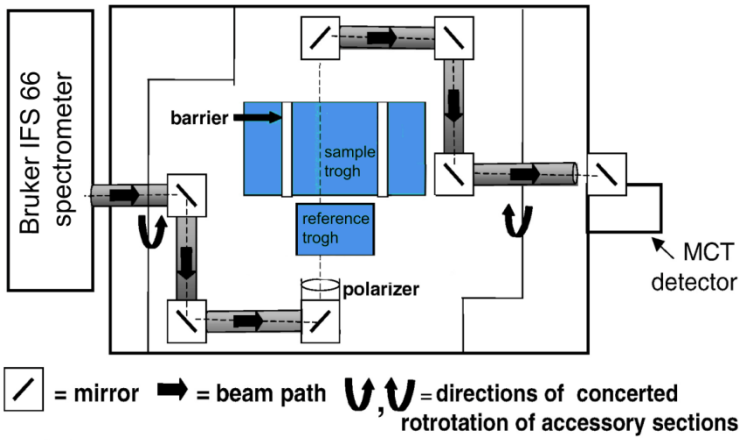

Figure 7: IRRAS setup, adapted from Mendelsohn et al [137].

With IRRA spectroscopy, the secondary structure of the peptide at the water surface can be obtained as an overall sum. The positions of the amide bands in the spectra depend on the secondary structure elements in the sample. The amide I band contributes mainly the C=O stretching vibration, which is very sensitive to hydrogen bonding of the peptide backbone and is mainly used for the estimation of the secondary structure of a peptide. The amide II band (in-plane bending and C-N stretching) is also sensitive to the hydrogen bonding, but it is less specific since other vibrations also contribute to the band. But the amide II vibration can be considered to validate the structure which was found by means of the amide I band.

The CH_2 band from the fatty acid tails of the lipids is sensitive to the conformation of the lipid chains. A transition from a gauche to an all-trans conformation can be seen by a shift in this band from 2924 cm^{-1} to 2919 cm^{-1} (asymmetric CH_2 vibration) and from 2854 cm^{-1} to 2849 cm^{-1} (symmetric CH_2 vibration). Using parallel (p) and perpendicular (s) polarized light, the orientation of the transition dipole moment can be derived. This is useful to determine the orientation of the molecules. The ratio of R_p/R_s is the dichroic ratio and is related to the tilt angle of the molecules. It can be employed to both, the amide I band of peptides and the CH_2 bands of lipids. The directions of the transition dipole moments of some vibrations in an α-helix, a β-sheet and a phospholipid are drawn in Figure 8. In a lipid, the transition dipole moment of the CH_2 vibration is normal to the lipid chain. In a perfectly oriented lipid monolayer, the chains are oriented parallel to the surface normal, and therefore the transition dipole moment is parallel to the air/water interface. For a peptide, the orientation of the transition dipole moment depends on the conformation of the peptide. In a β-sheet, the transition dipole moment lies in the plane of the β-sheet while in an α-helix, the transition dipole moment of the amide I is pointed 36°…39° away from the molecular axis [156; 158]. A deviation from the orientation leads to a changed absorption in the IR spectrum.

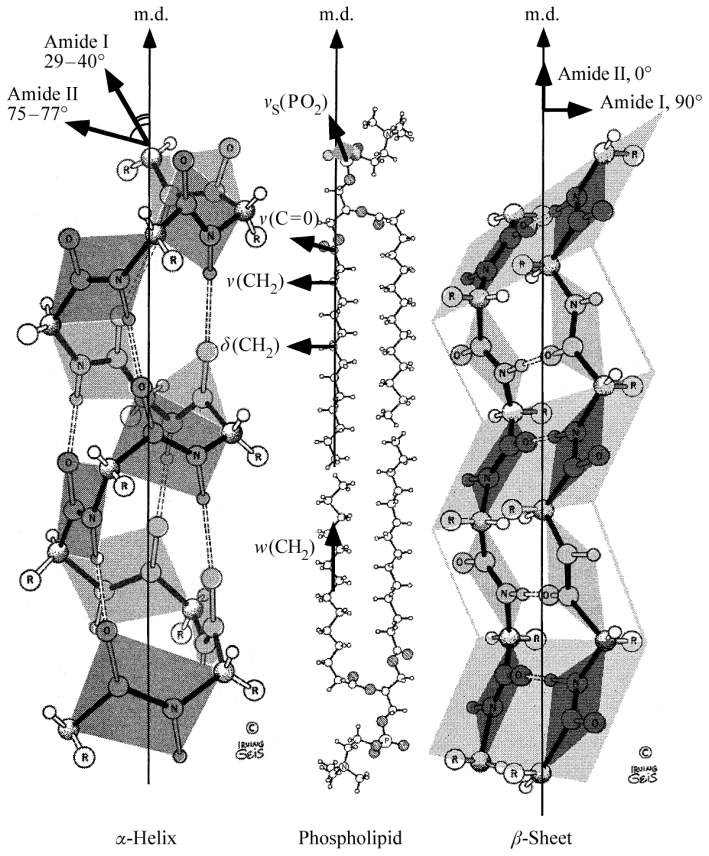

Figure 8: Direction of the transition dipole moments of characteristic vibrations in an α-helix, a phospholipid and a β-sheet, taken from [156]. M.d. denotes the molecular direction.

IRRA spectra were recorded with the IFS 66/ Vertex 70 FT-IR spectrometer (Bruker, Germany) coupled with a Langmuir film balance (Riegler & Kirstein, Germany) with a total area of 182 cm^2 and two movable barriers.

The films were compressed with a velocity of 4 $Å^2$ $molecule^{-1}$ min^{-1}. Angles of incidence were varied between 30° and 70°, the polarization of the beam was modulated to perpendicular (s) and parallel (p) polarized light. The reflected IR beam was detected at the same angles with a liquid nitrogen cooled MCT (Mercury Cadmium Telluride) detector. The resolution of the spectra is 8 cm^{-1}. The spectra were atmospheric compensated in OPUS 6.0 and shifted to zero at 1900 cm^{-1} and 2600 cm^{-1}, respectively.

Table 1: Some characteristic IR absorption bands of lipids and peptides, adapted from [32; 156; 157].

	Assignment	Wavenumber [cm^{-1}]	Specification	
Lipid chains	O-H (v_{as})	~3490		
	O-H (v_s)	~3280		
	CH_3 (v_{as})	2956		
	CH_2 (v_{as})	2920	Condensed phase: fluid phase:	2920 2924
	CH_3 (v_s)	2870		
	CH_2 (v_s)	2850	Condensed phase: fluid phase:	2849 2854
	C=O (v)	1730		
	H_2O (δ)	1645		
	COO^- (v_{as})	1623		
	CH_2 triclinic (c)	1473		
	CH_2 hexagonal (c)	1468		
	CH_2 orthorhombic (c)	1472/1463		
	CH_3 (δ_{as})	1460		
Peptides	amide A	~3300		
	amide I C=O (v) (76%), CN (v) (14%), CCN (d) (10%)	1600-1700	α-helix: random coil: turns: β-sheet: aggregated strands: antiparallel β-sheet:	1657-1648 1657-1642 1682-1662 1641-1623 1610-1628 1695-1674
	amide II NH (δ) (55%), CN (v) (29%), C=O (δ) (11%), […]	1510-1580	α-helix: β-sheet:	1545-1551 1552-1525

v stretching, *δ* bending, *c* scissoring, *d* deformation, s symmetric, as asymmetric

2.4 Surface Sensitive X-ray Scattering

A synchrotron beam can be diffracted from a liquid surface at low angles of incidence. For the horizontal scattering vector $\boldsymbol{Q}_{xy}>0$, Grazing-Incidence X-ray Diffraction (GIXD) can be measured while for $\boldsymbol{Q}_{xy}=0$ specular X-ray Reflectivity (XR) is measured. Combining both methods, different parts of the structure can be measured. While GIXD shows the periodically ordered packing of the lipids on the surface in xy-direction (in-plane), XR measures the electron density in z-direction (out-of-plane), meaning the thickness of the layer. A more detailed description of the theory and the experimental setup of the x-ray scattering methods can be found in the work of Jensen, Kjaer, Als-Nielsen *et al.* [29; 135; 159; 160].

GIXD and XR experiments were performed at BW1, HASYLAB, DESY (Hamburg, Germany). A Langmuir film balance (Riegler & Kirstein, Germany) with a movable barrier was placed in a hermetically sealed container with a Kapton foil window. The container was flushed with helium for at least 40 min to reduce the oxygen content. The trough was laterally moved during the experiments to eliminate sample damage due to the X-ray radiation. The stroke area had a size of 2 mm x 50 mm. An additional glass plate was used under the footprint area to reduce mechanically excited long-wavelength waves on the water surface [159]. The synchrotron beam was monochromated by a beryllium (002) crystal to λ=1.304 Å. A peptide concentration of 0.3 µM in the subphase was used for the experiments, because the trough had a different geometry with an increased ratio of surface area per volume. This had influence on the adsorption times of the peptides.

2.4.1 Grazing-Incidence X-ray Diffraction (GIXD)

The scattering vector $\boldsymbol{Q}$ is defined as $\boldsymbol{Q}=\boldsymbol{k}_f-\boldsymbol{k}_i$, with $\boldsymbol{k}_i$ being the incident, and $\boldsymbol{k}_f$ being the scattered wave vector. They represent the reciprocal space with $|\boldsymbol{k}_{i,f}|=k=2\pi/\lambda$ (see Figure 9). Bragg diffraction fulfills the Laue conditions in 2D only at $\boldsymbol{Q}=\boldsymbol{Q}_{hk}$ (h, k Miller indices), meaning that

$$\boldsymbol{Q}\boldsymbol{a} = 2\pi h, \boldsymbol{Q}\boldsymbol{b} = 2\pi k, \tag{8}$$

with the lattice parameters *a, b* which span the primitive unit cell. The scattering vector $\boldsymbol{Q}$ can be split into a horizontal and a vertical component $\boldsymbol{Q}_{xy}$ and $\boldsymbol{Q}_z$. After background subtraction, the Bragg rods Q_z were calculated with

$$Q_z = \frac{2\pi}{\lambda}[\sin(\alpha_i) + \sin(\alpha_f)] \approx \frac{2\pi}{\lambda}\sin(\alpha_f), \tag{9}$$

and the Bragg peaks $\boldsymbol{Q}_{xy}$ were calculated with

$$Q_{xy} = \frac{2\pi}{\lambda}[cos^2(\alpha_i) + cos^2(\alpha_f) - 2\cos(\alpha_i)\cos(\alpha_f)\cos(2\theta_{xy})]^{1/2} \approx \frac{4\pi}{\lambda}\sin\left(\frac{2\theta_{xy}}{2}\right). \tag{10}$$

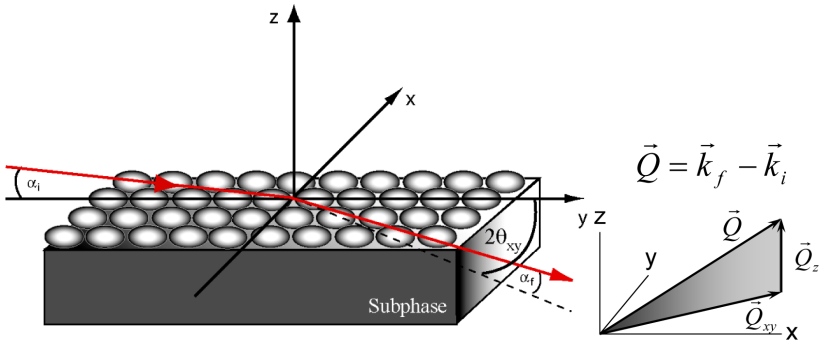

Figure 9: Schematic representation of a GIXD experiment, adapted from [161] and [162].

Due to the random orientation of the crystalline domains around the surface normal, the lipid monolayer can be seen as a 2D powder and $Q_{xy}=|\boldsymbol{Q_{xy}}|$ can only be measured as a combination of Q_x and Q_y.

Finally, Q_z and Q_{xy} were analyzed with a Gaussian and a Lorentzian fit, respectively. From that, the repeat spacing d can be calculated with

$$d = \frac{2\pi}{Q_{xy}} = [\frac{h^2}{a^2} + \frac{k^2}{b^2} - 2\left(\frac{hk}{ab}\right)\cos\gamma]^{-1/2}\sin\gamma. \quad (11)$$

γ is the angle between cell vectors **a** and **b**. The area of the unit cell A can be obtained from

$$A = a \cdot b \cdot \sin\gamma. \quad (12)$$

Due to the finite size of the crystalline domains, the Bragg peaks and rods are broadened. From the $FWHM_{intrinsic}$ ($Q_{xy,z}$) (full with at half maximum), the finite size of the domains L_{xy} can be calculated with

$$L_{xy} \approx 0.9[2\pi/FWHM_{intrinsic}(Q_{xy})]. \quad (13)$$

Therefore, the measured $FWHM_{meas}$ (Q_{xy}) has to be corrected to the instrumental resolution by

$$FWHM_{intrinsic}(Q_{xy}) = [FWHM_{meas}(Q_{xy})^2 - FWHM_{resol}(Q_{xy})^2]^{1/2}, \quad (14)$$

with $FWHM_{resol}(Q_{xy}) = 0.008$ Å^{-1}. The thickness of the diffracting layer L_z can be calculated with

$$L_z \approx 0.9[2\pi/FWHM(Q_z)]. \quad (15)$$

The monochromated synchrotron beam struck the surface at an angle of $\alpha_i = 0.85\alpha_c$, with $\alpha_c \approx 0.13°$ being the critical angle of total reflection. This makes it possible to measure surface sensitive, since the penetration depth is defined by the exponential decrease of the evanescent wave, and is only about 5 nm. The diffracted beam was collimated with a Soller collimator (JJ X-Ray, Denmark) and detected under varying vertical and horizontal scattering angles ($\alpha_f \geq 0$, $2\theta_{xy} \neq 0$; see Figure 9 for visualization of the angles) with a linear position-sensitive detector (OED-70-

M, Braun, Garching, Germany) or a MYTHEN detector system (PSI, Villingen, Switzerland). Bragg peaks and Bragg rods were analyzed with a Lorentzian and a Gaussian fit, respectively.

2.4.2 X-ray Reflectivity (XR)

XR measurements can help to clarify and identify the position of the peptide in the lipid monolayer, since from the reflectivity profile the electron density profile at the surface can be calculated [135]. This can help to distinguish between a penetration or an adsorption of the peptides.

In XR, the vertical scattering vector Q_z is measured for $\alpha_i = \alpha_f$ and $2\theta_{xy} = 0$ as a function of

$$Q_z = 4\pi/\lambda \sin(\alpha_f) \quad (16)$$

beween 0.01 $Å^{-1}$ and 0.85 $Å^{-1}$ (α_r is the angle of the reflected beam). The obtained reflectivity R was normalized to the FRESNEL reflectivity R_F, meaning a smooth surface or sharp interface. The data were analyzed by inversion into an electron density profile ρ normalized to water ρ_{water} by a model-independent method [163] using a linear combination of b-splines. The electron density was fitted with boxes of a defined thickness, electron density and roughness.

2.5 Chemicals and Sample Preparation

Peptides: The two fragments of LL-37, namely LL-20 and LL-32, were synthesized with C-terminal amidation by the solid-phase peptide synthesis technique on an automatic peptide synthesizer (model 433 A; Applied Biosystems) on Rink amide resin according to the fastmoc synthesis protocol of the manufacturer, including the removal of the N-terminal Fmoc-group. The peptide was cleaved from the resin and deprotected and with 90 % trifluoroacetic acid (TFA), 5 % anisole, 2 % thioanisole, 3 % dithiothreitol for 3 h at room temperature. After cleavage the suspension was filtered and the soluble peptides were precipitated with ice-cold diethylether followed by centrifugation and extensive washing with ether. Peptides were purified by RP-HPLC using a Jupiter 4µ Proteo column (Phenomenex). Elution was done by using a gradient of 0-70% acetonitrile in 0.1 % (TFA) to purities above 95%. The Purity was determined by analytical reversed-phase HPLC (UV 214 nm) and matrix-assisted laser-desorption-time-of-flight mass spectrometry (MALDI-TOF MS, Bruker). The masses are 3922 Da for LL-32 and 2465 Da for LL-20. The aqueous solutions were prepared using ultrapure water (specific resistance of 18.2 MΩcm) produced by a Millipore reverse osmosis unit. The peptides were dissolved in water to a concentration of c = 1 mg/ml. These peptide stock solutions were stored in the refrigerator at 4°C and used within one week. The peptides were synthesized by Rainer Bartels and kindly provided by Prof. Dr. Thomas Gutsmann, Research Center Borstel, Germany.

Table 2: Amino acid sequences of LL-37, and its fragments used in this study.

Peptide	Sequence
LL-37 (not used)	LLGDFFRKSKEKIGKEFKRIVQRIKDFLRNLVPRTES
LL-32	LLGDFFRKSKEKIGKEFKRIVQRIKDFLRNLV
LL-20	LLGDFFRKSKEKIGKEFKRI

***Lipid monolayer**:* Zwitterionic 1,2-Dipalmitoyl-sn-glycero-3-phosphocholine (DPPC), 1,2-dioleoyl-sn-glycero-3-phosphocholine (DOPC), bovine brain sphingomyelin (SM) and anionoic 1,2-dipalmitoyl-sn-glycero-3-phospho-(1'-rac-glycerol) (DPPG), 1-palmitoyl-2-oleoyl-sn-glycero-3-phospho-(1'-rac-glycerol) (POPG), 1,2-dioleoyl-sn-glycero-3-phospho-L-serine (DOPS) were purchased from Avanti Polar Lipids (USA) and stored at -20°C. For experiments, the lipids were dissolved in chloroform to a concentration of 1 mM and kept at 4°C. Film balance measurements were performed on buffer with 5 mM HEPES (Roth, Germany), 100 mM NaCl (Merck, Germany, heated to 600°) at pH 7.4.

***Lipid vesicles*:** 1-palmitoyl-2-oleoyl-sn-glycero-3-phospho-(1'-rac-glycerol) (POPG) and 1-palmitoyl-2-oleoyl-sn-glycero-3-phosphocholine (POPC) (Avanti Polar Lipids, USA) were dissolved in water to a concentration of 1 mM, vortexed for 5 min and sonicated in a water bath (T=30°C) for 15 min. To obtain unilamellar vesicles, the suspension was freeze-thawed 10 times. To obtain vesicles with a defined size, the suspension was pressed trough a polycarbonate filter (Avestin Inc., Canada) with a LiposoFastExtruder (Avanti Polar Lipids, USA). The size distribution of the vesicles was measured with Dynamic Light scattering. The averaged diameter was calculated for POPC to $d_1 = 78$ nm and for POPG to $d_2 = 117$ nm.

3 Surface Activity and Structures of the Two Peptides

Abstract

Two fragments of the antimicrobial peptide LL-37 (LL-32 and LL-20) have been characterized in adsorption layers at the air/water interface by Infrared Reflection Absorption Spectroscopy (IRRAS) and X-ray Reflectivity (XR) measurements. As shown in previous work, LL-32 exhibits an increased antimicrobial activity compared to LL-37 while LL-20 is almost not active. In water, both peptides are in an unstructured conformation. Adsorbed at the air-water interface, the peptides differ drastically in their surface activity (equilibrium adsorption pressure) as well as in their secondary structure. While LL-32 transforms into an α-helix lying flat at the water surface, with a helix diameter of 14 Å, LL-20 stays partly unstructured. The dichroic ratio is reduced and the electron density profile shows the formation of a second layer, whereas the electron density profile of LL-32 agrees with that of an entire α-helix. The ability to form a complete α-helical structure at the interface is in good agreement with the high antimicrobial activity of LL-32.

3.1 Peptides in Water

To determine the secondary structure of the peptides in solution, CD experiments were performed (Figure 10). Due to the strong absorption of HEPES and NaCl, the CD experiments were done in pure water. Both peptides exhibit a broad minimum at 198 nm and a tiny minimum at 230 nm. The spectra are typical for an unstructured conformation [154] and comparable to LL-37 [121]. Using the AGADIR algorithm [164], a theoretical helix content of LL-32 was calculated to 0.9% and that of LL-20 to 0.3% in water at pH 6, showing that both peptides have a marginal propensity to form an α-helix. The theoretical helix content increases only slightly (1.8% for LL-32 and 0.6% for LL-20) with increasing ionic strength (100 mM NaCl at pH 7.4). The results obtained with DICHROWEB [150; 165] deviate and are shown in the appendix. The data bases are derived from larger proteins and therefore are hardly applicable for short peptides.

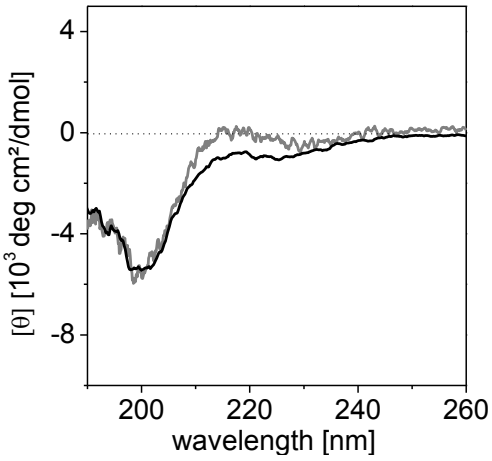

Figure 10: CD spectra of LL-32 (—) and LL-20 (—) in water at 20 °C. 63 µM peptide in solution.

3.2 Peptides at the Air/water Interface

LL-32 and LL-20 adsorb to the air/water interface only in the presence of salt and lead to an increase in the surface pressure π (Figure 11). This is an effect which was already observed for other AMPs [31; 34] and can be explained by a reduced peptide charge due to the electrostatic interaction with counter ions leading to a reduced repulsion between the adsorbing peptide and the corresponding image charge, and will not be discussed in detail. Based on AGADIR we expect no influence of the increasing ionic strength on the secondary structure, but we observed huge changes in the surface activity. The equilibrium surface pressure π_{eq} was determined for different peptide concentrations in bulk (Figure 11A)). The minimal bulk concentration to achieve a completely covered surface was used in the following experiments (0.2 µM). The equilibrium surface pressure π_{eq} is 24 mN/m for LL-32 and only 6 mN/m for LL-20 (Figure 11B)). Due to the

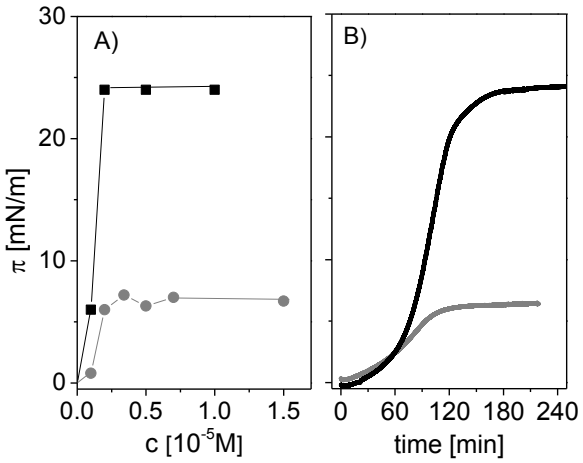

Figure 11: Film balance measurements: adsorption of the peptides to the air/water interface.
A) The equilibrium surface pressure π_{eq} for LL32 (■) and LL-20 (●) depends on the peptide concentration c in the subphase. The minimal concentration to achieve maximum π_{eq} was used in the following experiments. B) Time-dependent surface pressure π of LL-32 (—) and LL-20 (—).
(5 mM HEPES, 100 mM NaCl, pH 7.4, 20°C)

slow desorption kinetics, the peptide films can be compressed to surface pressures well above π_{eq}: 34 mN/m for LL-32 and 12 mN/m for LL-20.

3.2.1 Infrared Reflection Absorption Spectroscopy (IRRAS)

After reaching the adsorption equilibrium, IRRA spectra were recorded using different incidence angles (Figure 12 A)). The amide I band around 1660 cm^{-1} can be fitted with two Lorentzian curves with maxima at 1658 cm^{-1} and 1679 cm^{-1} for LL-32 and 1658 cm^{-1} and 1668 cm^{-1} for LL-20. The vibration at 1658 cm^{-1} is related to an α-helical conformation but could also arise from unstructured conformations. However, the sign of the amide I band changes for incidence angles above the Brewster angle, thus a dominant helical conformation can be predicted. Also, the position of the amide II band at 1548 cm^{-1} is characteristic for an α-helix. The additional high frequency vibrations in the spectra can be indicators for non-hydrogen bonded C=O stretching vibrations from the peptide interior [157]. By comparing the areas of both bands, the latter contributes 30±5% to the spectra. Being unstructured in bulk the peptides are in an α-helical conformation at the interface.

The intensity of the amide I band depends on the peptide density, but also on the alignment of the peptide at the interface. Measurements at different angles of incidence using different polarizations of the incident light can help to shed light on the orientation of the helix at the interface. Therefore, measurements using p- and s-polarized light at different angles of incidence have been performed. For s-polarized light, the absolute values of the band intensity in the reflectance absorbance spectra increase monotonically with increasing angle of incidence. For p-

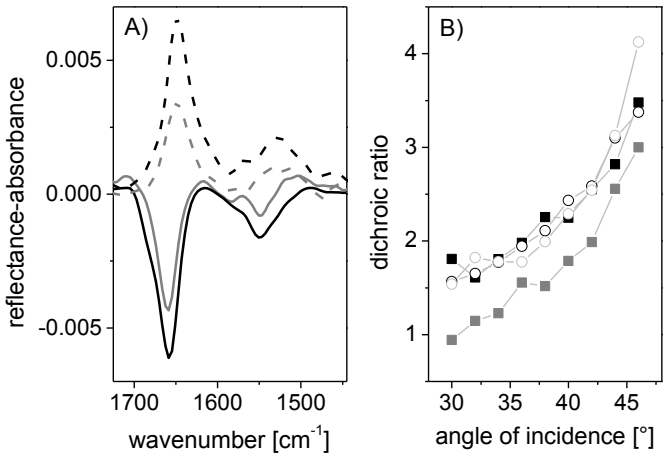

Figure 12: A) IRRA spectra of the amide I and II band of LL-32 (—) and LL-20 (—) adsorbed to the air/water interface. Shown are the spectra for p-polarized light at incidence angles of 40° (solid line) and 60° (dashed line) B) Dichroic ratio of the amide I band (1660 cm^{-1}) of LL-32 at π_{eq} = 24 mN/m (■) and π_l = 34 mN/m (○), LL-20 at π_{eq} = 6 mN/m (■) and π_l = 12 mN/m (○) for varied angles of incidence. (5 mM HEPES, 100 mM NaCl, pH 7.4, 20°C, 0.2 µM peptide in solution)

polarized light, the sign of the band changes at the Brewster angle and the resulting changes in band direction, intensity, and position allow the determination of orientations of secondary structure elements. To elucidate the LL-32 conformation and orientation at the interface, measured IRRA spectra can be compared with simulated spectra (see appendix). The spectra can be best described by an α-helix with its helical axis in the surface plane.

Calculating the intensity ratio of the amide I band using p-polarized and s-polarized light gives the dichroic ratio, which provides additional information about changes of the peptide in-plane and out-of-plane orientation [137]. For LL-32, the angle dependent dichroic ratio at the equilibrium surface pressure (24 mN/m) and after compression (34 mN/m) is the same (Figure 12 B)). This shows clearly that the compression of the adsorption layer does not lead to a peptide bend or tilt. Also, a change to a more parallel alignment of the helices, as in a 2D nematic phase [166], can be excluded. Upon compression of the peptide adsorption layer, the intensity of the OH stretching band at 3600 cm^{-1} increases. The intensity of this band depends on the effective adsorption layer thickness [167], because the intensity of the water OH stretch vibration in the spectrum of the sample trough is reduced in comparison with the reference trough, since the adsorption layer replaces a water layer of the same thickness. The intensity increase can only be explained by either an unlikely increase of the peptide layer thickness (bend or tilt has been excluded based on the dichroic ratio data) or an increased packing density in the peptide film but without going into a 2D nematic phase.

The dichroic ratio of LL-20 at the equilibrium pressure (6 mN/m) is smaller than that of LL-32, suggesting a less structured peptide film due to a certain fraction of unstructured molecules [137]. Compression of LL-20 (to 12 mN/m) leads to values of the dichroic ratio comparable to that of

LL-32, indicating the transition of unstructured peptides to helical conformation. This might be also the reason for the same intensity of the OH stretching band at 3600 cm^{-1} before and after compression showing that the effective thickness of the LL-20 peptide layer is not changed. The higher packing density induced by compression could be balanced by the transition of the peptide from an unstructured conformation to a helical conformation.

3.2.2 X-Ray Reflectivity

To obtain information of the peptide orientation normal to the air/buffer interface, X-ray reflectivity (XR) measurements were performed. From the experimental XR curves (Figure 13 A)), the corresponding profile correlation function is estimated via indirect Fourier transformation. For this profile correlation function, the matching electron density profile is then derived by square-root deconvolution. No a priori assumptions on the shape of the electron-density profile have to be made. The obtained relative electron density distributions along the surface normal to the peptide monolayers at the air/buffer interface normalized to water are shown in Figure 13. To obtain the absolute values of the electron densities, the relative electron density has to be multiplied with the electron density of water ρ_{water}= 0.334 $e^-/Å^3$.

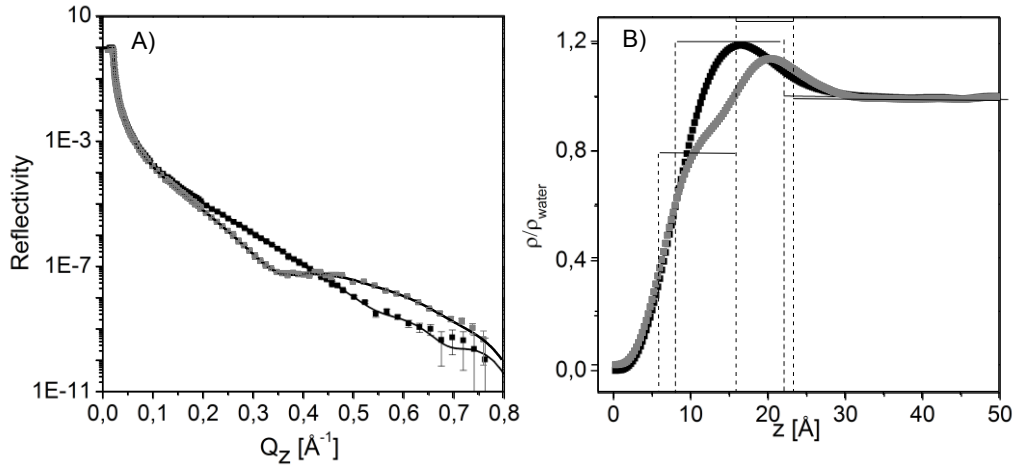

Figure 13: A) X-ray Reflectivity and B) calculated relative electron density profile of the peptides adsorbed the air/water interface: LL-32 (—) at π_{eq} = 24 mN/m and LL-20 (—) at π_{eq} = 6 mN/m (5 mM HEPES, 100 mM NaCl, pH 7.4, 20°C, 0.2 µM peptide in solution). Q_z is the out-of-plane scattering vector, z the distance from the interface, ρ/ρ_{WATER} is the electron density normalized to water.

The electron density profile of LL-32 (Figure 13 B), black curve) can be fitted with a one-box model. Based on the box thickness of (13.9±0.5) Å, an absolute electron density of (0.4±0.02) $e^-/Å^3$ and a roughness of (3.4±0.1) Å towards air and (3.7±0.1) Å towards water, it is concluded that the α-helix of LL-32 is lying flat at the interface. This is in agreement with the IRRAS data and with literature data showing that the thickness of an α- helix is between 13 Å [135] and 17 Å [31; 168]. The lack of Bragg peaks in the GIXD implies a random orientation of the helices and the

absence of a two-dimensional order in the peptide adsorption film. Compression of the LL-32 film leads to an estimated thickness of (15.4±0.5) Å with a roughness of (4.2±0.1) Å and (3.9±0.1) Å towards air and water, respectively. The electron density amounts to (0.40±0.02) $e^-/Å^3$. A change in the orientation of the peptide as a bend or the formation of a second layer would lead to an increase of the calculated thickness.

The electron density of the compressed LL-32 film agrees with measurements of another α-helical peptide, NK-2 [31], but it is slightly reduced in the uncompressed peptide film of LL-32. This is probably due to a less densely packed film. Upon compression, the peptide could arrange better with less space between the molecules, leading to the observed increase of the electron density.

The reflectivity data for LL-20 is clearly different. The calculated electron density profile (Figure 6 B), grey curve) is not symmetrical as observed for LL-32. Such a profile had to be fitted with 2 boxes. The first box has a thickness of (9.7±0.5) Å with an electron density of (0.27±0.02) $e^-/Å^3$, a roughness of (2.5±0.1) Å towards air and (3.6±0.1) Å to the next box. The second box has a thickness of (6.6±0.5) Å and a roughness of (4.0±0.1) Å towards the subphase. The electron density amounts to (0.43 ±0.02) $e^-/Å^3$. The sum of the thicknesses of the two sub-layers is with (16.3±0.5) Å comparable with the thickness of an α-helix. The electron density in both contributions is clearly smaller compared with that of well-packed stretched helices. The decreased electron density corresponds to a more diluted peptide layer. The dilution of the peptide is also supported by the much lower equilibrium values of the adsorption pressure. One possibility to explain the electron density profile could be that one part of the adsorbed peptide forms an α-helix and another part stays unstructured. Or some peptides molecules transform into the α-helix and other do not. These explanations might be surprising, because no difference in the secondary structure was observed with IRRAS. However, the dichroic ratio for LL-20 at equilibrium pressure differs drastically from that of LL-32. This could support the assumption that some adsorbed molecules of LL-20 stay unstructured. This would result in more or less the same position of the amide I band in the IRRA spectra, but in another dichroic ratio and would lead to another electron density profile in XR. In contrast to LL-32, the transition from the unstructured to the helical conformation is obviously incomplete in the LL-20 adsorption layer. This could be either due to slow transformation kinetics or due to the existence of a peptide concentration threshold at the surface. The latter seems to be the main reason, because the compression of the peptide film had only little effect on the electron density profile.

The compressed LL-20 film has to be again fitted with two boxes with thicknesses of (10.6±0.5) Å and (8.2±0.5) Å. The electron densities amount to (0.27±0.02) $e^-/Å^3$ and (0.41±0.02) $e^-/Å^3$. The roughness of the boxes is estimated to (4.33±0.1) Å towards water, (3.09±0.1) Å

between the boxes and (2.63±0.1) Å towards air. The LL-20 film cannot be compressed to such high packing densities as observed for LL-32 with an equilibrium value of 24 mN/m compared to the maximum value of only 12 mN/m which can be reached after compression of LL-20. These values show that the transition threshold for a perfect helix cannot be reached as indicated by the same electron density profile, even if the dichroic ratio is increased.

3.3 Discussion

Two fragments (LL-32 and LL-20) of the antimicrobial peptide LL-37 have been characterized in bulk and adsorbed at the air/buffer interface by CD and IRRA spectroscopy, respectively. XR was used to determine the electron density profiles perpendicular to the buffer surface. LL-32 and LL-20 are in water in an unstructured conformation. Theoretical calculations using AGADIR show that the increase of the ionic strength does not change the secondary structure in bulk, but increases drastically the surface activity of the peptides. The equilibrium adsorption pressures of both peptides are quite different (π_{eq} ~ 24 mN/m for LL-32 and ~ 6 mN/m for LL-20). The relative mean hydrophobic moment mH_{rel} of the helix (relative to a perfect amphipathic peptide) can be calculated with MPex [147], using the Eisenberg-scale [146], to mH_{rel} = 0.47 for LL-20 and mH_{rel} = 0.51 for LL-32. This shows only a marginal difference in the amphipathy, which is not large enough to explain the huge differences in the surface activity. The only explanation for the higher surface activity of LL-32 could be the larger molecular size, which stabilizes the α-helical conformation at the interface (for review see [30]).

CD spectroscopy showed bands characteristic for an unstructured peptide. IRRA spectroscopy showed, that the peptides transform into helices, when they are adsorbed to the air/ water interface in the presence of salt. Obviously, the adsorption of the peptides to a hydrophobic/hydrophilic interface is connected with a secondary structure change. This effect has already been observed for other antimicrobial peptides, like NK-2, arenicin, melittin or others [31; 32; 71; 169]. But this is not a general phenomenon for peptides, since also the solution structure of peptides and proteins can be preserved at the air-water interface [30].

LL-32 forms an entire helix with the molecular axis parallel to the interface and a diameter of 14Å, which is in accordance with other α-helical peptides [31; 166; 168]. LL-20 forms unstructured, amphipathic intermediates, which can be squeezed out from the interface by compression. This was resolved from the electron density profile, obtained from the XR curves. The smaller dichroic ratio for LL-20 at equilibrium pressure supports the assumption that some adsorbed molecules of LL-20 stay unstructured. In contrast to LL-32, the transition from the unstructured (in bulk) to the helical conformation at the surface is obviously incomplete in the LL-20 adsorption layer. This could be either due to slow transformation kinetics or due to the

existence of a peptide concentration threshold at the surface for such a transition. The latter seems to be the main reason, because the compression of the peptide film had only little effect on the electron density profile. The two parts of the adsorption layer are still seen with slightly increased thickness (21.7 Å at 12 mN/m), mainly because of the higher compressibility of an unstructured peptide layer. In conclusion, the LL-20 film cannot be compressed to such high packing densities as observed for LL-32. Therefore, the transition threshold for a complete α-helical conformation cannot be reached even if the dichroic ratio is increased. The helical peptides at the surface contribute stronger to the IRRA spectra than the unstructured ones. The measured dichroic ratio for the compressed peptide film is therefore similar to the one observed for the helical LL-32.

Neville *et al.* performed XR measurements on LL-37 [136]. At zero equilibrium adsorption pressure, the electron density was fitted with a box thickness of only 7.7 Å, but the same maximum electron density of ~0.4 $e^-/Å^3$ as in our case. Since the authors used only half of the concentration we used for our experiments, and the equilibrium adsorption pressure is zero, the surface is obviously not completely covered with the peptides. After compression to 28 mN/m, two boxes had to be used to fit the XR data with thicknesses of L_1 = 8.5 Å and L_2 = 4.3 Å and electron densities of 0.38 and 0.32 $e^-/Å^3$, correspondingly. This was interpreted by the formation of a second layer. As described in the introduction, LL-37 adopts mainly α-helical conformation and an unstructured part involving the residues 32-37. Therefore, this observation supports our assumption that the two contributions to the electron density profile of LL-20 originate from helical and unstructured peptides, even if the determined box thicknesses do not match our results.

4 The Influence of the Peptides on Lipid Monolayers

Abstract

LL-32 and LL-20 (two fragments of the human antimicrobial LL-37), which show a contrary behavior in biological experiments, have been characterized on their physico-chemical properties. To obtain insight into the peptide structure and their influence on phospholipids, lipid monolayers were used as a simple model for the outer leaflet of a cell membrane. Film balance measurements were coupled with surface sensitive Infrared Reflection-Absorption Spectroscopy (IRRAS), Grazing Incidence X-ray Diffraction (GIXD), and X-ray Reflectivity (XR). The results were compared to CD measurements with vesicles.

LL-32 is more surface active and can better intercalate into lipid monolayers than LL-20. Even though LL-32 has no cell-selectivity, our results show how the peptide interacts differently with zwitterionic compared to anionic membrane models. The interaction with dipalmitylphosphatidylcholine (DPPC) monolayers is based on the simple intercalation of the peptides between the lipid molecules, which leads to a phase transition of the lipids to a condensed phase. But the peptides bind in a two-step process to dipalmitylphosphatidylglycerol (DPPG) monolayers, which results in a fluidization of the lipid film. This can be related to a membrane thinning.

4.1 Interaction of the Peptides with Lipid Monolayers

In this chapter, the interaction of LL-32 and LL-20 with different model membranes was investigated. To model the interaction with mammalian cell membranes, lipid monolayers composed of the zwitterionic DPPC and DOPC, respectively, were formed. To investigate the interaction with bacterial cell membranes, lipid monolayers of the negatively charged DPPG and POPG, respectively were formed. DPPC and DPPG exhibit phase transitions from the expanded to the condensed state. This makes them a useful model membrane, since the influence of the peptide on the phase state of the lipids can be visualized. Many proteins and peptides interact preferentially with a fluid phase, so experiments with POPG and DOPC complement the obtained results.

4.1.1 Interaction with Pre-Compressed Monolayers: the Fluid Phase is Preferred

4.1.1.1 Maximum Insertion Pressure Measurements

Maximum Insertion Pressure (MIP) measurements with monolayers are a quite simple method to assess if a peptide would interact with a biological membrane. The peptide is injected under a pre-compressed monolayer with a defined surface pressure π_i. An interaction of the peptide with the lipids leads to a change in the surface pressure π. Plotting the change of the surface pressure $\Delta\pi=\pi-\pi_i$ depending on the initial pressure π_i, linear fitting and extrapolating to $\Delta\pi=0$ gives the MIP, up to which an interaction of the peptide with the lipid monolayer is energetically favorable [170]. If a peptide interacts with a cell membrane, the value of the MIP should be higher or in the range of the lateral pressure in a membrane. This was found to be 30…35 mN/m [37; 38]. Additionally, the slope of the linear fit gives further information on the peptide interaction: an equilibrium surface pressure π_{eq}=const. for all π_i, means that the MIP is a stationary surface pressure [171; 172] and independent from π_i. The slope in the linear fit of $\Delta\pi(\pi_i)$, $\frac{d(\Delta\pi(\pi_i))}{d\pi_i}\approx$-1. A non-stationary $\pi_{eq(\pi_i)}$ leads to a reduced increase in $\Delta\pi_{(\pi_i)}$ with increasing π_i, meaning that $\frac{d(\Delta\pi(\pi_i))}{d\pi_i}>$-1, and makes it more difficult for the peptide to interact with the monolayer with increasing π_i.If $\pi_{eq(\pi_i)}$ is increasing with increasing π_i, the MIP corresponds more to an Exclusion Pressure (EP) [171; 172].

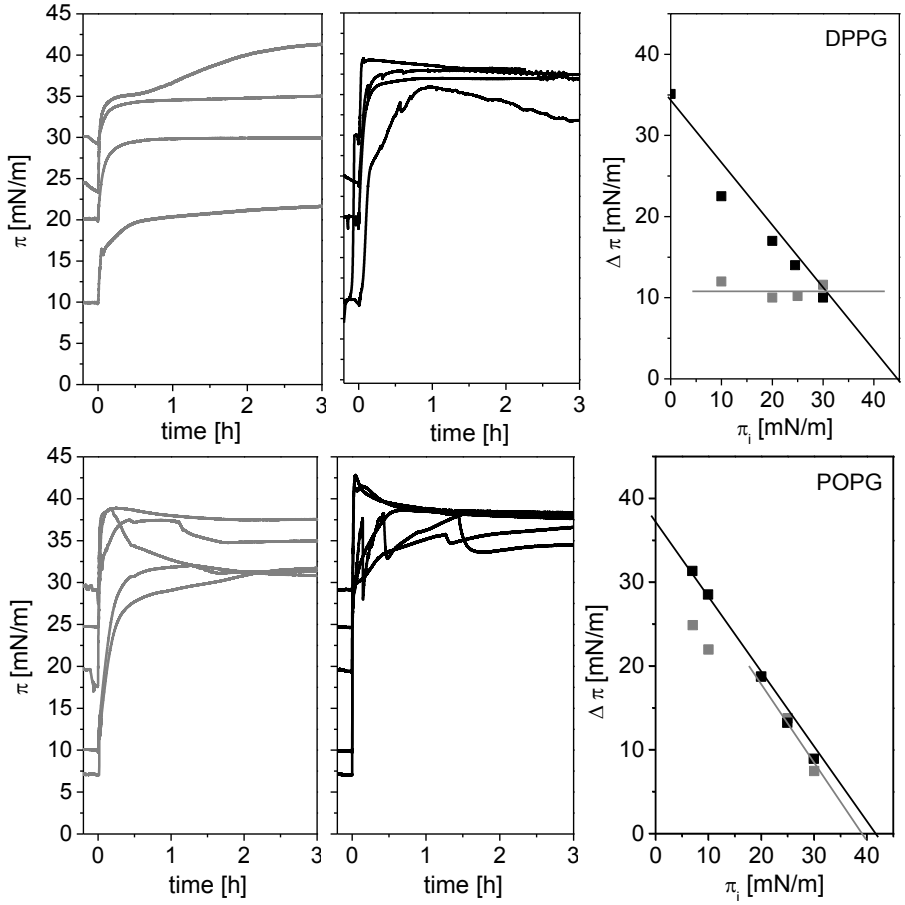

Figure 14: Estimation of the MIP of LL-20 (—, ■) and LL-32 (—, ■) into negatively charged DPPG and POPG monolayers. Shown is the time-depending surface pressure π for varied π_i. The increase in the surface pressure Δπ dependent on the initial pressure π_i is plotted on the right. Extrapolating the linear fit to Δπ = 0 gives the MIP. (5 mM HEPES, 100 mM NaCl, pH 7.4, 20°C, 0.2 µM peptide in solution).

The change in surface pressure after the injection of LL-32 and LL-20 (injection at t=0) and the extrapolation of the MIP are shown for DPPG, DPPC, POPG and DOPC monolayers in Figure 15. The results of the fit (MIP and slope) are listed in Table 3.

LL-32 has a high affinity for negatively charged lipid monolayers. The injection of LL32 under pre-compressed POPG and DPPG monolayers leads to a strong increase in the surface pressure. The equilibrium surface pressure are π_{eq}(DPPG) ≈ 37 mN/m and π_{eq}(POPG) ≈ 38 mN/m for all π_i. That means that $\pi_{eq(\pi_i)}$ is a stationary surface pressure and that the phase state has no influence on Δπ and the MIP [172]. The slope in the linear fit of $\Delta\pi(\pi_i))$, $\frac{d(\Delta\pi(\pi_i))}{d\pi_i} \approx -1$. The MIP of LL-32 is found to be (45±3) mN/m for DPPG and (40±2) mN/m for POPG.

The injection of LL-20 under DPPG leads to a constant increase in Δπ = 10 mN/m for all π_i, with $\frac{d(\Delta\pi(\pi_i))}{d\pi_i} = 0$. This leads to a MIP = ∞, but reflects only electrostatic attraction and not a hydrophobic interaction, because it is independent from the phase state of the phospholipids. The

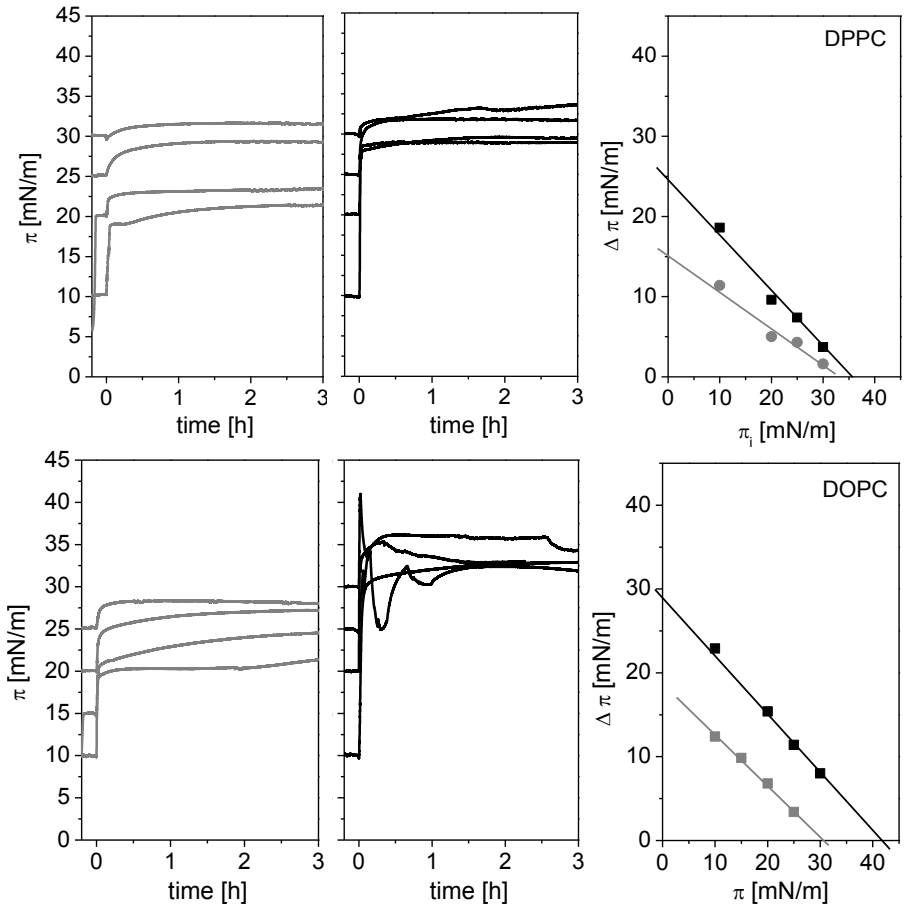

Figure 15: Estimation of the MIP of LL-20 (—, ■) and LL-32 (—, ■) into zwitterionic DPPC and DOPC monolayers. Shown is the time-depending surface pressure π for varied π_i. The increase in the surface pressure Δπ dependent on the initial pressure π_i is plotted on the right. Extrapolating the linear fit to Δπ = 0 gives MIP. (5 mM HEPES, 100 mM NaCl, pH 7.4, 20°C, 0.2 µM peptide in solution)

peptide is attracted to the charged head groups, compensating the negative charge, but exhibits no further interaction with the lipids. The peptide could be inactivated by hindering hydrophobic interactions, which play a strong role in the activity of helical antimicrobial peptides [64; 173-175].

The effect of LL-20 to POPG monolayers is comparable to the interaction of LL-32 with POPG. The MIP is 38 mN/m and corresponds to a stationary surface pressure.

The MIP of LL-20 is estimated to be (32±3) mN/m into DPPC monolayers. Together with a low slope $\frac{d(\Delta\pi(\pi_i))}{d\pi_i}$=-0.5 it is obvious that LL-20 has only a low affinity for DPPC, but also DOPC monolayers. LL-20 cannot bind to zwitterionic lipid monolayers at physiological relevant surface pressures (30 mN/m), independent of the lipid phase state. LL-32 has a MIP of (35±2) mN/m into DPPC with a slope $\frac{d(\Delta\pi(\pi_i))}{d\pi_i}$=- 0.7, meaning an interaction with the zwitterionic DPPC for low π_i.

The MIP of LL-32 into DOPC monolayers is even comparable with that of POPG and is in agree-

Table 3: Maximum Insertion Pressure (MIP), and slope of the linear fit.

		MIP [mN/m]	**Slope** $\frac{d(\Delta\pi(\pi_i))}{d\pi_i}$
LL-32	DPPG	45±5	-1
	DPPC	35±2	-0.7
	POPG	40±2	-1
	DOPC	42±2	-0.7
LL-20	DPPG	∞	0
	DPPC	32±3	-0.5
	POPG	38±3	-0.9
	DOPC	30±1	-0.7

ment with the non-cell selectivity of the peptide [73].

In the experiments with LL-32 and DOPC and POPG monolayers, irregularities in the adsorption isotherm are visible. A drop in the isotherm and a decrease in the surface pressure after the peptide injection is generally described as a condensing effect due to a compensation of charges [176-178]. From other injection experiments, by keeping the surface pressure constant while the change in the area is monitored, it was concluded that a drop in the surface pressure is the result of film lability [136; 179]. This we also propose here, since the isotherms show several instabilities which cannot be explained by condensing effects. The injection of LL-32 under monolayers composed of lipids in a fluid phase state leads to a strong accumulation of the peptides at this interface and to a high increase in the surface pressure. This leads to local destabilizations of the lipid monolayer which result in the drop of the surface pressure. Due to further adsorption of peptides, the surface pressure further increases, leading to additional defects until adsorption equilibrium of the peptide is reached.

4.1.1.2 Infrared-Reflection-Absorption Spectroscopy with LL-32

IRRAS measurements at the air/water interface can be performed additionally to the MIP experiments. They are useful to examine the interaction of the peptides with the lipids. An interaction with the head groups and/or the hydrophobic chains leads to differences in the packing which is reflected by the CH_2 band position. The amide bands are connected with the secondary structure of the peptide. The OH-band intensity is related to the film thickness[3] and is influenced by the tilt angle of the molecules and the formation of additional layers.

[3] With increasing film thickness, the number of water molecules at the surface is replaced by the presence of lipids and peptides at the water surface, which leads to this positive band in the spectrum.

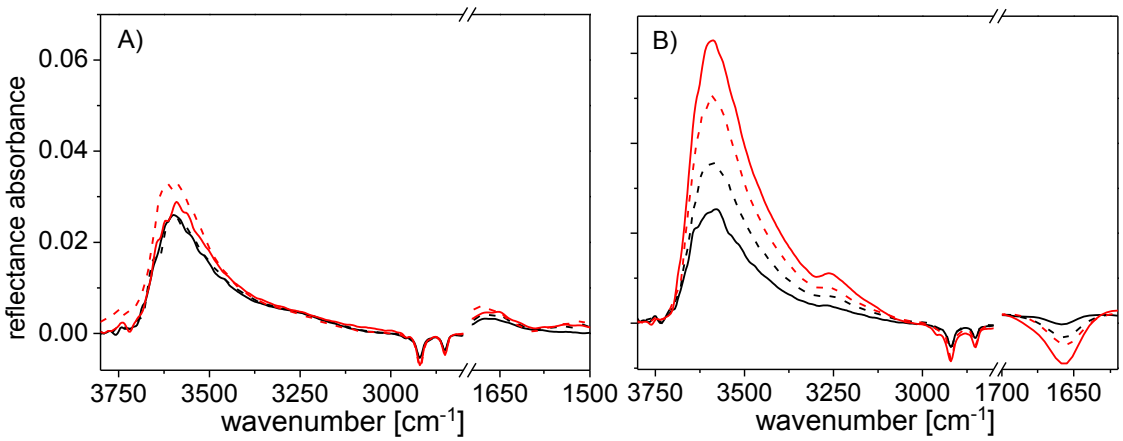

Figure 16: IRRAS on A) DPPG and B) DPPG/LL-32 mixed films. The peptide was injected under a precompressed monolayer with a π_i of 10 mN/m (—), 15 mN/m (- - -), 20 mN/m (—) or 30 mN/m (- - -). The spectra were measured in equilibrium at ~35 mN/m. 40°, p-polarized beam (5 mM HEPES, 100 mM NaCl, pH 7.4, 20°C, 0.2 µM peptide in solution).

The spectra of the condensed DPPG film (Figure 17) show a small increase in the ν(OH) (~ 3600 cm-1) band intensity, dependent on the surface pressure π. Above 8 mN/m, DPPG is in a condensed phase state with an all-trans conformation of the fatty acid chains. Further compression leads to small changes in the packing and the tilt angles. The phase state of the lipids can be concluded from the band position of the symmetric and asymmetric CH_2 vibration, because this vibration is sensitive to the ratio of trans/gauche conformers. It is found to be 2919 cm^{-1} for the $\nu_{as}(CH_2)$ and 2849 cm^{-1} for the $\nu_s(CH_2)$, both before and after the peptide injection. This means a condensed state which is not affected by the peptide. But the peptide leads to changes in the OH-band. At the same time, amide bands (amide A ~3300 cm^{-1}, amide I ~ 1658 cm^{-1}) become apparent. The amide I band position at ~1658 cm^{-1} denotes the presence of the peptide with an α-helical structure. The OH-band intensity is increased[4] in the mixed film compared to the DPPG film, meaning a strong interaction of the peptide with the lipid monolayer, with additional binding under the lipid head groups. This will be verified later.

[4] The intensity change is quiet high, but shows not a direct correlation to π_i. For this reason, further quantitative interpretation was renounced.

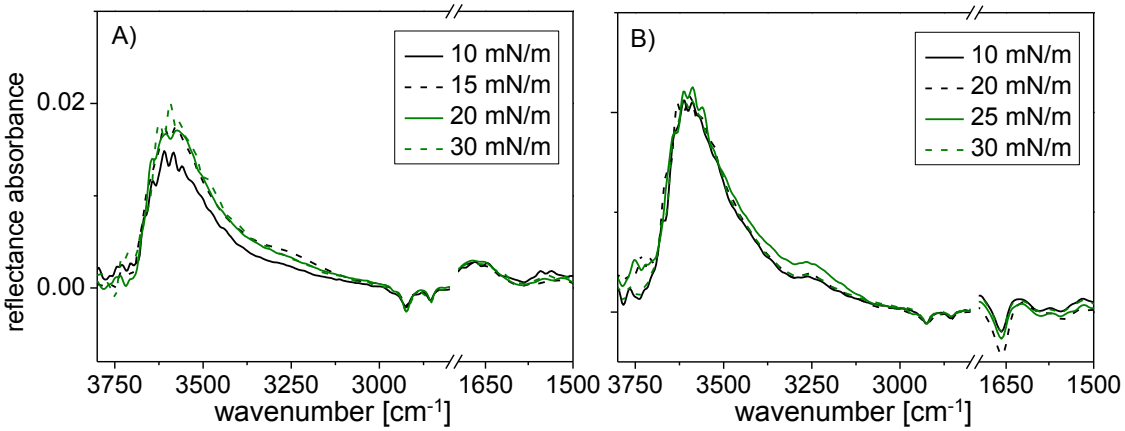

Figure 17: IRRAS on A) POPG and B) POPG/LL-32 mixed films. The peptide was injected under a precompressed monolayer with a π_i of 10 mN/m (—), 15 mN/m (- - -), 20 mN/m (—) or 30 mN/m (- - -). The spectra were measured in equilibrium at ~35 mN/m, 40°, p-polarized beam (5 mM HEPES, 100 mM NaCl, pH 7.4, 20°C, 0.2 µM peptide in solution).

The chains of POPG are fluid at 20°C, leading to $\nu_s(CH_2)$ = 2855 cm^{-1} and $\nu_{as}(CH_2)$ = 2923 cm^{-1}, which is certainly not influenced by the peptide (Figure 18). The intensity of these bands is quite low, since the chains are completely disordered. Condensed chains have a strong packing and thus a better oriented transition dipole moment which leads to a stronger signal in the IR spectrum [180]. A fluid monolayer has a lower packing density of the aliphatic chains; this also contributes to reduced band intensity.

The presence of amide bands illustrates the presence of the peptide in the lipid film. The intensity of the ν(OH) of POPG is almost unchanged after peptide injection, meaning a complete incorporation of the peptide and no formation of an additional layer under the lipid head groups as seen for DPPG .

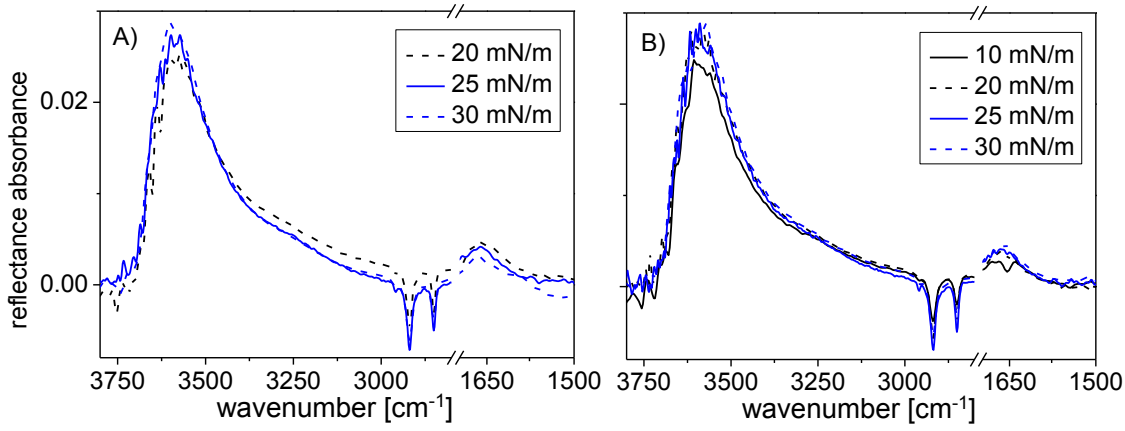

Figure 18: IRRAS on A) DPPC and B) DPPC/LL-32 mixed films. The peptide was injected under a precompressed monolayer with a π_i of 10 mN/m (—), 20 mN/m (- - -), 25 mN/m (—) or 30 mN/m (- - -). The spectra were measured in equilibrium between 25 mN/m and 32 mN/m. 40°, p-polarized beam (5 mM HEPES, 100 mM NaCl, pH 7.4, 20°C, 0.2 µM peptide in solution).

In DPPC/L-32 mixed films (Figure 19), no amide bands were detected for π_i >10 mN/m. For π_i = 10 mN/m only a small dip in the spectrum at 1658 cm^{-1} can be seen. Apart from that, the increase in the surface pressure after the peptide injection ($\pi_{eq}>\pi_i$) denotes an interaction with the lipid interface. An explanation for this is that the peptide binds preferentially to the air/water interface between the DPPC molecules without a further interaction. This can proceed beyond the IR spot. The excess of peptide could stay in solution or adsorb to the bottom of the trough, but does not bind under the lipid monolayer.

4.1.2 Interaction of LL-32 and LL-20 with Uncompressed Monolayers: Condensation and Fluidization are Key Effects

To be sure that the peptides are homogeneously distributed at the lipid interface, the peptide is homogeneously dissolved in the subphase and the lipid solution is spread on the surface. An adsorption of the peptide to the the air/water interface and leads to an interaction with the lipid monolayer. The concentration of the lipid film is chosen such that the initial surface pressure is zero. The increase in surface pressure reflects the peptide's affinity for this type of membrane. Differences in the surface pressure for different model membranes give hint to the selectivity of the peptides [178]. To asess the influence of the peptide on the lipid packing, experiments were done with DPPC or DPPG to mimic mammalian or bacteria cell membranes.

Spreading of the DPPG solution on the peptide-containing subphase leads to a strong increase in the surface pressure (Figure 20 A)). The equilibrium pressure for both peptides is increased in the presence of DPPG (35 mN/m for LL-32 with DPPG and 25 mN/m for LL-32 alone; 22 mN/m for LL-20 with DPPG and 6 mN/m for LL-20 alone). The equilibrium surface pressure is reached much faster for the less active LL-20, indicating additional effects in interaction of LL-32 with the lipids.

The peptide adsoption to DPPC (Figure 20 B)) leads to a surface pressure increase of 8.5 mN/m in the presence of LL-20, and to 25 mN/m in the presence of LL-32. These values are comparable with the peptide adsorption to the bare air/water interface, indicating no specific interaction of the peptides with DPPC. The adsorption isotherm for LL-32 shows again a small plateau at 8 mN/m, conceivably due to a phase transition in the monolayer. This was not observed for LL-20. There, the equilibrium surface pressure is below the surface pressure required to induce the phase transition of DPPC. The results will now be analyzed in detail.

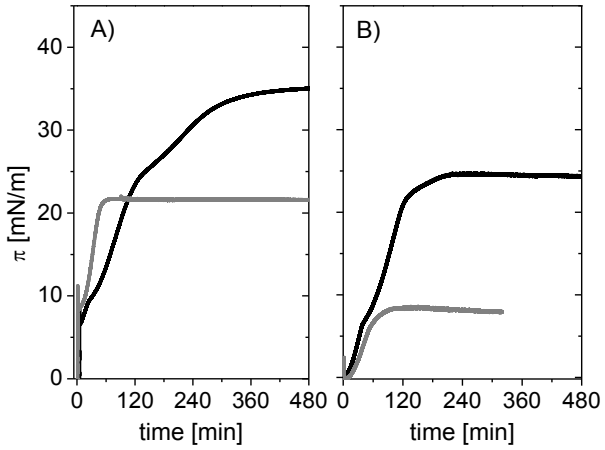

Figure 19: Adsorption isotherms of LL-32 (—) and LL-20 (—) binding to A) DPPG and B) DPPC monolayers. (5 mM HEPES, 100 mM NaCl, pH 7.4, 20°C, 0.2 µM peptide in solution)

4.1.2.1 Infrared-Reflection-Absorption Spectroscopy

A phase transition in DPPC and DPPG monolayers can be seen by a shift in the frequency of the asymmetric CH_2 vibration[5] from 2924…2922 cm^{-1} (expanded) to 2919 cm^{-1} (condensed).

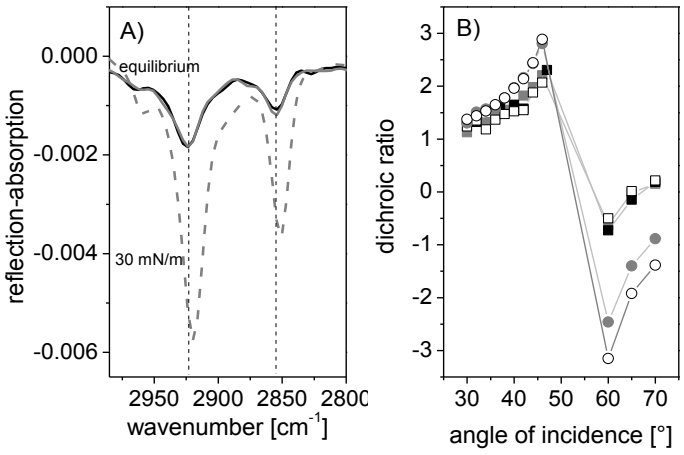

Figure 20: A) CH_2 vibration of DPPG-peptide mixtures with LL-32 at π_{eq} = 38 mN/m (—) and LL-20 at π_{eq} = 22 mN/m (—) and π = 30 mN/m (– – –). B) Dichroic ratio of the asymmetric CH_2 vibration of DPPG at 2854 cm^{-1} at 0 mN/m (□) and π = 30 mN/m (○), of DPPG with LL-32 (■) at π = 38 mN/m and LL-20 at π = 22 mN/m (■) and π = 30 mN/m (●). (5 mM HEPES, 100 mM NaCl, pH 7.4, 20°C, 0.2 µM peptide in solution).

DPPG

Both peptides lead to a fluidization of the monolayer: in equilibrium, the position and the dichroic ratio of the asymmetric CH_2 vibration agree well with those of a DPPG monolayer in an expanded phase (Figure 21). This is surprising, since the equilibrium pressure is much higher than the phase transition pressure of a DPPG monolayer (8 mN/m).

[5] This is analogously valid for the symmetric CH_2 band between 2854 cm^{-1} and 2849 cm^{-1}.

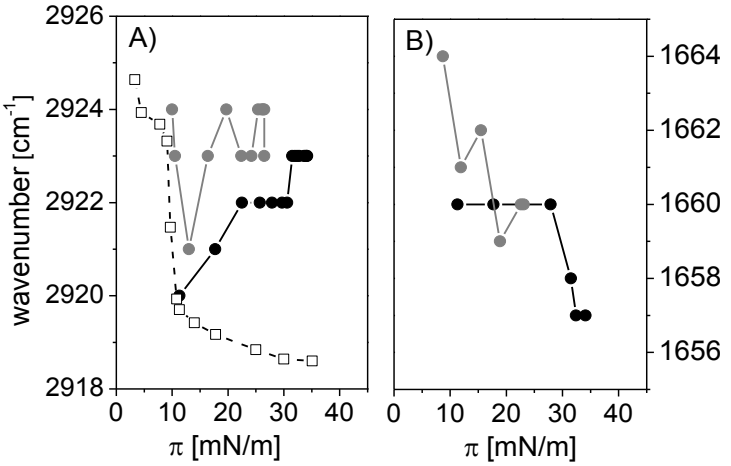

Figure 21: A) Maxima of the asymmetric CH_2 vibration band and B) Maxima of the amide I band, depending on the surface pressure π for DPPG (□) and DPPG/LL-32 (●) and DPPG/LL-20 (●). (5 mM HEPES, 100 mM NaCl, pH 7.4, 20°C, 0.2 µM peptide in solution).

Following the adsorption kinetics with IRRAS (Figure 22A)) shows that LL-32 shifts the methylene vibration to 2920 cm^{-1} (condensed state), which is followed by relaxation to 2923 cm^{-1} (expanded state) for intermediate surface pressures > 20 mN/m. LL-20 shifts the methylene vibration to 2921 cm^{-1} (condensed state) which relaxes to 2923 cm^{-1} (expandend state) for intermediate surface pressures >15 mN/m. That means that the peptide adsorption leads to an acyl chain ordering which is again dissolved by a further peptide-lipid-interaction. In the adsorption isotherm (Figure 20) can be seen that an intermediate equilibrium is reached around 25 mN/m, but additional interaction with the now compressed monolayer leads to a further increase of the surface pressure, indicating a further step in the peptide-lipid interaction.

Additional compression of the DPPG/LL-20 film to 30 mN/m changes the position and intensity of the CH_2 band (Figure 21). The maximum of the asymmetric CH_2 vibration band is found at 2920 cm^{-1}, which differs not from a pure DPPG monolayer at 30 mN/m. The dichroic ratio of the CH_2 band intensity is slightly below the value of the pure lipid. This means a partial squeezing-out of the peptide, but indicates that the peptide is still located at the lipid interface, probably by interacting with the negative charge of the lipid head groups. The LL-32/DPPG mixed film was not further compressed, due to the high equilibrium pressure of the film.

Following the adsorption kinetics, we also observe a shift in the amide I band to lower wavenumbers (Figure 22 B)). A redshift in the amide I band position can be attributed to the formation of hydrogen bonds [162; 181] or a change in the helix flexibility [182]. Also, a change in the backbone hydration influences slightly the band position. This can be due to an aggregation of the peptide [183-185] or a deeper incorporation into a hydrophobic environment which is both connected to a dehydration of the C=O groups. As shown in chapter 3, LL-20 adopts a less dis-

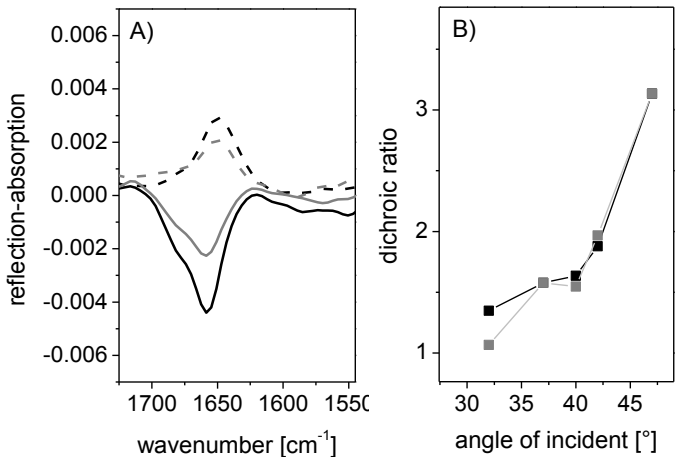

Figure 22: A) Amide band at 40° (solid lines) and 60° (dashed lines) of the peptide/DPPG film after subtraction of pure DPPG monolayer spectra. LL-32 (—), LL-20 (—), p-polarized light B) Dichroic ratio of the amide I band intensity at 1658 cm^{-1} (5 mM HEPES, 100 mM NaCl, pH 7.4, 20°C, 0.2 µM peptide in solution).

tinct α-helix, with more contact to water. The stronger shift for LL-32/DPPG mixtures could be therefore explained by a deeper insertion of LL-32 compared to LL-20 or simply a better formation of an α-helix.

In equilibrium, the amide I band[6] can be fitted with two Lorentzian curves with maxima at 1657.8cm^{-1} and 1679.0 cm^{-} for LL-32 and 1658.1 cm^{-1} and 1668.2 cm^{-1} for LL-20. The high energetic band can be attributed to the vibration of non-hydrogen bonded C=O groups [156].

To compare the orientation of the peptides, the dichroic ratio of the amide I band can be calculated by dividing the signal of the p-polarized light by the signal of the s-polarized light [137; 166]. The dichroic ratio is independent of the concentration or length of the peptides and allows comparisons regarding the orientation in both, in-plane and out-of-plane. The spectrum of pure DPPG at π = 0 mN/m has to be subtracted previously to eliminate the influence of the H_2O bending vibration on the band intensity, because it overlaps with the amide I band. The dichroic ratio of the amide I band is comparable for both peptides, indicating that both peptides adopt a comparable orientation when interacting with DPPG. But the values are slightly below the values of an entire α-helix lying flat at the air/water interface. Moreover, they are comparable to the deviating conformation of LL-20 at the air/water interface.

[6] Differences in the intensity of the spectra originate from the different peptide sizes. The smaller LL-20 contains less peptide bonds which can contribute to the IR spectrum. This was in detail discussed in chapter 3.

DPPC

The interaction of the peptides with DPPC is different from that with DPPG, as can be seen from the surface pressure change upon adsorption of the peptides. The asymmetric methylene vibration of the lipid (Figure 24) shifts for LL-32 to 2920 cm^{-1} and to 2924 cm^{-1} for LL-20. The band intensity increases, since the phase transition of the lipid film from a gauche to an all-trans conformation leads to a change in the orientation of the transition dipole moment, which gives a stronger signal [180]. This effect is increased by the better packing of the condensed molecules, because it increases the number of molecules in the spot, but this effect is eliminated by calculating the dichroic ratio. The dichroic ratio of DPPC/LL-32 agrees with the value of a pure DPPC film at the same surface pressure, confirming a phase transition of DPPC from the expanded to condensed state by the adsorption of LL-32. The adsorption of LL-20 leads does not lead to a condensation of the DPPC monolayer, but it should be mentioned, because the low surface pressure of 8.5 mN/m is too low to induce the phase transition.

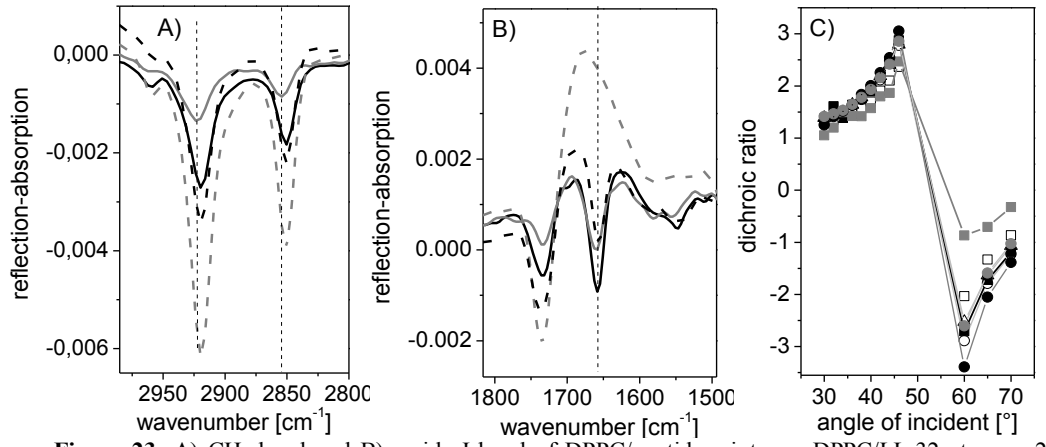

Figure 23: A) CH_2 band and B) amide I band of DPPC/peptide mixtures. DPPC/LL-32 at π_{eq} = 25 mN/m (—) and π_1 = 30 mN/m (- - -), DPPC/LL-20 at π_{eq} = 8.5 mN/m (—) and π_1 = 30 mN/m (- - -) C) Corresponding dichroic ratio of $\nu_{as}(CH_2)$ of DPPC at π = 10 mN/m (□), 25 mN/m (Δ), 30 mN/m (○), DPPC/LL-32 at π_{eq} = 25 mN/m (■) and π_1 = 30 mN/m (●), DPPC/LL-20 at π_{eq} = 8.5 mN/m (■) and π_1 = 30 mN/m (■) (5 mM HEPES, 100 mM NaCl, pH 7.4, 20°C, 0.2 μM peptide in solution).

Compression of the peptide/DPPC films to 30 mN/m leads to a shift in the asymmetric CH_2 vibration to 2919.4 cm^{-1}, both in the absence and in the presence of the LL-20 and LL-32. Moreover, the dichroic ratio of the LL-20/DPPC mixed film and the DPPC film are the same. The absence of amide bands in the spectra (Figure 24 B)) confirms that LL-20 is squeezed out and not located between the lipids anymore. This is not the case for LL-32. The CH_2 vibration has the same position as for pure DPPC, but the band intensity is relatively low and the dichroic ratio is increased. The presence of the amide bands from LL-32 in the spectra indicates that the peptide is still located at the interface (see appendix) and influences the lipid conformation.

4.1.2.2 Grazing Incidence X-ray Diffraction

Film balance measurements and IR spectroscopy give no direct information about the crystalline packing, but GIXD allows the determination of the condensed monolayer structure [160]. The periodicity of the high ordering of condensed fatty acid chains results in a diffraction pattern, when X-rays are diffracted by them. The contour plots show the distribution of scattering intensity as a function of the in-plane scattering vector component Q_{xy} and the out-of-plane scattering vector component Q_z at different lateral pressures [28]. The contour plots of DPPC and DPPG monolayers with and without the peptides are shown in Figure 25. From the positions of the Q-values, the lattice parameters of the unit cell can be calculated, and the tilt angle can be derived. The obtained cross-sectional areas of one chain (approximately 20 $Å^2$, see appendix) and the calculated tilt angles agree with the literature [28; 29; 136; 186; 187].

DPPC

The diffraction pattern of condensed DPPC contains two Bragg peaks and can be attributed to a rectangular lattice [187]. The peak of the L_{02} reflection is located at Q_z=0, the degenerated peak of the L_{11} reflection is located at Q_z >0 $Å^{-1}$. The chains are tilted by 31.8° at 30 mN/m (for more details of the in-plane parameters see appendix).

The addition of neither LL-20 nor LL-32 has significant influence on the diffraction pattern and thus in the packing and the tilt angles. In the DPPC/LL-32 mixtures, the correlation lengths are 670 Å and 100 Å for the equilibrium pressure of 26 mN/m. DPPC at 25 mN/m has correlation lengths of 630 Å and 90 Å, respectively. These are values of the same order, showing that the crystallinity of the monolayer is unaffected and LL-32 is probably excluded from the condensed lipid domains. This is analogously valid for LL-20.

DPPG

For DPPG, three Bragg peaks can be identified, all located at Q_z>0. This is characteristic for an oblique lattice. At 30 mN/m, the chains are tilted to 26.9°. (see appendix).

In contrast to DPPC, the peptides have a strong influence on the scattering properties. The presence of LL-20 decreases the tilt angles to 22.9° at 28 mN/m. This can be due to an increased order in the head group region and could be the result of charge compensation. It was concluded from the MIP experiments that LL-20 is electrostatically bound to the head groups, without exhibiting further interaction. When LL-32 is adsorbed to the DPPG monolayer, no Bragg peaks were found, even at a high equilibrium surface pressure of 38 mN/m. This is consistent with the IRRAS measurements that the adsorption of LL-32 to DPPG leads to a fluidization of the monolayer.

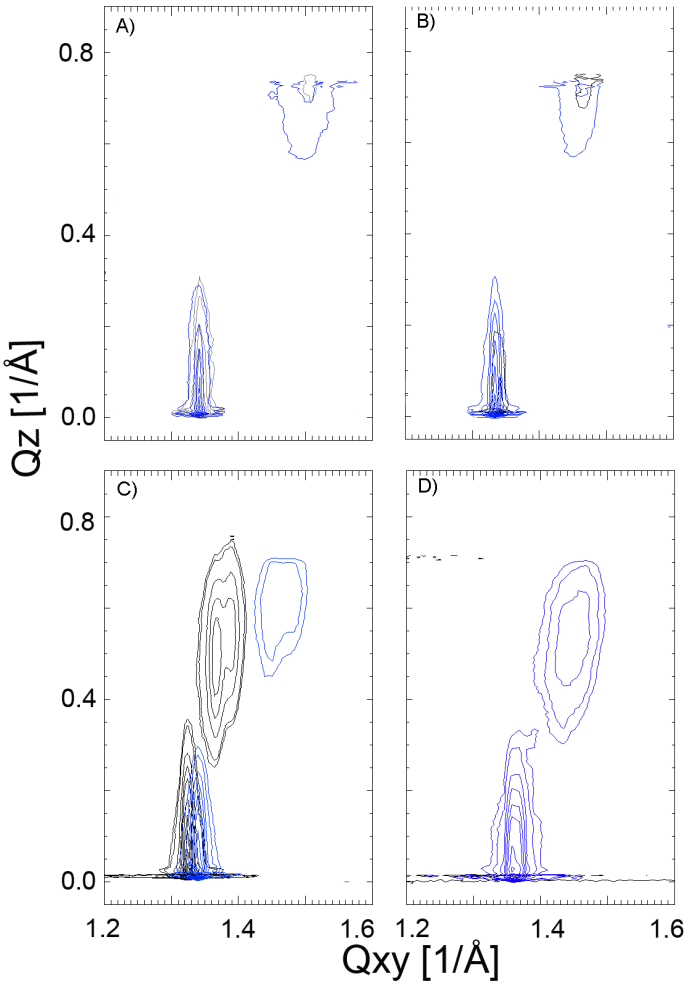

Figure 24: Contour plots of the corrected X-ray intensities as a function of the in-plane (Q_{xy}) and out-of-plane component (Q_z). Shown is an overlay of lipid/peptide mixtures at π_{eq} (—) and pure lipid monolayers at comparable π (—). A) DPPC and DPPC/LL-20 B) DPPC and DPPC/LL-32 C) DPPG and DPPG/LL-20 D) DPPG and DPPG/LL-32 (no Bragg peaks are found for DPPG/LL-32). (5 mM HEPES, 100 mM NaCl, pH 7.4, 20°C, 0.3 µM peptide in solution)

4.1.2.3 Specular X-Ray Reflectivity

Specular X-ray reflectivity (XR) is based on the interference between X-rays reflected at various depths in the monolayer [29]. XR measurements can help to clarify and identify the position of the peptide in the lipid monolayer, since XR provides the electron density profile at the surface [135] and can help to distinguish between a penetration of the peptides into the hydrophobic chain region and an adsorption of the peptides to the head group region. The electron density profile can be fitted with boxes of a certain thickness, roughness and electron density. From that, the orientation and the film thickness at the interface can be estimated.

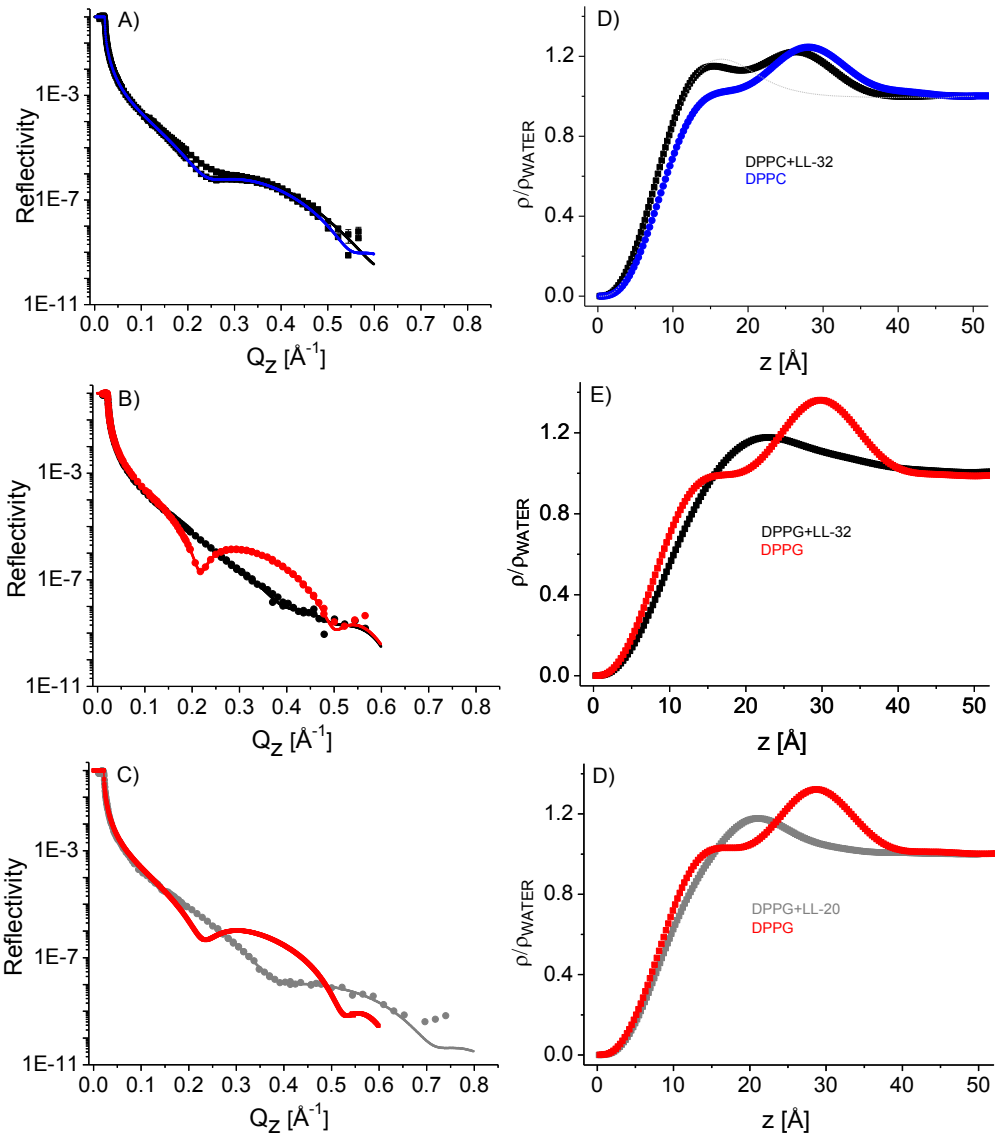

Figure 25: A-C) X-ray reflectivity and D-F) calculated electron density profile of DPPC/peptide and DPPG/peptide mixtures at π_{eq}. Q_z is the out-of-plane scattering vector, ρ/ρ_{WATER} denotes the electron density normalized to water, z is the distance from the air/water interface towards the subphase. Lipid/LL-32 (—), lipid/LL-20 (—). Pure DPPC (—) and DPPG (—) monolayers at equivalent surface pressure are plotted for comparison. (5 mM HEPES, 100 mM NaCl, pH 7.4, 20°C, 0.3 µM peptide in solution)

DPPC and DPPG show a characteristic electron density profile (Figure 26) which can be fitted with two boxes for the head group and the tail region, respectively (see Table 4). The smaller boxes can be attributed to the lipid head group while the larger box of ~ 16 Å with the lower electron density corresponds to the fatty acid tail.

The electron density curves of the mixtures peptides/DPPG do not allow the clear distinction between chain and head group as for the pure lipid. This is due to the deep penetration of the peptides between the lipids, which smears the transition between the two constituents. Nevertheless, the curves could be best fitted assuming 4 boxes. For LL-32, the first box of 4.4 Å can be attributed to a diluted CH_2 layer, as seen by the small relative electron density of only 0.16. The second box of 6.5 Å corresponds to the mixed CH_2/peptide region. The peptide is incorporated into the chain region of the lipids. The third box of 12 Å corresponds to a mixed peptide/lipid head group layer. The fourth box in the DPPG/LL-32 mixture has a thickness of 17.0 Å. That corresponds to the upper limit of a helix diameter [135] and indicates a second peptide layer bound under the DPPG monolayer, but could also arise from a peptide chain hanging out of the interface. The peptide carries a kink at Lys12, which breaks the helix into two helices [99] and the residues 1-12 are inactive against any cell type [110], so the interaction of the peptide with the DPPG film should be dominated by the second helix (residues 13-32). The first helix has a theoretical length of 18 Å, so the fourth box in the electron density profile could also be related to the first helix, hanging towards water. The small electron density of that box arises from a diluted peptide adsorption layer. The peptides oriented normal to the interface are less tightly packed than the ones parallel to the interface. The DPPG/LL-20 film shows a similar reflectivity profile. But the fourth box has a thickness of only 5.7 Å. Due to the reflectivity profile of the peptide adsorbed to the air/water interface (chapter 3), this box can be attributed to an unstructured contribution of the peptide.

Table 4: Data obtained from XR experiments. π – surface pressure, d-thickness of the box, ρ/ρ_{water}-electron density normalized to water (ρ_{water}= 0.334 $e^-/Å^3$), roughness means the roughness of the calculated box.

	π [mN/m]	d [Å]	ρ/ρ_{water}	roughness [Å]
DPPC	30	15.9	1.03	3.36
		5.3	1.53	3.63
				6.01
DPPC, LL-32	26	15.2	1.12	3.2
		9.1	1.24	2.0
		11.9	1.05	2.9
				15.3
	30	16.7	1.10	3.4
		3.13	1.85	3.5
				5.8
DPPG	28	16.3	1.03	3.36
		9.1	1.38	2.77
				3.70
	38	16.6	0.99	3.41
		10.4	1.40	3.06
				3.28
DPPG, LL-20	28	3.7	0.17	1.7
		7.7	0.71	2.8
		5.7	1.48	4.6
		5.9	1.08	4.5
				8.5
DPPG, LL-32	38	4.4	0.16	1.9
		6.5	0.77	3.1
		12.0	1.26	3.9
		17.0	1.02	8.2
				11.0

4.2 Comparison to Measurements in Bulk

To compare the monolayer experiments with experiments in bulk, we performed CD experiments with the peptides and lipid vesicles (Figure 27). Due to the high absorbance of NaCl and HEPES in CD spectroscopy, the experiments were performed in ultrapure water [154]. There, both peptides are unstructured (see chapter 3). The helical content was calculated to < 1% for both peptides, also for a NaCl concentration of 100 mM. The addition of POPC vesicles to the peptide solution has little effect on the peptide conformation. The CD spectra correspond still to an unstructured peptide [31; 154], although the intensity at 230 nm increases little. However, the addition of POPG vesicles leads to a change in the peptide conformation of both LL-32 and LL-20. A positive band at 193 nm and two negative bands at 207 and 222 nm emerge. These bands are indicators for an α-helix [31; 34; 154]. A formation of transmembrane pores in equilibrium can be excluded, since transmembrane pores lead to a redshift of the positive band in the range of 195-200 nm and a higher intensity of the band at 222 nm compared to 208 nm [34; 151].

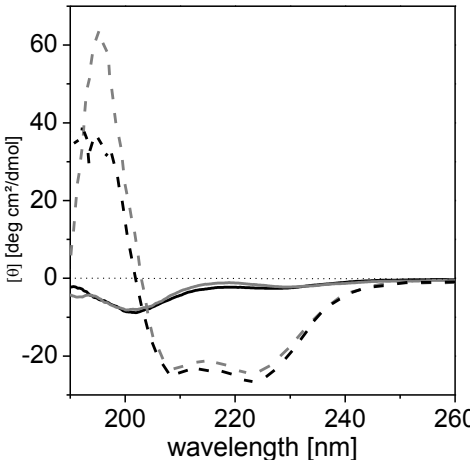

Figure 26: CD spectra of LL-32 (—) and LL-20 (—) in water in the presence of POPC vesicles (solid lines) and in the presence of POPG vesicles (dashed lines). Peptide:lipid = 1:16. Measurements were done in water at 20°C.

4.3 Discussion

The interaction of two peptides with model membranes, including vesicles and lipid monolayers, has been investigated to point out differences in their mode of action. The peptides are fragments of the human antimicrobial LL-37 and show contrary behavior in biological experiments. While LL-32 is more active compared to the mother peptide, LL-20 is active only at very high concentrations [143; 145]. Lipid monolayers composed of DPPG, POPG, DPPC and DOPC were formed to clarify how the lipid charge and the lipid phase state influence the lipid/peptide interaction. Surface sensitive IRRAS, GIXD and XR measurements were coupled to Langmuir film balance measurements to obtain details on a molecular level. The results were compared to CD experiments with vesicles composed of POPC and POPG, respectively.

As shown in chapter 3, both peptides are surface active. This surface activity is enlarged by the presence of lipids. The equilibrium surface pressure for LL-32 at lipid monolayers is quite high (38 mN/m with DPPG, 25 mN/m with DPPC). LL-20 is less surface active and shows also a smaller equilibrium surface pressure in the presence of lipids (22 mN/m with DPPG and 8.5 mN/m with DPPC). Moreover, the adsorption of both peptides to DPPC monolayers is comparable with the adsorption to the air/water interface.

Maximum Insertion Pressure (MIP) measurements revealed the critical surface pressure, up to which the peptides interact with lipid monolayers of a certain composition. For an interaction with a cell membrane, the MIP should be higher than 30…35 mN/m, because this value corresponds to the lateral pressure in a membrane [37; 38]. The different MIPs and the corresponding slopes in the fit support the fact, that LL-32 is the more active peptide, and show that the mode of action is

different, even between the different lipid monolayers. The low MIPs of LL-20 into DOPC and DPPC monolayers indicate that the peptide will not spontaneously insert into zwitterionic regions of cell membranes. The interaction of LL-20 with negatively charged lipid monolayers shows the dependence from the lipid phase state, as concluded from the MIP experiments. Injection of LL-20 under pre-compressed DPPG monolayers led to a constant increase in the surface pressure, independent from the initial surface pressure π_i. The strong electrostatic attraction of LL-20 to the negatively charged head groups of condensed DPPG could hinder a penetration of the peptide into the tightly packed DPPG monolayer while the peptide exhibits normal interaction with the fluid POPG monolayer. GIXD experiments showed that LL-20 lowers the tilt angle of DPPG. Probably, LL-20 compensates the charges of the DPPG head groups, which improves the lipid packing. The resulting local 'gaps' could be used for the adsorption of the peptides to the air/water interface, since the now charge-compensated lipids have no attraction to the peptide, and the peptide does not interact with neutral lipids, as shown.

LL-32 shows a strong affinity for both zwitterionic and negatively charged lipid monolayers and an interaction at physiological relevant surface pressures (30…35 mN/m [37; 38]). LL-32 completely penetrates the fluid POPG monolayers for π<MIP, but forms an additional layer under DPPG monolayers.

The differences in the surface activity and MIPs for different lipids are indicative for a different way of action of the peptides [178] and mean a kind of selectivity of the peptide towards different membrane compositions.

Both peptides have no influence on DPPC monolayers. The CH_2 band position and the diffraction pattern of the DPPC/peptide films are undistinguishable from reference measurements of DPPC. As can be concluded from the correlation length of ~ 650 Å and ~100 Å, the crystallinity of the DPPC film is unaffected by the peptide adsorption. The peptides probably adsorb in clusters between the DPPC molecules, leaqding a coexistence of two phases: a condensed lipid phase and a peptide phase. Compression of the peptide-mixed films leads to a squeezing-out of LL-20, but not LL-32, as concluded from the dichroic ratio of the CH_2 band and the qualitative analysis of the amide I band.

For DPPG monolayers, the CH_2 band position in the IRRA spectra are related to an expanded lipid phase and the lack of Bragg peaks in GIXD experiments indicate a fluidization of the lipid film. Following the adsorption kinetics shows that the peptide adsorption leads to a prior condensation of DPPG monolayers. The condensed lipid domains serve as a target for a further peptide-lipid interaction. While the peptide completely incorporates into pre-compressed POPG films, the peptide injection under DPPG monolayers leads to additional binding beneath the head groups, as concluded from the electron density profile. But the formed layer under the DPPG head

groups differs in the thickness. The second layer of LL-32 is 17 Å thick and can be attributed to an α-helix, both being parallel or perpendicular to the interface. The peptide carries a kink at Lys12, which breaks the α-helix into two parts [99]. Since the second helix corresponds to the active part of the peptide [117; 188], the first helix could hang out of the interface, leading to a sublayer with a theoretical thickness of 18 Å. It was concluded that the second layer of LL-20 corresponds mainly to an unstructured peptide, which compensates the charges of DPPG, because LL-20 lacks the part identified as antimicrobial core LL-$37_{18\text{-}29}$ [88]. The peptide is electrostatically bound to the head groups, but possibly with an irregular conformation. Both peptides adopt an α-helical conformation with a comparable orientation, as concluded from the amide I band position and the corresponding dichroic ratio for several angles of incidence. Compared to the values of the air/water interface, both peptides lie partly parallel to the surface, but contain deviating conformations. LL-32 contains a helix perpendicular to the interface and the layer of LL-20 contains unstructured peptides. Both cases lower the dichroic ratio (see chapter 3 and [137]).

The peptides are both unstructured in solution, but adopt a helical conformation when bound to POPG vesicles. Transmembrane helices could not be observed in the equilibrium state. POPC vesicles have no effect on LL-20 and LL-32 in water; the CD spectra are almost unchanged.

To decide, if the unstructured peptides are bound to the POPC vesicles, some calculations can be done. The theoretical change in the Gibbs energy ΔG_{wif} for the transition of the unstructured peptides from water to a POPC interface can be calculated with the help of Mpex [148] by using the White-Wimley scale [36]. This is a simple model to evaluate, if the adsorption of the unstructured peptides to a hydrophilic-hydrophobic interface is energetically possible.

$\Delta G_{wif,LL\text{-}20}$ = 6.86 kcal/mol for LL-20 and $\Delta G_{wif,LL\text{-}32}$ = 9.28 kcal/mol for LL-32, indicating that binding of the unstructured peptide to POPC is energetically unfavorable. ΔG can be reduced by the formation of hydrogen bonds with the formation of α-helices, which reduces ΔG to -0.4 kcal/mol per residue [189]. To gain in energy, and change the sign in ΔG_{wif}, the helical content has to be ≥ 73% for LL-32 and ≥ 86% for LL-20. Therefore, the unstructured peptides are not bound to the POPC vesicles.

It was shown that LL-32 fluidizes negatively charged DPPG monolayers, it penetrates into zwitterionic DOPC monolayers, but it exhibits no special interaction with DPPC. It was expected that LL-32 shows also an interaction with zwitterionic lipids, because the peptide is haemolytic [143; 145]. Is this in contrast to monolayer experiments? Also, it remains open, why LL-32 does not lead to a fluidization of pre-compressed DPPG monolayers. In the next chapter, the membrane model will be more adapted to a natural membrane by incorporating sphingomyelin to the monolayers. This will help to answer those questions.

5 Peptide Interaction with Mixed Lipid Monolayers Containing Sphingomyelin

Abstract

Biological membranes contain a mixture of thousands of lipids and proteins. Besides phosphatidylcholine (PC), sphingomyelin (SM) is the major constituent of human erythrocytes. The interaction of LL-32 and LL-20 with lipid monolayers containing both, PC and SM has been examined. The results show a clear dependency on the heterogeneity of the lipid film for the interaction of LL-32.

First, the influence of SM on the DPPC packing within a monolayer has been investigated. It could be shown that SM exhibits like DPPC a phase transition from the expanded to the condensed phase and that at 30 mN/m condensed SM molecules are tilted by 18.1° while DPPC is tilted by 31.8°. Incorporation of SM to DPPC monolayers (50:50) resulted in an intermediate tilt angle of 23.2° and a coexistence of two phases over a wide pressure range. LL-32 interacts differently with SM-containing lipid monolayers compared to PC monolayers. It was concluded from MIP experiments that the peptide strongly binds to the lipids if there is a coexistence of fluid and condensed phases.

In a second part, DOPS was incorporated into the DPPC/SM mixed films to mimic cancer cells, since cancer cell membranes contain an increased amount of DOPS in the outer leaflet. DOPS had no influence on the isotherm and the IRRA spectra, but led to a changed diffraction pattern. Though the equilibrium surface pressure of the peptide was slightly increased by the presence of DOPS, the results could not prove a stronger interaction.

Finally, the obtained results were compared to DOPC and DOPC/SM/DOPS mixtures, which exhibited no phase transition to the condensed phase. The interaction of LL-32 with these mixtures was unaltered by the incorporation of SM and DOPS.

It is concluded that LL-32 inserts into L_d phases and binds to L_o phases, but inserts preferentially into membranes exhibiting a L_d-L_o phase coexistence.

5.1 Characterization of the Mixed Lipid Films

5.1.1 SM Influences the DPPC Phase Transition

In the previous chapter, a clear influence of LL-32 on DPPC monolayers could not be observed, though a haemolytic effect of the peptide was observed [143; 145]. Natural membranes are certainly more complex, than a simple monolayer of DPPC or DOPC. For that reason, the model membrane was extended. Besides PCs, sphingomyelin (SM) is a basic module of the mammalian cell membrane (50% of the total lipid amount in the outer leaflet of erythrocytes[14]). SM influences the packing of the membrane and is together with cholesterol involved in the formation of lipid rafts (see introduction). Commercially available is SM with defined chain length, but also brainSM, a mixture of SM with different chain lengths (50% 18:0, 21% 24:1, 7% 22:0, 5% 20:0, 5% 24:0, 2% 16:0 fatty acid distribution). SM monolayers with chain length of 18:0, 20:0, 22:0, 24:0 can exhibit a phase transition from the expanded to the condensed phase on water [190]. That means that 67% of the SM molecules in the brainSM[7] mixture can form condensed films at high surface pressure. This results in a kink in the isotherm of SM (Figure 28 A), red curve). The critical surface pressure for the phase transition π_{pt} is shifted to higher π compared to 18:0 SM (between 5 and 10 mN/m) [190; 191], reflecting a retarded phase transition due to the high amount of unsaturated chains. A squeezing-out of fluid molecules by the formation of condensed domains changes the compressibility of the film, which leads to a coexistence over a wide pressure range, as can be concluded from the deviation from a horizontal line. This is validated in the following experiments.

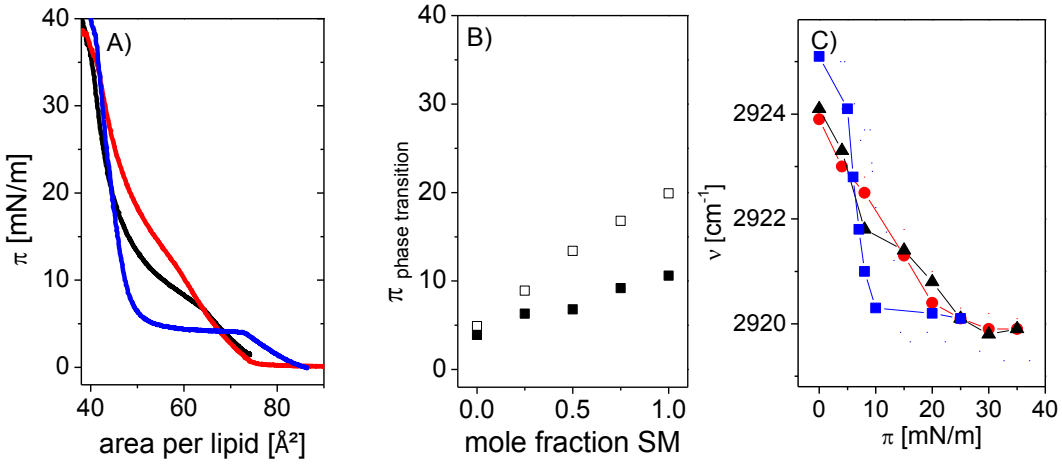

Figure 27: A) Isotherms and B) onset (■) and extrapolated end surface pressure (□) of the coexistence region for DPPC monolayers containing different mole fractions of SM. See text for description. C) Maximum in the asymmetric CH_2 vibration, depending on the surface pressure π. DPPC (—), DPPC/SM (50:50) (—) and SM (—). (5 mM HEPES, 100 mM NaCl, pH 7.4, 20°C)

[7] In the further text SM denotes the mixture of brainSM

5.1.1.1 IRRAS

In Figure 28 C), the maximum in the asymmetric CH_2 band position is plotted as a function of the surface pressure. This maximum is shifted to lower wavenumbers with increasing π, supporting the assumption of a phase transition. But compared to DPPC, where the phase transition occurs at defined π_{PT} =5 mN/m, the phase transition of SM is blurred over a wide surface pressure range. This originates from the exclusion of molecules with unsaturated chains which cannot undergo a phase transition to the condensed phase and underlines the coexistence of two phases over a wide pressure range.

The DPPC/SM (50:50) mixture behaves similar to SM, but the phase transition region is shortened compared to SM. During the phase transition of DPPC, the CH_2 band position shifts from 2924 to 2919 cm^{-1}. For SM and DPPC/SM, this shift is broadened to 20 mN/m. For higher π, the CH_2 band position agrees with the values for the pure DPPC, indicating the condensation of the film.

In the DPPC/SM mixture, the critical surface pressure for the phase transition π_{PT} depends on the mole fraction of SM (Figure 28 B)). The maximum surface pressure of the transition region was extrapolated by drawing tangent lines in the isotherms. The intersection point of the lines was defined as the end surface pressure of the coexistence region, whereas the starting point was defined by the kink in the isotherm. It is obvious that the width of the phase transition region is blurred with increasing SM content, because it increases the number of molecules in the film which cannot condense.

5.1.1.2 GIXD

With the help of the GIXD experiments it is possible to distinguish between a mixed or phase separated film of the condensed DPPC/SM monolayer and to obtain information on the crystalline structure of the film. In a phase separated film, the pure DPPC and SM diffraction pattern would be part of the diffraction pattern of the DPPC/SM mixed film [192; 193]. The miscibility of the compounds leads to a distinctive pattern. An overlay of the contour plots of SM, DPPC and the DPPC/SM mixture at 30 mN/m is shown in Figure 29.

GIXD measurements of SM monolayers led to a diffraction pattern with a broad Bragg peak of low intensity. Additionally, the Bragg peak decays in the direction of smaller Q_{xy} values and higher Q_z values, indicating a superposition. The Bragg rod and Bragg peak profile can be best fitted assuming 2 peaks with $Q_z>0$, meaning a NNN tilt. At 30 mN/m, the molecules are tilted by18.1°.

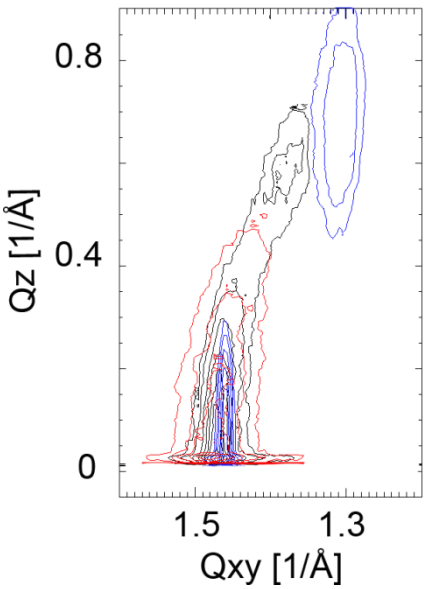

Figure 28: Contour plots of the corrected X-ray intensities as a function of the in-plane (Q_{xy}) and out-of-plane component (Q_z). Shown is an overlay of the SM (—), DPPC (—) and DPPC/SM (50:50) (—) monolayers at 30 mN/m (5 mM HEPES, 100 mM NaCl, pH 7.4, 20°C).

The DPPC monolayer results in a diffraction pattern clearly composed of two Bragg peaks, meaning a centered rectangular lattice with a 31.8° tilt at 30 mN/m (this was discussed in detail in chapter 4).

In the diffraction pattern of the DPPC/SM mixed film, clearly 3 peaks can be identified. Analysis of the peak position and the Bragg rod profile gives a tilt angle of 23.2° at 30 mN/m which is reduced compared to DPPC, but increased compared to SM. The diffraction pattern differs clearly from that of pure DPPC and SM, meaning that both types of lipids influence each other, leading to a different packing mode. The reduced correlation lengths of 167 Å, 34 Å, and 73 Å indicate a monolayer with an increased number of defects.

The Bragg peak and Bragg rod profiles for several surface pressures and the derived packing parameters of the unit cell can be found in the appendix.

5.1.2 Incorporation of 10 mol % DOPS Reduces Strong Packing

Incorporation of 10 mol % DOPS into the DPPC/SM monolayer had only little influence on the shape of the isotherm and the CH_2 band position (Figure 30).

The diffraction pattern (Figure 31) reveals that the incorporation of DOPS influences the packing within the monolayer. The pattern consists of one broad peak with a low intensity. Analysis of the Bragg rod profile indicates that this peak is a superposition of two peaks, but one with Q_z=0, meaning a NN tilt. Additionally, the intensity of the second peak is reduced with

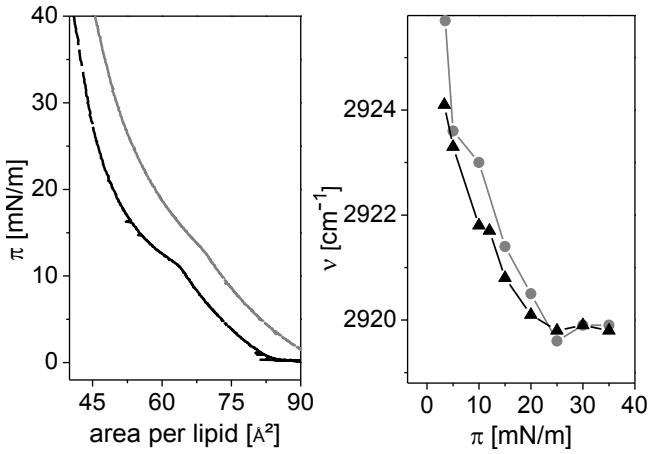

Figure 29: (A) Isotherm and (B) asymmetric CH_2 band position of DPPC/SM (50:50) (—) and DPPC/SM/DOPS (45:45:10) (—) (5 mM HEPES, 100 mM NaCl, pH 7.4, 20°C)

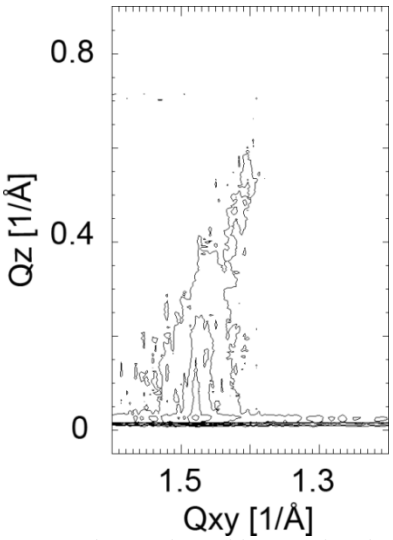

Figure 30: Contour plots of the corrected X-ray intensities as a function of the in-plane (Qxy) and out-of-plane component (Qz) of DPPC/SM/DOPS (45:45:10) at 30 mN/m (5 mM HEPES, 100 mM NaCl, pH 7.4, 20°C)

increasing surface pressure. Besides, L_z is increased to 20.1 Å. The obtained tilt angle is with 22.3° at 30 mN/m only slightly changed compared to DPPC/SM.

5.2 Influence on the Peptide Interaction

5.2.1 How SM and DOPS Incorporation into DPPC Monolayers Influence the Interaction with the Peptides

The interaction of the peptides LL-32 and LL-20 with DPPC/SM (50:50) and DPPC/SM/DOPS (45:45:10) monolayers has been investigated and compared to the results obtained with DPPC monolayers.

The adsorption of LL-32 to the uncompressed DPPC/SM monolayers (π_i=0) leads to an increase in the surface pressure to 23.5 mN/m and to 26.5 mN/m in the case of DPPC/SM/DOPS monolayers (Figure 32), which is comparable to DPPC (25 mN/m). LL-20 leads to a surface pressure of 10 mN/m for adsorption to DPPC/SM and to 12 mN/m to DPPC/SM/DOPS, which is slightly increased compared to DPPC (8.5 mN/m). The time for reaching the equilibrium is for both peptides enlarged compared to DPPC. The following results demonstrate clear differences in the way of action of the peptides with the SM-mixed films compared to DPPC.

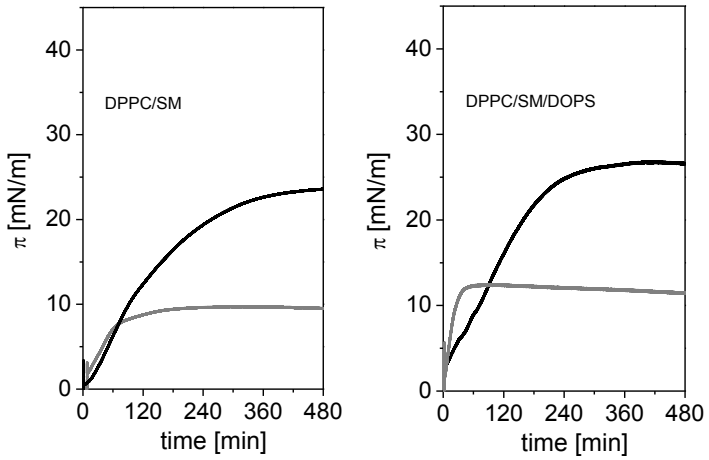

Figure 31: Time-dependend change in the surface pressure π upon adsorption of LL-32 (—) and LL-20 (—) to DPPC/SM (50:50) and DPPC/SM/DOPS monolayers (45:45:10).
(5 mM HEPES, 100 mM NaCl, pH 7.4, 20°C, 0.2 µM peptide in solution).

The adsorption of LL-32 shifts the CH_2 bands of DPPC to 2919.2 cm^{-1} and 2850.1 cm^{-1}, which corresponds to pure DPPC at comparable π (see chapter 4). The adsorption to DPPC/SM shifts the band position to only 2922.8 cm^{-1} and 2853.1 cm^{-1} for, indicating a fluidization of the film (Figure 33). This was also observed for DPPC/SM/DOPS (see appendix). Compression of the LL-32/DPPC/SM film to 30 mN/m leads only to a marginal shift to 2922.2 cm^{-1} and 2852.3 cm^{-1}. The intensity of the amide I band is unchanged. Further compression to 35 mN/m shifts the CH_2 bands to lower wavenumbers (2920.3 cm^{-1} and 2851.9 cm^{-1}), but these values are still slightly increased compared to DPPC/SM. The amide I band is unchanged in intensity, but the position shifts from

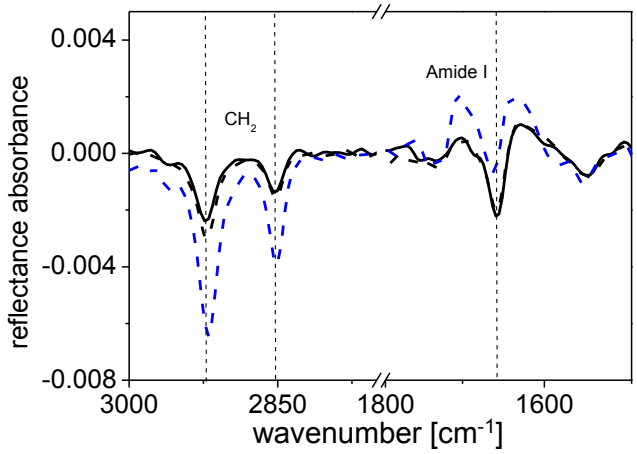

Figure 32: IRRA spectra of mixed films of DPPC/SM/LL-32 at π_{eq} = 23.5 mN/m (—), π_1 = 30 mN/m (- - -) and π_2 = 35 mN/m (- - -) (5 mM HEPES, 100 mM NaCl, pH 7.4, 20°C, 0.2 µM peptide in solution).

1658.3 cm^{-1} to 1658.8 cm^{-1} (30 mN/m) and 1663.4 cm^{-1} (35 mN/m), reflecting more contact with water. But the peptide remains bound to the lipids.

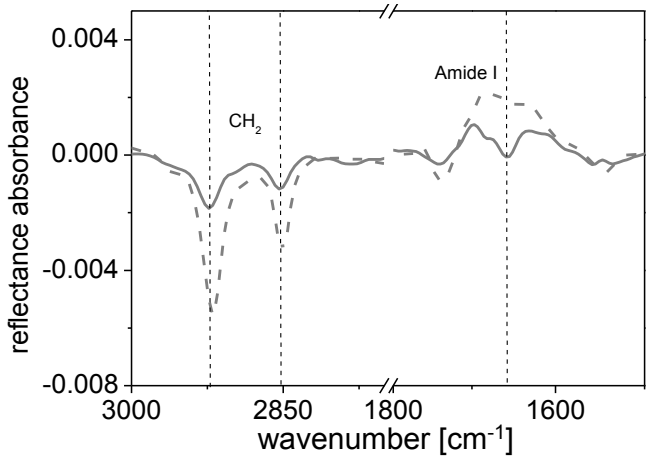

Figure 33: IRRA spectra of mixed films of DPPC/SM/LL-20 at π_{eq} = 10 mN/m (—) and π_1 = 25 mN/m (- - -) (5 mM HEPES, 100 mM NaCl, pH 7.4, 20°C, 0.2 µM peptide in solution).

The adsorption of LL-20 to DPPC/SM shifts the asymmetric CH_2 band to 2923.3 and 2853.9 cm^{-1} (Figure 34), this agrees with the values of the pure DPPC/SM film at this pressure (Figure 28). The amide I band has a maximum at 1657.7 cm^{-1}. The compression of the mixed film leads to a complete squeeze-out of the peptide. At 25 mN/m, the peptide is not bound to the lipids anymore. The small dip in the spectrum arises from the SM backbone and is found in every spectrum of SM mixed films. The sphingosine is connected with the fatty acid via an amide bond. This contributes to the IR spectrum. The position of the CH_2 band maximum is shifted to 2919.9 cm^{-1} and 2851.2 cm^{-1}, which is comparable to the lipid monolayer without the peptide. LL-20 shows no increased interaction by the incorporation of SM.

5.2.1.1 GIXD

To obtain more details about the structure of that film, GIXD was performed on the mixed films. Due to the lack of interaction of LL-20 with DPPC/SM and time restrictions at the beam line, GIXD measurements were only done for LL-32.

The presence of LL-32 in the mixed DPPC/SM film leads to a modified diffraction pattern compared to DPPC/SM alone. At equilibrium pressure, the diffraction pattern is composed of a broad peak with very low intensity, which can be best fitted with two Lorentzian curves. The diffraction pattern shows similarities to raft-like domains with cholesterol [194], indicating a high ordering of the chains which contribute to the diffraction pattern. LL-32 reduces the crystallinity of the film, but some tightly packed domains still exist. The Q_{xy} values of 1.472 Å and 1.516 Å with the Q_z values of 0.183 Å and 0 Å correspond to orthorhombic packing with NN tilt of 8.3°. The diffraction pattern shows similarities with the pure DPPC/SM/DOPS monolayer, reflecting a reduced number of ordered domains which contribute to the diffracted signal.

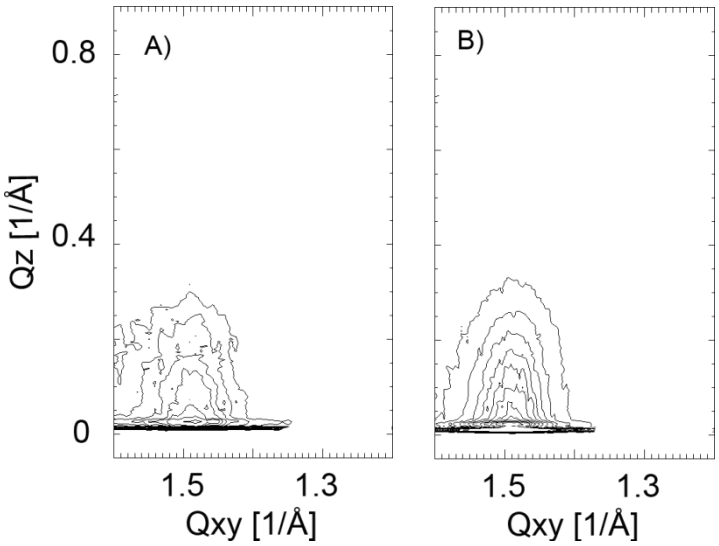

Figure 34: Contour plots of A) DPPC/SM/LL-32 mixed film and B) DPPC/SM/DOPS/LL-32 mixed film, π = 35 mN/m (5 mM HEPES, 100 mM NaCl, pH 7.4, 20°C, 0.3 µM peptide in solution).

The small tilt angle indicates a decreased mismatch between head group and chain area requirements. The compression of the film does not lead to a squeeze-out of the peptide. The signal is still low and the packing parameters are almost unchanged. The contour plot of the compressed film is shown in Figure 35 (for details see appendix).

The adsorption of LL-32 to DPPC/SM/DOPS resulted in a destruction of the crystalline order. At equilibrium pressure, no Bragg peaks can be detected. The compression of the film to 35 mN/m results in a diffraction pattern comparable to that of the LL-32/DPPC/SM film with a tilt

angle of 8.7°. Maybe, some SM molecules with long chains are less well miscible and phase separated only at higher surface pressures. The long scattering length of L_z = 23.2 Å supports this assumption.

5.2.1.2 Injection under Pre-Compressed Monolayers: Dependence on the Lipid Phase State

The peptides were injected under pre-compressed lipid monolayers with defined surface pressures π_i. The equilibrium surface pressure $\pi_{eq=} \pi_i+\Delta\pi$ was estimated and $\Delta\pi$ was plotted versus π_i. A linear fit with an extrapolation to $\Delta\pi$=0 gives the MIP. A MIP higher than 30…35 mN/m means that the peptide would interact with a membrane, since this surface pressure corresponds to the lateral pressure in a membrane [37; 38].

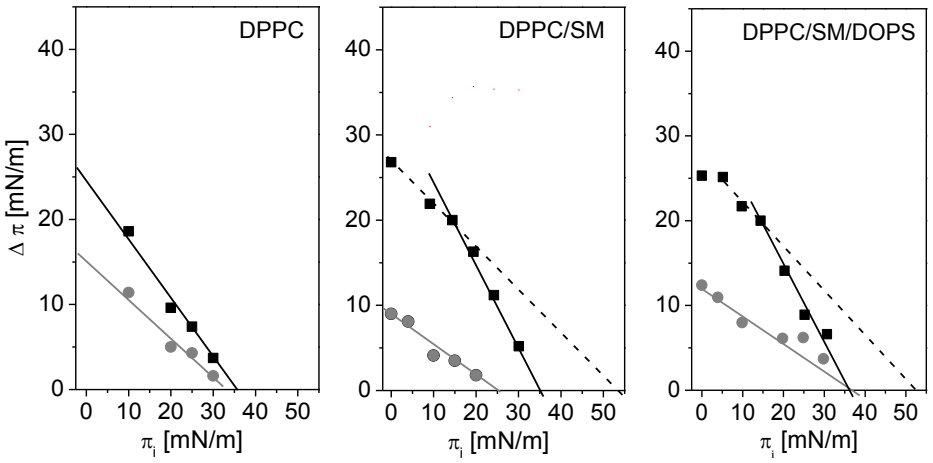

Figure 35: Maximum Insertion Pressure experiments of LL-32 (■) and LL-20 (●) with DPPC, DPPC/SM (50:50) and DPPC/SM/DOPS (45:45:10) monolayers and linear fit to estimate the MIP. (5 mM HEPES, 100 mM NaCl, pH 7.4, 20°C, 0.2 µM peptide in solution).

The results are shown in Figure 36. LL-32 has a MIP[8] of 35 mN/m, which is the same as all mixed monolayers with DPPC. But the MIP of LL-32 depends strongly on the phase of the lipid monolayer. The data points deviate from the linear fit for the expanded phase and the expanded/condensed coexistence region, reflecting dependence from the compressibility of the lipid monolayer. In DPPC monolayers, the phase transition occurs at defined π_{PT} = 5 mN/m while in DPPC/SM monolayers, the phase transition is blurred up over a wide pressure range. This leads to a MIP of 52 mN/m for $\pi_i \leq$ 15 mN/m. The peptide shows a higher interaction with the heterogeneous lipid film, because the overall fluidity of the film is unaffected by the presence of

[8] The MIP values are ±3 mN/m.

few domains. Only when the condensed phase becomes dominant, the monolayer becomes stiff [195].

The incorporation of 10 mol % DOPS to the DPPC/SM mixture has no influence on the interaction with LL-32. Like for the DPPC/SM monolayer, the data can be best fitted assuming two different lines. This leads to a MIP of 52 mN/m for $\pi_i \leq 15$ mN/m (expanded/condensed coexistence). For a condensed film, a MIP of 36 mN/m was calculated.

However, the MIP of LL-20 is lowered by the incorporation of SM (MIP = 25 mN/m compared to 32 mN/m for DPPC) and increased by the presence of DOPS (36 mN/m). The MIPs of LL-20 are independent from the phase and reflect more the influence of charges on the peptide.

5.2.2 SM Addition to Fluid DOPC Monolayers Has no Effect on the Peptide Interaction

To compare the results with experiments with fluid lipids, DOPC monolayers were used. The incorporation of neither SM nor DOPS changes the shape of the isotherm (Figure 37 A)), confirming a fluid phase even after SM incorporation. This was proved by IRRAS. Highly ordered chains (all trans conformation) result in a CH_2 band at low wavenumbers while fluid chains (gauche conformation) vibrate at higher wavenumbers. The coexistence of fluid and condensed phases (analogous to L_o and the L_d phases in bilayers) leads to an overlap of the vibrational energies and can clearly be distinguished. The CH_2 band of the DOPC/SM is shown in Figure 37 B). It has a constant maximum at 2854.0 and 2923.5 cm^{-1}, independent of the surface pressure, indicating an overall fluid film.

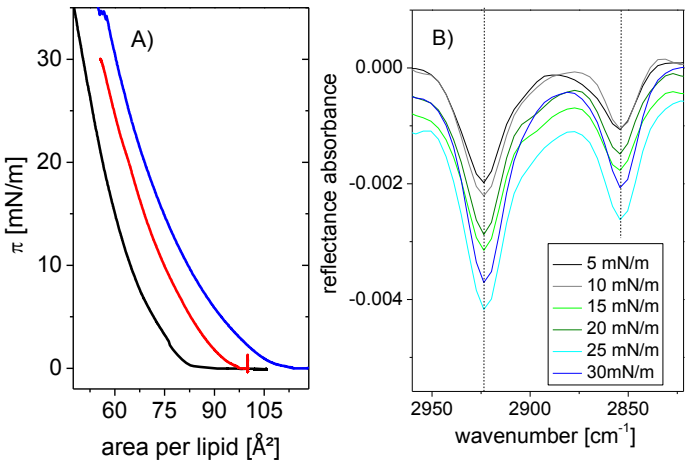

Figure 36: A) Isotherms of DOPC (—), DOPC/SM (50:50) (—), and DOPC/SM/DOPS (45:45:10) (—) B) CH_2 bands of DOPC/SM for different surface pressures π. (5 mM HEPES, 100 mM NaCl, pH 7.4, 20°C)

5.2.2.1 IRRAS

The adsorption of the peptides to DOPC, DOPC/SM and DOPC/SM/DOPS led to comparable results like for the DPPC mixtures. The equilibrium surface pressure is unchanged by the addition of SM or DOPS (for details see appendix). But compression of the LL-32-mixed film does not lead to a complete squeeze-out of the peptide. LL-20 is already squeezed out at 25 mN/m, in all mixtures. The IR spectra can be found in the appendix. Because of the fact that DOPC cannot undergo a phase transition to the condensed phase, the CH_2 band position gives no further information about the peptide-lipid interaction, and the spectra are therefore not shown.

5.2.2.2 Injection Under Pre-compressed Monolayers

The MIPs are the same for all DOPC-mixtures (Figure 38). Within the statistical error (±3 mN/m), the MIP of ~42 mN/m indicates a strong interaction of LL-32 with the lipids, but independent from the incorporation of SM and DOPS. Moreover, the MIP values are below the values of the heterogeneous films. This supports the assumption that the coexistence of fluid and condensed domains dominates the interaction of LL-32 with the monolayers, rather than the fluidity or the presence of charges. The MIP of LL-20 is ~30 mN/m for all mixtures, indicating only a low affinity of the peptide for the lipid films.

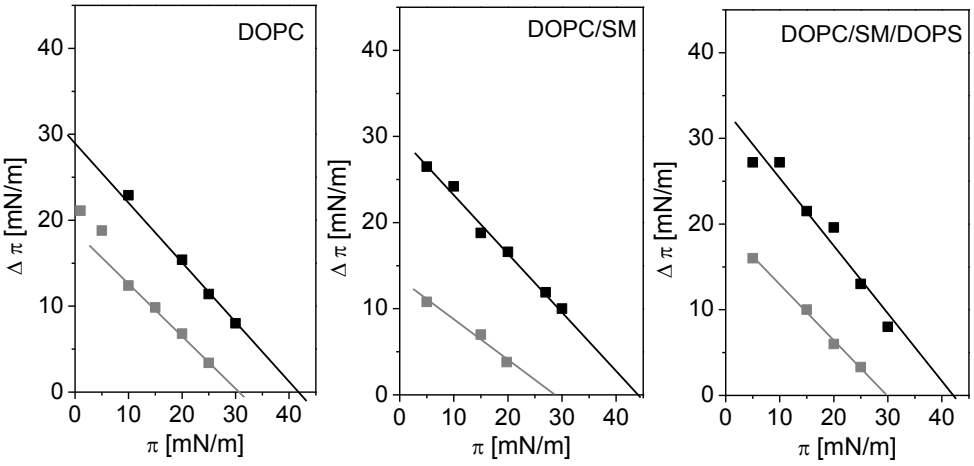

Figure 37: Maximum Insertion Pressure experiments of LL-32 (■) and LL-20 (■) into DOPC, DOPC/SM (50:50) and DOPC/SM/DOPS (45:45:10) monolayers and linear fit to estimate the MIP. (5 mM HEPES, 100 mM NaCl, pH 7.4, 20°C, 0.2 µM peptide in solution).

5.3 Discussion

In this chapter, the interaction of mixed model membranes with LL-32 and LL-20 was investigated. To mimic human erythrocytes, monolayers were prepared from mixtures of DPPC or DOPC with SM. All of them carry the same head group, but vary in chain length and saturation and thus the phase transition temperatures. Additionally, SM contains a sphingosin backbone. The main constituent of brainSM, C18:0 SM is well miscible with DPPC, in both the gel and the liquid-crystalline phase [196]. The DPPC/SM lipid mixture was extended by adding the negatively charged DOPS to mimic cancer cells. Before investigating the interaction with the peptides, the monolayers were characterized in terms of their structure.

5.3.1 Structure of the Lipid Films

DPPC and SM

From the position of the Bragg peaks and Bragg rods measured with surfaces sensitive GIXD, it can be concluded that SM is tilted by 18.1°.This is different from GIXD measurements of other work groups. Vaknin and Kelley [193] reported a tilt of ~4.2° of brainSM on water, albeit they receive unnaturally high values for the chain cross-section (>21 $Å^2$). Broniatowksi *et al.* [197] indexed two diffraction peaks and calculated a tilt angle of 14.2° on water, but identified only one peak in the presence of mercury salts, which corresponds to untilted molecules. This is not understandable, since the Bragg peak profile indicates clearly the presence of more than one peak and the calculated correlation length L_z is with 12.8 and 10.2 Å too small compared to values they obtained from XR (~ 15 Å for the tail region). Also, the electron density profile allows the interpretation of a tilted molecule with a tilted head group instead of zigzag order of untilted molecules. Anyway, the sphingosine has a defined chain length corresponding to 18 carbon atoms. The second chain has a varying length and can be shorter, equal or longer. The resulting electron density profile would consist of two different parts. Unfortunately, both groups did not present the diffraction pattern in their work to discuss this in detail. Maulik and Shipley [198] assumed a tilted gel phase $L_{\beta'}$ based on their X-ray diffraction data in bilayer experiments of 24:0 SM, but they did not calculate the exact tilt angle.

It was shown that at 20°C, DPPC and SM exhibit a phase transition from the expanded to the tilted condensed phase upon compression, but the surface pressure of the transition is higher for SM and smeared over a wide pressure range. Unsaturated chains act as contaminants which are squeezed out from the condensed part of the film upon compression [199] and lead to a resistance of the monolayer against compression due to the nonzero rigidity in the coexistence region [195]. Moreover, the changed compressibility leads to lateral molecular density fluctuations of the

cooperative units [200]. This leads to a deviation of the isotherm from a horizontal line. Since SM is a mixture with varying chain length (50% 18:0, 21% 24:1, 7% 22:0, 5% 20:0, 5% 24:0, 2% 16:0 fatty acid distribution), the molecules with unsaturated chains are squeezed out from the condensed domains upon compression, leading to a coexistence of condensed and fluid phases. The condensed domains with a perfect crystallinity have only small size. GIXD analysis resulted in correlation lengths of 87 Å and 57 Å of SM while DPPC shows a perfect crystallinity over a wide range of ~670 Å and ~100 Å.

As shown in chapter 4, DPPC is tilted by 31.8° at 30 mN/m. The addition of SM to DPPC monolayers results in a shift in the phase transition from the expanded to the condensed phase to a higher surface pressure, which is additionally smeared over a broad pressure range. This was confirmed by the CH_2 band position in IRRAS experiments and is related to the complexity of the mixture. The transition range shows a linear dependence on the mole fraction of SM. DPPC and 18:0 SM or SM-mixtures containing mainly 16:0 SM are well miscible in both the gel and the liquid-crystalline phase [196; 201]. Analysis of the diffraction pattern of the condensed DPPC/SM mixtures results in a tilt angle of 23.2° at 30 mN/m which is smaller compared to DPPC (31.8°), but larger compared to SM (18.1°). SM influences the ordering of the polar head groups of DPPC [201], leading to a changed packing. The correlation lengths decrease to 166 Å, 34 Å and 73 Å. The diffraction pattern differs clearly from that of pure DPPC and SM, meaning that both types of lipids influence each other. The reduced correlation length shows that the crystallinity is reduced and that the presence of the SM mixture leads to more defects.

DOPC and SM

From the shape of the isotherm and the CH_2 band position it was concluded that DOPC/SM mixed monolayers are like DOPC monolayers in a fluid phase. This is in agreement with the confocal microscopy observations on GUVs [203] and MD simulations [204] that DOPC and 18:0 SM do not phase separate. On the other hand, Langmuir-Blodgett transfer of DOPC/brainSM monolayers on water resulted in microdomains in AFM pictures [205]. Differential Scanning Calorimetry (DSC) and Förster Resonance Energy Transfer (FRET) measurements revealed that brainSM and DOPC exhibit fluid-fluid coexistence [206]. Mixtures with DOPC and 16:0 SM or eggSM (which contributes to 86% 16:0 SM) exhibit a clear phase separation into L_d and S_o phase with [140-142], but the results cannot be directly compared with our mixture, since brain SM contains mainly 18:0 SM.

Incorporation of DOPS to the Mixed Films

The addition of 10 mol % DOPS has no influence on the isotherm or the CH_2 band position in IRRAS. But GIXD experiments showed that DOPS influences the packing in the condensed film of DPPC/SM. The diffraction pattern consists of two strongly overlapping peaks with low intensity and shows similarities to raft-like domains with cholesterol [194]. The obtained tilt angles are only slightly changed to 22.2° for all π. The correlation length L_z is increased from 16.4 (DPPC/SM) to 20.1 Å. A reduced intensity means a decreased contribution of scattering molecules. The remaining SM molecules which contribute to the diffracted signal are the longer ones which are less good miscible within the film. This happens if more SM molecules with shorter chain length are mixed within the fluid part of the film. Therefore, L_z is increased while the overall signal is reduced.

5.3.2 Influence of SM and DOPS on the Peptide Interaction

The MIP experiments revealed the dependence of the lipid phase state on the peptide incorporation. LL-32 has a MIP of 52 mN/m into DPPC/SM and DPPC/SM/DOPS monolayers for heterogeneous films containing both, expanded and condensed phases. Comparison to fluid lipid films (DOPC, DOPC/SM and DOPC/SM/DOPS) show that the peptide has indeed a higher affinity for lipid monolayers in a fluid phase, but the MIP of ~ 42 mN/m into fluid films is still below the MIP for the heterogeneous films containing DPPC (MIP ~ 52 mN/m). Also, the incorporation of DOPS has no influence on the interaction of the peptide, even when the ordering of the molecules was reduced.

The phase transition is characterized by the coexistence of two phases. In DPPC monolayers, already a small increase in the surface pressure by the adsorption of the peptide leads to a transition to a completely condensed film. The incorporation of SM blurs the phase transition over a wide pressure range. The coexistence of expanded and condensed phases is retained. If the peptide is injected under the pre-compressed DPPC monolayer (experiments were done above π_{pt}, for π_i>10 mN/m), the peptide adsorbs to a condensed film. If the peptide is injected under a pre-compressed DPPC/SM(/DOPS) monolayer, for π_i<20 mN/m, the peptide adsorbs to the film containing both, fluid and condensed domains..

In contrast to DPPC, where the adsorption of the peptides leads to a condensation of the lipid film, the mixed films are more fluid in the presence of the peptide, as concluded from the higher CH_2 band position in the IRRAS experiments. LL-32 is not squeezed out by the compression of the SM-mixed film to 35 mN/m, though DOPC, DPPC and SM have the same head group and the interaction with the head group was thought to be accountable for the membrane-lytic effect of

the peptide (chapter 4). It could be shown, that the membrane activity of LL-32 is increased in the presence of a miscibility gap of the lipids.

LL-20 is apparently different. The equilibrium surface pressure is too low to induce the phase transition of the lipid film, which is necessary to create a coexistence of fluid and condensed sections. Already a compression of the peptide/lipid film to only 25 mN/m results in a squeezing-out of the peptide, as followed by the IR data. The CH_2 band position is comparable to that of a bare lipid film and also the amide bands vanish. So the interaction of LL-20 with DPPC is not enhanced by the addition of SM. The MIP is rather reduced by SM incorporation (from 32 to 25 mN/m) . The incorporation of DOPS has also no effect.

6 General Discussion/Conclusion

Two fragments of the human AMP LL-37 with different antibacterial activities were investigated in this work. LL-32 lacks the unstructured part of LL-37, which makes the peptide more active against bacteria, but also more active against human cells [85; 87; 143]. LL-20 exhibits almost no activity against both types of cells [143-145], presumably because it lacks the identified antimicrobial core [88].

In chapter 3 of this work, the peptides were characterized by their physical-chemical properties. Their surface activity was investigated and the structure at the air/water interface was compared with the structure of the peptides in solution. In chapter 4, the interaction of the peptides with membrane models was investigated. There the peptide binding to various lipid monolayers was compared. Negatively charged lipids (POPG, DPPG) were used to model the interaction with bacteria membranes and zwitterionic lipids (DOPC, DPPC, POPC) were used to model the interaction with mammalian cells. In chapter 5, the mammalian membrane model was extended by the addition of SM to DOPC and DPPC in order to mimic better the membrane of human erythrocytes. The influence of SM on the lipids was investigated and its effect on the peptide interaction with the membrane was discussed. Additionally, DOPS was incorporated to increase the surface charge to mimic cancer cell membranes, and the influence of DOPS addition on the peptide interaction with the membrane was investigated.

6.1 Peptides at the Air/water Interface

Two fragments of the antimicrobial peptide LL-37 have been characterized in bulk and adsorbed at the air/water interface by CD and IRRAS experiments, respectively. XR gave additional information and allowed to explain the differences observed between the two peptides. The results are graphically represented in Figure 39.

LL-32 and LL-20 obtain an unstructured conformation in solution. Film balance measurements showed that both peptides differ drastically in their surface activity. The equilibrium surface pressure $\pi_{eq} \sim 24$ mN/m for LL-32 and ~ 6 mN/m for LL-20. Adsorbed to the air-water interface, LL-32 transforms into an α-helical structure with a diameter of 14 Å with the molecular axis parallel to the interface. This was confirmed by IRRAS and XR experiments.

The conformation of LL-20 deviates from that of a pure α-helix, since the dichroic ratio of the amide I band is reduced and the electron density profiles consist of two contributions. It was concluded that a part of the LL-20 peptides does not exist as an α-helix flat at the interface, but remains partially unstructured after adsorption. The main reason for this clear difference between LL-32 and LL-20 is the reduced surface activity of LL-20. Therefore, the critical surface concen-

Figure 38: Schematic picture of the peptides adsorbed to the air/water interface in side view. LL-32 (black) adopts an α-helix with the axis lying flat at the interface and a random in-plane orientation. LL-20 (grey) forms a similar α-helix, but with an unstructured contribution of the peptide located close to the interface.

tration for the transition to a complete helix cannot be reached in the LL-20 film. After compression of the LL-20 film, the unstructured molecules are mainly squeezed out into the bulk solution, leading to IR-spectra and dichroic ratios comparable to those of LL-32. However, some unstructured LL-20 molecules stay at the interface, giving rise to an electron density profile described by two contributions. In other words LL-20 does not reach the concentration threshold needed for a complete transformation to a helical structure at the air/water interface. Therefore the adsorption layer consists of two parts: Unstructured peptides and helical peptides. In contrast, LL-32 forms a perfect helix at the hydrophilic/hydrophobic interface, what can be related to the higher antimicrobial activity.

6.2 Interaction of the Peptides with Vesicles

LL-32 and LL-20 are unstructured in the bulk solution, as concluded from the CD spectra. The titration of zwitterionic POPC vesicles to the peptide solution had no influence on the peptide conformation. Moreover, it could be shown that the unstructured peptides in the presence of POPC vesicles correspond to unbound peptides in water. In contrast the titration of POPG vesicles to the peptide solution led to a change in the secondary structure for both peptides from an unstructured to an α-helical conformation. As shown in earlier studies, the binding of an antimicrobial peptide to a membrane mimetic interface can be connected to a change in the secondary structure [31; 32; 128], which is in good agreement with the finding that LL-32 and LL-20 bind to a hydrophobic/hydrophilic interface by forming an α-helix. However, the peptides differ in their structure when adsorbed to the air/water interface. Consequently, the question appears why both peptides entirely fold into a helix in the presence of POPG? It was shown by molecular dynamics simulations that the adsorption of peptides to the air/water interface can occur via a series of intermediate states [207] which are metastable amphipathic structures with buried hydrophobic residues [1]. In the case of LL-20, the intermediate state at the air/water interface is a partly unstructured conformation, as found in bulk. The presence of the head group charges of POPG could help the peptide to fold into an α-helix.

6.3 Interaction of the Peptides with Lipid Monolayers

From the Maximum Insertion Pressure (MIP) experiments with DOPC, DPPC, DPPG, and POPG it was concluded, that a penetration into both, human and bacteria cell membranes, is feasible only for LL-32 and not for LL-20. This is consistent with biological experiments [85; 87; 143-145]. But the way of interaction must be specific for the respective cell type, even though *in vivo* experiments with LL-37 show no cell selectivity [73]. From the surface pressure dependent IR measurements it can be concluded that the interaction of LL-32 and LL-20 with DPPG monolayers proceeds via two steps:

1. Adsorption of the peptides to the air/water interface between the lipid molecules which leads to a condensation of the lipids by compression

2. Adsorption of the peptides to condensed lipid domains, leading to fluidization of the lipid monolayer.

In step one, peptide and lipids form two phases while in step two, peptides and lipids mix. This is in agreement with the idea that LL-37 binds as oligomers to zwitterionic membranes [111], but as monomers to negatively charged membranes [73].

From the electron density profiles could be concluded that LL-32 binds as an helix between the lipids, preferentially interacting with the air/water interface, but it also binds as a helix underneath the condensed domains of DPPG. The second layer of LL-20 is (partly) unstructured, when LL-20 is adsorbed at the air/ water interface. This explains the stronger redshift of the amide I band of LL-32 compared to LL-20.

The two peptides bind differently to model membranes in different phases. LL-32 binds to POPG and DPPG at surface pressures < 40 and < 45 mN/m, respectively. While LL-32 completely incorporates into the POPG monolayer, it forms an additional layer under the condensed DPPG.

The MIP of LL-20 into a POPG monolayer is the same as for LL-32, but the injection of the peptide under condensed DPPG led to a constant increase in the surface pressure $\Delta\pi$, independent from the initial surface pressure π_i. I interpreted this as a kind of aggregation of the peptide, based on electrostatic attraction. This is in agreement with the electron density profile of the peptide/lipid film, which predicted an unstructured peptide bound under the head groups – in contrast to LL-32 which is bound in a helical conformation. The bound LL-20 shields the charges of the DPPG head group, leading to a better packing of lipid chains. This resulted in decreased tilt angles of the chains (22.9° instead of 26.9° for DPPG). This could be a transient state in the

peptide-lipid interaction and needs further investigation. It was shown that the peptides lead to a fluidization of DPPG films in an expanded phase, which precedes with a condensation of the film.

The intercalation of the peptides into the DPPG monolayer can be deeper for LL-32 than for LL-20, since we observe a stronger redshift in the amide I band in the adsorption process, which indicates less water contact of the peptide bonds by a deeper intercalation into the lipid chain region or more oriented H-bonds. As shown for other CAP18-derived peptides, the possibility of a deep penetration is sufficient for the antimicrobial activity of CAP-derived peptides [120; 208]. It was shown in bilayer experiments with alamethicin, that the fluidization effect is connected to a membrane thinning [175]. The deep insertion and accumulation of peptides into one half of the bilayer can lead to a mass imbalance and therefore a curvature strain and membrane thinning [55]. The strong fluidization effect of AMPs in monolayer experiments was also observed for some other helical AMPs: the pore forming peptides Protegrin [179; 209], Dicynthaurin [28], for LL-37 [136] and concentration-dependent for SMAP-29 [210], which belongs to the cathelicidin family like LL-37. For melittin, the helical content increases with the penetration depth of the peptide into DMPC/DMPA vesicles [211].

MIP experiments showed that LL-32 does not fluidize completely condensed DPPG films. How is this possible, since the adsorption of the peptide to uncompressed monolayers leads to a fluidization of the film? The adsorption of the peptides to the initially expanded lipid film leads to a condensation of the lipid molecules. This means that there is a transient coexistence between expanded and condensed phases within the monolayer. In chapter 5 it was shown that the MIP depends strongly on the phase state of DPPC/SM and DPPC/SM/DOPS films and that the coexistence of fluid and condensed phases increases the MIP and thus the interaction with the peptide. This will be now discussed in detail.

6.4 Interaction of the Peptides with Mixed Lipid Monolayers Containing SM and DOPS

Besides PCs, SM is a main component in mammalian cells. Together, PCs and SMs they make more than 80% of the total lipid amount in the outer leaflet of human red blood cells [14]. SM can form inter- and intramolecular hydrogen bonds [16; 17] and that has influence on the head group order of DPPC [201].

It was shown that in a condensed phase at 30 mN/m, the acyl chains of DPPC are tilted by 31.8° and the alcyl chains of SM are tilted by 18.1°. The mixing of the two lipids results in a tilt of 23.2°, showing that SM influences the head group packing of PCs [201]. The phase transition

of DPPC is smeared by SM incorporation, but shows a linear dependence on the mole fraction of SM in the mixture indicating that number of molecules, which cannot undergo a phase transition to the condensed phase, act as contaminants. This coexistence of two phases over a wide pressure range increased the interaction of the monolayer with LL-32. In MIP experiments, where the peptide is injected under a pre-compressed monolayer with a defined surface pressure and phase, it could be shown that LL-32 binds much stronger to heterogeneous lipid monolayers than to a fluid or condensed lipid film. The MIP was larger for the coexistence of the expanded and the condensed phase. The interaction of LL-20 was unaffected by the heterogeneity of the film. Moreover, the presence of SM reduced the MIP of LL-20, which can be related to a weakened interaction of the peptide with the lipid film. A schematic illustration is shown in Figure 40.

Figure 40: Schematic Illustration of LL-32 bound as an αhelix to the interface between a fluid and a condensed phase.

DOPC/SM mixtures were prepared for comparison to see the influence of an overall fluid phase on the peptide-membrane interaction. As concluded from the isotherm and the methylene vibration bands, DOPC/SM monolayers are in a fluid phase like DOPC, but can exhibit fluid-fluid coexistence [206]. Though it was shown that the peptides can better intercalate into fluid compared to condensed lipid films (chapter 4), the MIP of LL-32 into DOPC/SM films was lower than for the DPPC/SM mixture in the coexistence region.

Incorporation of SM into the lipid monolayer reduces the MIP of LL-20 from 32 mN/m into DPPC to 25 mN/m. Due to the fact that the used mixture corresponds to more than 80% of the total lipid amount in the outer leaflet of a human red blood cell [14], an interaction with that cell type is unlikely for LL-20, which is in agreement with the biological experiments [143; 145].

It was shown in chapter 4 that LL-32 leads to a fluidization of DPPG monolayers as if it adsorbs to uncompressed films. The interaction occurs via the intermediate of a condensed lipid film, as deduced from the CH_2 band position in the IRRAS experiments. I suggest that the interaction of the peptide with DPPG is also determined by the coexistence of LE and LC phases during the adsorption process. A graphical summary is presented in Figure 41.

But can the interaction of the peptide with the membrane be improved by the existence of small domains? Membrane heterogeneity was shown to be crucial for the selectivity of some model AMPs [212]. The peptide indolicidin, appears to initiate a thinning of the gel-phase domains

independent of the presence of an anionic lipid at high peptide concentrations while it forms an amorphous peptide layer on the fluid domains containing anionic lipids at low peptide concentrations [213]. Recently, it was shown that the cyclic antimicrobial peptide surfactin binds preferentially to the fluid phase at high peptide concentrations while at low peptide concentrations, the peptides bind to the interface of domains and destroys them [214]. This I would also suggest for LL-32, but a direct proof still needs to be provided. If the peptides interact with the lipid phase boundaries, they change the line tension of the interface, inducing a membrane-disruption in a detergent-like way [6].

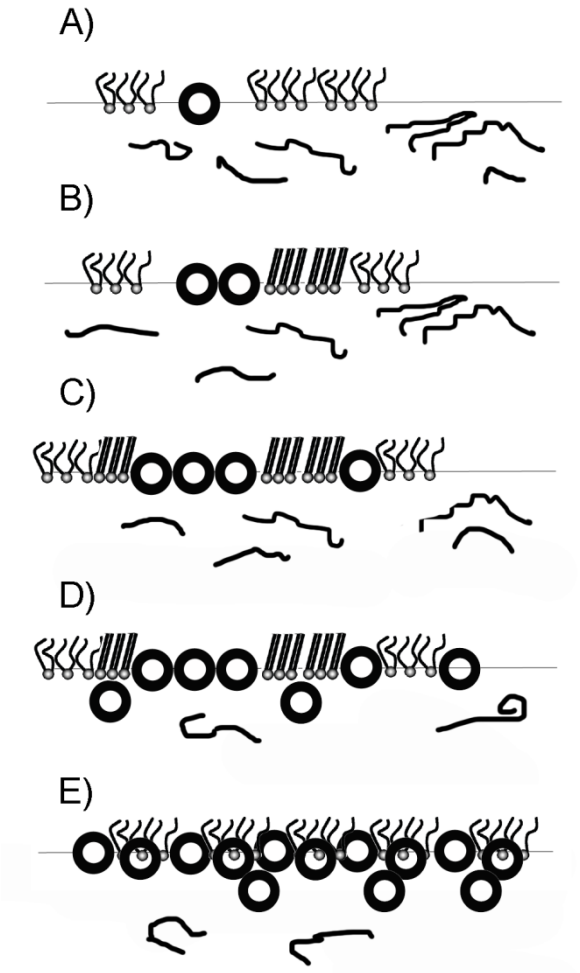

Figure 41: Schematic presentation of the adsorption process of LL-32 to a DPPG monolayer at the air/water interface. A) The lipid solution is spread on a peptide-containing subphase. The peptides are unstructured in solution, but some peptides are adsorbed to the air/water interface. The lipids are in an expanded state. B) The peptides are attracted to the air/water interface and the charged head groups of the lipids. The increasing amount of peptides at the interface leads to a condensation of the lipid film. C) and D) The peptides bind preferentially to transient interfaces of coexisting phases, reducing the line tension. Some peptides bind additionally underneath the headgroups. E) In equilibrium, the surface is maximal covered with peptides. Condensed domains are dissolved which results in a fluidized lipid film. Some more peptides could be bound underneath the monolayer or a part of the peptide could hang out of the interface.

DOPS was incorporated into the membrane model to mimic cancer cell membranes. A PS content of 10% corresponds to the value in the outer leaflet of leukemia cells [23].Incorporation of DOPS into the DPPC/SM mixture changed slightly the surface activity of the peptides (the equilibrium surface pressure was slightly increased), but had no influence on the MIP and its phase dependence. Moreover, incorporation of DOPS had no influence on the interaction of the peptide with DOPC/SM mixed films. Why is the interaction of LL-32 with the SM-mixed films not increased by incorporating the negatively charged DOPS? LL-32 is strongly active against some cancer types [145], and cancer cells have an increased level of negatively charged lipids in the outer leaflet of their membrane [20; 21]. Compared to healthy cells, in cancer cells the elasticity of the whole cell is changed [19] and some cancer cell types contain an increased amount of cholesterol-rich rafts [22], which changes the fluidity. This could be the key effect in the anticancer activity of LL-32. That means that the surface charge acts more as a helper to attract the peptide, as already proposed [119; 120].

6.5 Similiarities of LL-32 and LL-37 to Melittin

Interesting are some similarities between LL-32 and melittin. First of all melittin is non-cell selective [72; 73] and active against cancer cells [124; 125; 212], like LL-37 and LL-32. The formation of pores is part of the interaction of melittin with zwitterionic lipids while the peptide is destroying negatively charged membranes in a detergent-like way [75; 213].

Flach *et al.* [169] obtained results on melittin with IRRAS measurements which can be compared to the results from this study: a condensation of the zwitterionic lipid monolayer (DPPC) and a fluidisation of the negatively charged lipid monolayer (DPPS). Besides that, bulk studies by Sevcisk *et al.* [214] with LL-37 and melittin showed comparable results. Based on SAXS, ESR and DSC measurements, they could draw a schematic phase diagram depending on the peptide concentration and the hydrocarbon chain length of the lipids, including lamellar non-interdigitated, interdigitated phases and micellar disks, which is valid for both peptides. They concluded a general mechanism for α-helical AMPs, but I would rather conclude that this shows more the similarity of the two peptides.

Moreover, melittin showed higher leakage efficiency upon increasing the SM content in POPC vesicles, which could be attributed to the coexistence of gel-phase SM-rich domains [215], which is in accordance with the results with LL-32 (chapter 5). Also, both peptides influence phospholipase A_2 acitivity [216-218]. The enzyme actitivity depends also on the coexistence of two phases [219] and the enzyme binds probably to the interfaces of domains [220]. Further investigations on melittin, LL-37 and their interplay with phospholipases could reveal valuable

details about their interplay. Moreover, a deeper investigation of the binding properties of melittin and LL-37 to lipid mixtures exhibiting an immiscibility gap is crucial.

Recently, it was shown that surfactin, a strong detergent and antibiotic, leads to lipid de-mixing [221] and binds to the interface between L_o and L_d phases [222]. The pore-forming equinatoxin II binds preferentially to domain interfaces and forms pores in giant unilamellar vesicles containing sphingomyelin only when liquid-ordered and liquid-disordered phases coexisted [223].

Future experiments with incorporation of cholesterol to the PC/SM mixtures would yet be interesting, since cholesterol influences the membrane structure by dissolving microdomains [205] or leading to phase separation by binding to the interfaces of microdomains [204]. Consequently, this reduces the penetration depth of melittin [224] and has a concentration-dependent effect on the membrane association of LL-37 [225]. Monolayer experiments, AFM and fluorescence-microscopy measurements with mixed membranes and fragments of LL-37 could be helpful to answer open questions about the binding of the peptides to the L_o-L_d interface and introduce new ones. But beside the effect of highly ordered rafts on the peptide interaction, the influence of immiscible components within the membrane should be part of further research in the interaction between AMPs and membranes.

7 References

[1] L.R. Pratt, A. Pohorille. Hydrophobic Effects and Modeling of Biophysical Aqueous Solution Interfaces. *Chemical Reviews* 102 (2002), 2671-2692.

[2] P. Wydro. The Magnitude of Condensation Induced by Cholesterol on the Mixtures of Sphingomyelin with Phosphatidylcholines-Study on Ternary and Quaternary Systems. *Colloids and surfaces. B, Biointerfaces* 82 (2011), 594-601.

[3] W. Dowhan. Molecular Basis for Membrane Phospholipid Diversity: Why Are There So Many Lipids? *Annual Review of Biochemistry* 66 (1997), 199-232.

[4] G.W. Feigenson. Phase Boundaries and Biological Membranes. *Annual Review of Biophysics and Biomolecular Structure* 36 (2007), 63-77.

[5] S.J. Singer, G.L. Nicolson. The Fluid Mosaic Model of the Structure of Cell Membranes. *Science* 175 (1972), 720-731.

[6] P.F.F. Almeida, A. Pokorny, A. Hinderliter. Thermodynamics of Membrane Domains. *Biochimica et Biophysica Acta-Biomembranes* 1720 (2005), 1-13.

[7] K. Simons, D. Toomre. Lipid Rafts and Signal Transduction. *Nature Reviews Molecular Cell Biology* 1 (2000), 31-39.

[8] D. Lingwood, K. Simons. Lipid Rafts as a Membrane-Organizing Principle. *Science* 327 (2010), 46-50.

[9] K. Simons, E. Ikonen. How Cells Handle Cholesterol. *Science* 290 (2000), 1721-1726.

[10] K. Simons, E. Ikonen. Functional Rafts in Cell Membranes. *Nature* 387 (1997), 569-572.

[11] Z. Korade, A.K. Kenworthy. Lipid Rafts, Cholesterol, and the Brain. *Neuropharmacology* 55 (2008), 1265-1273.

[12] C. Luo, K. Wang, Q. Liu de, Y. Li, Q.S. Zhao. The Functional Roles of Lipid Rafts in T Cell Activation, Immune Diseases and Hiv Infection and Prevention. *Cellular & Molecular Immunology* 5 (2008), 1-7.

[13] S.H. Untracht, G.G. Shipley. Molecular-Interactions between Lecithin and Sphingomyelin - Temperature-Dependent and Composition-Dependent Phase Separation. *Journal of Biological Chemistry* 252 (1977), 4449-4457.

[14] A.J. Verkleij, R.F.A. Zwaal, Roelofse.B, Comfuriu.P, Kastelij.D, Vandeene.Ll. Asymmetric Distribution of Phospholipids in Human Red-Cell Membrane - Combined Study Using Phospholipases and Freeze-Etch Electron-Microscopy. *Biochimica et Biophysica Acta* 323 (1973), 178-193.

[15] M. Koval, R.E. Pagano. Intracellular Transport and Metabolism of Sphingomyelin. *Biochimica et Biophysica Acta* 1082 (1991), 113-125.

[16] B. Ramstedt, J.P. Slotte. Membrane Properties of Sphingomyelins. *FEBS Letters* 531 (2002), 33-37.

[17] T. Rog, M. Pasenkiewicz-Gierula. Cholesterol-Sphingomyelin Interactions: A Molecular Dynamics Simulation Study. *Biophysical Journal* 91 (2006), 3756-3767.

[18] T.P.W. McMullen, R.N.A.H. Lewis, R.N. McElhaney. Cholesterol–Phospholipid Interactions, the Liquid-Ordered Phase and Lipid Rafts in Model and Biological Membranes. *Current Opinion in Colloid & Interface Science* 8 (2004), 459-468.

[19] S. Suresh. Biomechanics and Biophysics of Cancer Cells. *Acta Biomaterialia* 3 (2007), 413-438.

[20] T. Utsugi, A.J. Schroit, J. Connor, C.D. Bucana, I.J. Fidler. Elevated Expression of Phosphatidylserine in the Outer Membrane Leaflet of Human Tumor Cells and Recognition by Activated Human Blood Monocytes. *Cancer Research* 51 (1991), 3062-3066.

[21] S. Ran, A. Downes, P.E. Thorpe. Increased Exposure of Anionic Phospholipids on the Surface of Tumor Blood Vessels. *Cancer Research* 62 (2002), 6132-6140.

[22] S. Riedl, D. Zweytick, K. Lohner. Membrane-Active Host Defense Peptides - Challenges and Perspectives for the Development of Novel Anticancer Drugs. *Chemistry and Physics of Lipids* 164 (2011), 766-781.

[23] H. Schroder-Borm, R. Bakalova, J. Andra. The Nk-Lysin Derived Peptide Nk-2 Preferentially Kills Cancer Cells with Increased Surface Levels of Negatively Charged Phosphatidylserine. *FEBS Letters* 579 (2005), 6128-6134.

[24] K. Lohner, E.J. Prenner. Differential Scanning Calorimetry and X-Ray Diffraction Studies of the Specificity of the Interaction of Antimicrobial Peptides with Membrane-Mimetic Systems. *Biochimica et Biophysica Acta (BBA) - Biomembranes* 1462 (1999), 141-156.

[25] W. Zhao, T. Rog, A.A. Gurtovenko, I. Vattulainen, M. Karttunen. Atomic-Scale Structure and Electrostatics of Anionic Palmitoyloleoylphosphatidylglycerol Lipid Bilayers with Na+ Counterions. *Biophysical Journal* 92 (2007), 1114-1124.

[26] R.M. Epand, R.F. Epand. Lipid Domains in Bacterial Membranes and the Action of Antimicrobial Agents. *Biochimica et Biophysica Acta (BBA) - Biomembranes* 1788 (2009), 289-294.

[27] H. Brockman. Lipid Monolayers: Why Use Half a Membrane to Characterize Protein-Membrane Interactions? *Current Opinion in Structural Biology* 9 (1999), 438-443.

[28] M. Majerowicz, A.J. Waring, S.Y. Wen, F. Bringezu. Interaction of the Antimicrobial Peptide Dicynthaurin with Membrane Phospholipids at the Air-Liquid Interface. *Journal of Physical Chemistry B* 111 (2007), 3813-3821.

[29] V.M. Kaganer, H. Mohwald, P. Dutta. Structure and Phase Transitions in Langmuir Monolayers. *Reviews of Modern Physics* 71 (1999), 779-819.

[30] R. Maget-Dana. The Monolayer Technique: A Potent Tool for Studying the Interfacial Properties of Antimicrobial and Membrane-Lytic Peptides and Their Interactions with Lipid Membranes. *Biochimica et Biophysica Acta-Biomembranes* 1462 (1999), 109-140.

[31] C. Olak, A. Muenter, J. Andrae, G. Brezesinski. Interfacial Properties and Structural Analysis of the Antimicrobial Peptide Nk-2. *Journal of Peptide Science* 14 (2008), 510-517.

[32] O.G. Travkova, J. Andra, H. Mohwald, G. Brezesinski. Conformational Properties of Arenicins: From the Bulk to the Air-Water Interface. *ChemPhysChem* 11 (2010), 3262-3268.

[33] E. Maltseva, A. Kerth, A. Blume, H. Mohwald, G. Brezesinski. Adsorption of Amyloid Beta (1-40) Peptide at Phospholipid Monolayers. *ChemBioChem* 6 (2005), 1817-1824.

[34] F. Bringezu, M. Majerowicz, E. Maltseva, S.Y. Wen, G. Brezesinski, A.J. Waring. Penetration of the Antimicrobial Peptide Dicynthaurin into Phospholipid Monolayers at the Liquid-Air Interface. *ChemBioChem* 8 (2007), 1038-1047.

[35] M. Hoernke, B. Koksch, G. Brezesinski. Influence of the Hydrophobic Interface and Transition Metal Ions on the Conformation of Amyloidogenic Model Peptides. *Biophysical Chemistry* 150 (2010), 64-72.

[36] S.H. White, W.C. Wimley. Hydrophobic Interactions of Peptides with Membrane Interfaces. *Biochimica et Biophysica Acta-Reviews on Biomembranes* 1376 (1998), 339-352.

[37] D. Marsh. Lateral Pressure in Membranes. *Biochimica et Biophysica Acta-Reviews on Biomembranes* 1286 (1996), 183-223.

[38] A. Blume. A Comparative Study of the Phase Transitions of Phospholipid Bilayers and Monolayers. *Biochimica et Biophysica Acta* 557 (1979), 32-44.

[39] Y.H. Chan, S.G. Boxer. Model Membrane Systems and Their Applications. *Current Opinion in Chemical Biology* 11 (2007), 581-587.

[40] M. Eeman, M. Deleu. From Biological Membranes to Biomimetic Model Membranes. *Biotechnologie Agronomie Societe Et Environnement* 14 (2010), 719-736.

[41] A.R. Honerkamp-Smith, S.L. Veatch, S.L. Keller. An Introduction to Critical Points for Biophysicists; Observations of Compositional Heterogeneity in Lipid Membranes. *Biochimica et Biophysica Acta-Biomembranes* 1788 (2009), 53-63.

[42] S.L. Veatch, O. Soubias, S.L. Keller, K. Gawrisch. Critical Fluctuations in Domain-Forming Lipid Mixtures. *Proceedings of the National Academy of Sciences of the United States of America* 104 (2007), 17650-17655.

[43] C. Esposito, A. Tian, S. Melamed, C. Johnson, S.-Y. Tee, T. Baumgart. Flicker Spectroscopy of Thermal Lipid Bilayer Domain Boundary Fluctuations. *Biophysical Journal* 93 (2007), 3169-3181.

[44] L.S. Tavares, O. Santos Mde, L.F. Viccini, J.S. Moreira, R.N. Miller, O.L. Franco. Biotechnological Potential of Antimicrobial Peptides from Flowers. *Peptides* 29 (2008), 1842-1851.

[45] A. Giuliani, G. Pirri, A. Bozzi, A. Di Giulio, M. Aschi, A.C. Rinaldi. Antimicrobial Peptides: Natural Templates for Synthetic Membrane-Active Compounds. *Cellular and molecular life sciences : CMLS* 65 (2008), 2450-2460.

[46] M. Zasloff. Antimicrobial Peptides of Multicellular Organisms. *Nature* 415 (2002), 389-395.

[47] K. Splith, I. Neundorf. Antimicrobial Peptides with Cell-Penetrating Peptide Properties and Vice Versa. *European Biophysics Journal* 40 (2011), 387-397.

[48] D. Andreu, L. Rivas. Animal Antimicrobial Peptides: An Overview. *Biopolymers* 47 (1998), 415-433.

[49] V. Teixeira, M.J. Feio, M. Bastos. Role of Lipids in the Interaction of Antimicrobial Peptides with Membranes. *Progress in Lipid Research* 51 (2012), 149-177.

[50] H.G. Boman. Peptide Antibiotics and Their Role in Innate Immunity. *Annual Review of Immunology* 13 (1995), 61-92.

[51] R.E.W. Hancock, G. Diamond. The Role of Cationic Antimicrobial Peptides in Innate Host Defences. *Trends in Microbiology* 8 (2000), 402-410.

[52] Y.P. Lai, R.L. Gallo. Amped up Immunity: How Antimicrobial Peptides Have Multiple Roles in Immune Defense. *Trends in Immunology* 30 (2009), 131-141.

[53] H. Zhao, P.K. Kinnunen. Modulation of the Activity of Secretory Phospholipase A_2 by Antimicrobial Peptides. *Antimicrobial Agents and Chemotherapy* 47 (2003), 965-971.

[54] K.A. Brogden. Antimicrobial Peptides: Pore Formers or Metabolic Inhibitors in Bacteria? *Nature Reviews Microbiology* 3 (2005), 238-250.

[55] K. Lohner, S.E. Blondelle. Molecular Mechanisms of Membrane Perturbation by Antimicrobial Peptides and the Use of Biophysical Studies in the Design of Novel Peptide Antibiotics. *Combinatorial Chemistry & High Throughput Screening* 8 (2005), 241-256.

[56] F. Harris, S.R. Dennison, J. Singh, D.A. Phoenix. On the Selectivity and Efficacy of Defense Peptides with Respect to Cancer Cells. *Medicinal Research Reviews* 33 (2013), 190-234.

[57] D.W. Hoskin, A. Ramamoorthy. Studies on Anticancer Activities of Antimicrobial Peptides. *Biochimica et Biophysica Acta-Biomembranes* 1778 (2008), 357-375.

[58] S. Liu, M. Yu, Y. He, L. Xiao, F. Wang, C. Song, S. Sun, C. Ling, Z. Xu. Melittin Prevents Liver Cancer Cell Metastasis through Inhibition of the Rac1-Dependent Pathway. *Hepatology* 47 (2008), 1964-1973.

[59] J. Lehmann, M. Retz, S.S. Sidhu, H. Suttmann, M. Sell, F. Paulsen, J. Harder, G. Unteregger, M. Stockle. Antitumor Activity of the Antimicrobial Peptide Magainin II against Bladder Cancer Cell Lines. *European Urology* 50 (2006), 141-147.

[60] E.G. Rodrigues, A.S. Dobroff, C.F. Cavarsan, T. Paschoalin, L. Nimrichter, R.A. Mortara, E.L. Santos, M.A. Fazio, A. Miranda, S. Daffre, L.R. Travassos. Effective

Topical Treatment of Subcutaneous Murine B16f10-Nex2 Melanoma by the Antimicrobial Peptide Gomesin. *Neoplasia* 10 (2008), 61-68.

[61] F. Schweizer. Cationic Amphiphilic Peptides with Cancer-Selective Toxicity. *European Journal of Pharmacology* 625 (2009), 190-194.

[62] M. Leeb. Antibiotics: A Shot in the Arm. *Nature* 431 (2004), 892-893.

[63] G. Bell, P.H. Gouyon. Arming the Enemy: The Evolution of Resistance to Self-Proteins. *Microbiology* 149 (2003), 1367-1375.

[64] A. Tossi, L. Sandri, A. Giangaspero. Amphipathic, Alpha-Helical Antimicrobial Peptides. *Biopolymers* 55 (2000), 4-30.

[65] G.S. Wang, X. Li, Z. Wang. Apd2: The Updated Antimicrobial Peptide Database and Its Application in Peptide Design. *Nucleic Acids Research* 37 (2009), D933-D937.

[66] Y. Shai. Mechanism of the Binding, Insertion and Destabilization of Phospholipid Bilayer Membranes by Alpha-Helical Antimicrobial and Cell Non-Selective Membrane-Lytic Peptides. *Biochimica et Biophysica Acta* 1462 (1999), 55-70.

[67] K. Hristova, C.E. Dempsey, S.H. White. Structure, Location, and Lipid Perturbations of Melittin at the Membrane Interface. *Biophysical Journal* 80 (2001), 801-811.

[68] B. Bechinger, E.S. Salnikov. The Membrane Interactions of Antimicrobial Peptides Revealed by Solid-State NMR Spectroscopy. *Chemistry and Physics of Lipids* 165 (2012), 282-301.

[69] Y. Huang, J. Huang, Y. Chen. Alpha-Helical Cationic Antimicrobial Peptides: Relationships of Structure and Function. *Protein & Cell* 1 (2010), 143-152.

[70] W.T. Heller, A.J. Waring, R.I. Lehrer, H.W. Huang. Multiple States of β-Sheet Peptide Protegrin in Lipid Bilayers. *Biochemistry* 37 (1998), 17331-17338.

[71] M.R. Yeaman, N.Y. Yount. Mechanisms of Antimicrobial Peptide Action and Resistance. *Pharmacological Reviews* 55 (2003), 27-55.

[72] S.E. Blondelle, R.A. Houghten. Hemolytic and Antimicrobial Activities of the Twenty-Four Individual Omission Analogues of Melittin. *Biochemistry* 30 (1991), 4671-4678.

[73] Z. Oren, J.C. Lerman, G.H. Gudmundsson, B. Agerberth, Y. Shai. Structure and Organization of the Human Antimicrobial Peptide Ll-37 in Phospholipid Membranes: Relevance to the Molecular Basis for Its Non-Cell-Selective Activity. *Biochemical Journal* 341 (1999), 501-513.

[74] J.K. Ghosh, D. Shaool, P. Guillaud, L. Ciceron, D. Mazier, I. Kustanovich, Y. Shai, A. Mor. Selective Cytotoxicity of Dermaseptin S3 toward Intraerythrocytic Plasmodium Falciparum and the Underlying Molecular Basis. *The Journal of Biological Chemistry* 272 (1997), 31609-31616.

[75] N. Papo, Y. Shai. Can We Predict Biological Activity of Antimicrobial Peptides from Their Interactions with Model Phospholipid Membranes? *Peptides* 24 (2003), 1693-1703.

[76] K.T. Nguyen, S.p.V. Le Clair, S. Ye, Z. Chen. Molecular Interactions between Magainin II and Model Membranes in Situ. *The Journal of Physical Chemistry B* 113 (2009), 12358-12363.

[77] P. Bougis, M. Tessier, J. Vanrietschoten, H. Rochat, J.F. Faucon, J. Dufourcq. Are Interactions with Phospholipids Responsible for Pharmacological Activities of Cardiotoxins. *Molecular and Cellular Biochemistry* 55 (1983), 49-64.

[78] W.T. Heller, A.J. Waring, R.I. Lehrer, T.A. Harroun, T.M. Weiss, L. Yang, H.W. Huang. Membrane Thinning Effect of the Beta-Sheet Antimicrobial Protegrin. *Biochemistry* 39 (2000), 139-145.

[79] H. Mozsolits, M.I. Aguilar. Surface Plasmon Resonance Spectroscopy: An Emerging Tool for the Study of Peptide-Membrane Interactions. *Biopolymers* 66 (2002), 3-18.

[80] J. Dufourcq, J.F. Faucon. Intrinsic Fluorescence Study of Lipid-Protein Interactions in Membrane Models. Binding of Melittin, an Amphipathic Peptide, to Phospholipid Vesicles. *Biochimica et Biophysica Acta* 467 (1977), 1-11.

[81] A. Wiese, M. Münstermann, T. Gutsmann, B. Lindner, K. Kawahara, U. Zähringer, U. Seydel. Molecular Mechanisms of Polymyxin B-Membrane Interactions: Direct Correlation between Surface Charge Density and Self-Promoted Transport. *Journal of Membrane Biology* 162 (1998), 127-138.

[82] M.T. Lee, F.Y. Chen, H.W. Huang. Energetics of Pore Formation Induced by Membrane Active Peptides. *Biochemistry* 43 (2004), 3590-3599.

[83] U.S. Sudheendra, B. Bechinger. Topological Equilibria of Ion Channel Peptides in Oriented Lipid Bilayers Revealed by 15N Solid-State NMR Spectroscopy. *Biochemistry* 44 (2005), 12120-12127.

[84] K. Matsuzaki, O. Murase, H. Tokuda, S. Funakoshi, N. Fujii, K. Miyajima. Orientational and Aggregational States of Magainin 2 in Phospholipid Bilayers. *Biochemistry* 33 (1994), 3342-3349.

[85] T. Gutsmann, S.O. Hagge, J.W. Larrick, U. Seydel, A. Wiese. Interaction of Cap18-derived Peptides with Membranes Made from Endotoxins or Phospholipids. *Biophysical Journal* 80 (2001), 2935-2945.

[86] M. Zanetti. The Role of Cathelicidins in the Innate Host Defenses of Mammals. *Current Issues in Molecular Biology* 7 (2005), 179-196.

[87] J.W. Larrick, M. Hirata, J. Zhong, S.C. Wright. Antimicrobial Activity of Human Cap18 Peptides. *Immunotechnology* 1 (1995), 65-72.

[88] G.S. Wang. Structures of Human Host Defense Cathelicidin LL-37 and Its Smallest Antimicrobial Peptide KR-12 in Lipid Micelles. *Journal of Biological Chemistry* 283 (2008), 32637-32643.

[89] J.B. Cowland, A.H. Johnsen, N. Borregaard. HCAP-18, a Cathelin/Pro-Bactenecin-Like Protein of Human Neutrophil Specific Granules. *FEBS Letters* 368 (1995), 173-176.

[90] G. Weber, C.I. Chamorro, F. Granath, A. Liljegren, S. Zreika, Z. Saidak, B. Sandstedt, S. Rotstein, R. Mentaverri, F. Sanchez, A. Pivarcsi, M. Stahle. Human Antimicrobial Protein hCAP18/LL-37 Promotes a Metastatic Phenotype in Breast Cancer. *Breast Cancer Research* 11 (2009), R6.

[91] S.M. Travis, N.N. Anderson, W.R. Forsyth, C. Espiritu, B.D. Conway, E.P. Greenberg, P.B. McCray, R.I. Lehrer, M.J. Welsh, B.F. Tack. Bactericidal Activity of Mammalian Cathelicidin-Derived Peptides. *Infection and Immunity* 68 (2000), 2748-2755.

[92] K. Okumura, A. Itoh, E. Isogai, K. Hirose, Y. Hosokawa, Y. Abiko, T. Shibata, M. Hirata, H. Isogai. C-Terminal Domain of Human Cap18 Antimicrobial Peptide Induces Apoptosis in Oral Squamous Cell Carcinoma Sas-H1 Cells. *Cancer Letters* 212 (2004), 185-194.

[93] S. Tripathi, T. Tecle, A. Verma, E. Crouch, M. White, K.L. Hartshorn. The Human Cathelicidin LL-37 Inhibits Influenza a Viruses through a Mechanism Distinct from That of Surfactant Protein D or Defensins. *Journal of General Virology* 94 (2012), 40-49.

[94] T. Sigurdardottir, P. Andersson, M. Davoudi, M. Malmsten, A. Schmidtchen, M. Bodelsson. In Silico Identification and Biological Evaluation of Antimicrobial Peptides Based on Human Cathelicidin LL-37. *Antimicrobial Agents and Chemotherapy* 50 (2006), 2983-2989.

[95] P.W. Tsai, C.Y. Yang, H.T. Chang, C.Y. Lan. Human Antimicrobial Peptide Ll-37 Inhibits Adhesion of Candida Albicans by Interacting with Yeast Cell-Wall Carbohydrates. *PLOS ONE* 6 (2011).

[96] D. Vandamme, B. Landuyt, W. Luyten, L. Schoofs. A Comprehensive Summary of LL-37, the Factotum Human Cathelicidin Peptide. *Cellular Immunology* 280 (2012), 22-35.

[97] J.W. Larrick, M. Hirata, R.F. Balint, J. Lee, J. Zhong, S.C. Wright. Human CAP18 - a Novel Antimicrobial Lipopolysaccharide-Binding Protein. *Infection and Immunity* 63 (1995), 1291-1297.

[98] Y.H. Nan, J.K. Bang, B. Jacob, I.S. Park, S.Y. Shin. Prokaryotic Selectivity and LPS-Neutralizing Activity of Short Antimicrobial Peptides Designed from the Human Antimicrobial Peptide Ll-37. *Peptides* 35 (2012), 239-247.

[99] F. Porcelli, R. Verardi, L. Shi, K.A. Henzler-Wildman, A. Ramamoorthy, G. Veglia. NMR Structure of the Cathelicidin-Derived Human Antimicrobial Peptide LL-37 in Dodecylphosphocholine Micelles. *Biochemistry* 47 (2008), 5565-5572.

[100] U.H.N. Durr, U.S. Sudheendra, A. Ramamoorthy. LL-37, the Only Human Member of the Cathelicidin Family of Antimicrobial Peptides. *Biochimica et Biophysica Acta-Biomembranes* 1758 (2006), 1408-1425.

[101] R. Bals, X. Wang, M. Zasloff, J.M. Wilson. The Peptide Antibiotic LL-37/hCAP-18 Is Expressed in Epithelia of the Human Lung Where It Has Broad Antimicrobial Activity at the Airway Surface. *Proceedings of the National Academy of Sciences of the United States of America* 95 (1998), 9541-9546.

[102] R. Shaykhiev, C. Beisswenger, K. Kandler, J. Senske, A. Puchner, T. Damm, J. Behr, R. Bals. Human Endogenous Antibiotic LL-37 Stimulates Airway Epithelial Cell

Proliferation and Wound Closure. *American Journal of Physiology - Lung Cellular and Molecular Physiology* 289 (2005), L842-L848.

[103] J. Schauber, R.L. Gallo. Antimicrobial Peptides and the Skin Immune Defense System. *Journal of Allergy and Clinical Immunology* 122 (2008), 261-266.

[104] J.A. Hensel, D. Chanda, S. Kumar, A. Sawant, W.E. Grizzle, G.P. Siegal, S. Ponnazhagan. LL-37 as a Therapeutic Target for Late Stage Prostate Cancer. *The Prostate* 71 (2011), 659-670.

[105] J.D. Heilborn, M.F. Nilsson, C.I.C. Jimenez, B. Sandstedt, N. Borregaard, E. Tham, O.E. Sørensen, G. Weber, M. Ståhle. Antimicrobial Protein hCAP18/LL-37 Is Highly Expressed in Breast Cancer and Is a Putative Growth Factor for Epithelial Cells. *International Journal of Cancer* 114 (2005), 713-719.

[106] S.B. Coffelt, R.S. Waterman, L. Florez, K.H.z. Bentrup, K.J. Zwezdaryk, S.L. Tomchuck, H.L. LaMarca, E.S. Danka, C.A. Morris, A.B. Scandurro. Ovarian Cancers Overexpress the Antimicrobial Protein hCAP-18 and Its Derivative LL-37 Increases Ovarian Cancer Cell Proliferation and Invasion. *International Journal of Cancer* 122 (2008), 1030-1039.

[107] J. von Haussen, R. Koczulla, R. Shaykhiev, C. Herr, O. Pinkenburg, D. Reimer, R. Wiewrodt, S. Biesterfeld, A. Aigner, F. Czubayko, R. Bals. The Host Defence Peptide LL-37/hCAP-18 Is a Growth Factor for Lung Cancer Cells. *Lung Cancer* 59 (2008), 12-23.

[108] L.M. Coussens, Z. Werb. Inflammation and Cancer. *Nature* 420 (2002), 860-867.

[109] S.P. Hussain, C.C. Harris. Inflammation and Cancer: An Ancient Link with Novel Potentials. *International journal of cancer* 121 (2007), 2373-2380.

[110] W.K.K. Wu, G. Wang, S.B. Coffelt, A.M. Betancourt, C.W. Lee, D. Fan, K. Wu, J. Yu, J.J.Y. Sung, C.H. Cho. Emerging Roles of the Host Defense Peptide LL-37 in Human Cancer and Its Potential Therapeutic Applications. *International Journal of Cancer* 127 (2010), 1741-1747.

[111] A. Ramamoorthy, D.K. Lee, J.S. Santos, K.A. Henzler-Wildman. Nitrogen-14 Solid-State NMR Spectroscopy of Aligned Phospholipid Bilayers to Probe Peptide-Lipid Interaction and Oligomerization of Membrane Associated Peptides. *Journal of the American Chemical Society* 130 (2008), 11023-11029.

[112] K.A. Henzler-Wildman, G.V. Martinez, M.F. Brown, A. Ramamoorthy. Perturbation of the Hydrophobic Core of Lipid Bilayers by the Human Antimicrobial Peptide LL-37. *Biochemistry* 43 (2004), 8459-8469.

[113] C.C. Lee, Y. Sun, S. Qian, H.W. Huang. Transmembrane Pores Formed by Human Antimicrobial Peptide LL-37. *Biophysical Journal* 100 (2011), 1688-1696.

[114] K.A.H. Wildman, D.K. Lee, A. Ramamoorthy. Mechanism of Lipid Bilayer Disruption by the Human Antimicrobial Peptide, LL-37. *Biochemistry* 42 (2003), 6545-6558.

[115] J.E. Gable, D.E. Schlamadinger, A.L. Cogen, R.L. Gallo, J.E. Kim. Fluorescence and UV Resonance Raman Study of Peptide−Vesicle Interactions of Human Cathelicidin LL-37 and Its F6W and F17W Mutants. *Biochemistry* 48 (2009), 11264-11272.

[116] J. Turner, Y. Cho, N.N. Dinh, A.J. Waring, R.I. Lehrer. Activities of LL-37, a Cathelin-Associated Antimicrobial Peptide of Human Neutrophils. *Antimicrobial Agents and Chemotherapy* 42 (1998), 2206-2214.

[117] R.F. Epand, G. Wang, B. Berno, R.M. Epand. Lipid Segregation Explains Selective Toxicity of a Series of Fragments Derived from the Human Cathelicidin LL-37. *Antimicrobial Agents and Chemotherapy* 53 (2009), 3705-3714.

[118] S. Thennarasu, A.M. Tan, R. Penumatchu, C.E. Shelburne, D.L. Heyl, A. Ramamoorthy. Antimicrobial and Membrane Disrupting Activities of a Peptide Derived from the Human Cathelicidin Antimicrobial Peptide LL-37. *Biophysical Journal* 98 (2010), 248-257.

[119] X.A. Zhang, K. Oglecka, S. Sandgren, M. Belting, E.K. Esbjorner, B. Norden, A. Graslund. Dual Functions of the Human Antimicrobial Peptide LL-37-Target Membrane Perturbation and Host Cell Cargo Delivery. *Biochimica et Biophysica Acta-Biomembranes* 1798 (2010), 2201-2208.

[120] T. Gutsmann, J.W. Larrick, U. Seydel, A. Wiese. Molecular Mechanisms of Interaction of Rabbit CAP 18 with Outer Membranes of Gram-Negative Bacteria. *Biochemistry* 38 (1999), 13643-13653.

[121] J. Johansson, G.H. Gudmundsson, M.E. Rottenberg, K.D. Berndt, B. Agerberth. Conformation-Dependent Antibacterial Activity of the Naturally Occurring Human Peptide LL-37. *Journal of Biological Chemistry* 273 (1998), 3718-3724.

[122] N. Papo, Y. Shai. Host Defense Peptides as New Weapons in Cancer Treatment. *Cellular and Molecular Life Sciences* 62 (2005), 784-790.

[123] C. Leuschner, W. Hansel. Membrane Disrupting Lytic Peptides for Cancer Treatments. *Current Pharmaceutical Design* 10 (2004), 2299-2310.

[124] N.R. Soman, S.L. Baldwin, G. Hu, J.N. Marsh, G.M. Lanza, J.E. Heuser, J.M. Arbeit, S.A. Wickline, P.H. Schlesinger. Molecularly Targeted Nanocarriers Deliver the Cytolytic Peptide Melittin Specifically to Tumor Cells in Mice, Reducing Tumor Growth. *The Journal of Clinical Investigation* 119 (2009), 2830-2842.

[125] H. Pan, N.R. Soman, P.H. Schlesinger, G.M. Lanza, S.A. Wickline. Cytolytic Peptide Nanoparticles ('Nanobees') for Cancer Therapy. *Wiley Interdisciplinary Reviews. Nanomedicine and Nanobiotechnology* 3 (2011), 318-327.

[126] A. Héquet, V. Humblot, J.-M. Berjeaud, C.-M. Pradier. Optimized Grafting of Antimicrobial Peptides on Stainless Steel Surface and Biofilm Resistance Tests. *Colloids and Surfaces B: Biointerfaces* 84 (2011), 301-309.

[127] F. Costa, I.F. Carvalho, R.C. Montelaro, P. Gomes, M.C.L. Martins. Covalent Immobilization of Antimicrobial Peptides (AMPs) onto Biomaterial Surfaces. *Acta Biomaterialia* 7 (2011), 1431-1440.

[128] R. Gennaro, M. Zanetti. Structural Features and Biological Activities of the Cathelicidin-Derived Antimicrobial Peptides. *Biopolymers* 55 (2000), 31-49.

[129] R.P. Dellinger, M.M. Levy, A. Rhodes, D. Annane, H. Gerlach, S.M. Opal, J.E. Sevransky, C.L. Sprung, I.S. Douglas, R. Jaeschke, T.M. Osborn, M.E. Nunnally, S.R.

Townsend, K. Reinhart, R.M. Kleinpell, D.C. Angus, C.S. Deutschman, F.R. Machado, G.D. Rubenfeld, S.A. Webb, R.J. Beale, J.L. Vincent, R. Moreno. Surviving Sepsis Campaign: International Guidelines for Management of Severe Sepsis and Septic Shock: 2012. *Critical Care Medicine* 41 (2013), 580-637.

[130] G.S. Wang. Determination of Solution Structure and Lipid Micelle Location of an Engineered Membrane Peptide by Using One NMR Experiment and One Sample. *Biochimica et Biophysica Acta-Biomembranes* 1768 (2007), 3271-3281.

[131] G. Thakur, M. Micic, R.M. Leblanc. Surface Chemistry of Alzheimer's Disease: A Langmuir Monolayer Approach. *Colloids and Surfaces B-Biointerfaces* 74 (2009), 436-456.

[132] H. Mohwald. Phospholipid and Phospholipid-Protein Monolayers at the Air/Water Interface. *Annual Review of Physical Chemistry* 41 (1990), 441-476.

[133] E.E. Ambroggio, F. Separovic, J. Bowie, G.D. Fidelio. Surface Behaviour and Peptide-Lipid Interactions of the Antibiotic Peptides, Maculatin and Citropin. *Biochimica et Biophysica Acta-Biomembranes* 1664 (2004), 31-37.

[134] C.R. Flach, J.W. Brauner, J.W. Taylor, R.C. Baldwin, R. Mendelsohn. External Reflection Ftir of Peptide Monolayer Films in-Situ at the Air/Water Interface - Experimental-Design, Spectra-Structure Correlations, and Effects of Hydrogen-Deuterium Exchange. *Biophysical Journal* 67 (1994), 402-410.

[135] T.R. Jensen, K. Balashev, T. Bjornholm, K. Kjaer. Novel Methods for Studying Lipids and Lipases and Their Mutual Interaction at Interfaces. Part II. Surface Sensitive Synchrotron X-Ray Scattering. *Biochimie* 83 (2001), 399-408.

[136] F. Neville, M. Cahuzac, O. Konovalov, Y. Ishitsuka, K.Y.C. Lee, I. Kuzmenko, G.M. Kale, D. Gidalevitz. Lipid Headgroup Discrimination by Antimicrobial Peptide LL-37: Insight into Mechanism of Action. *Biophysical Journal* 90 (2006), 1275-1287.

[137] R. Mendelsohn, G. Mao, C.R. Flach. Infrared Reflection-Absorption Spectroscopy: Principles and Applications to Lipid-Protein Interaction in Langmuir Films. *Biochimica et Biophysica Acta* 1798 (2010), 788-800.

[138] S. Brahms, J. Brahms. Determination of Protein Secondary Structure in Solution by Vacuum Ultraviolet Circular Dichroism. *Journal of molecular biology* 138 (1980), 149-178.

[139] J.P. Slotte, B. Ramstedt. The Functional Role of Sphingomyelin in Cell Membranes. *European Journal of Lipid Science and Technology* 109 (2007), 977-981.

[140] N. Bezlyepkina, R.S. Gracià, P. Shchelokovskyy, R. Lipowsky, R. Dimova. Phase Diagram and Tie-Line Determination for the Ternary Mixture Dopc/Esm/Cholesterol. *Biophysical Journal* 104 (2013), 1456-1464.

[141] T.K.M. Nyholm, D. Lindroos, B. Westerlund, J.P. Slotte. Construction of a DOPC/PSM/Cholesterol Phase Diagram Based on the Fluorescence Properties of Trans-Parinaric Acid. *Langmuir* 27 (2011), 8339-8350.

[142] S.L. Veatch, S.L. Keller. Miscibility Phase Diagrams of Giant Vesicles Containing Sphingomyelin. *Physical Review Letters* 94 (2005), 148101.

[143] M.U. Hammer. Struktur-Wirkungsbeziehungen Zwischen Membranaktiven Peptiden Und Bakteriellen Lipopolysacchariden. *Dissertation*. Christian-Albrechts-Univerisität. Kiel 2007.

[144] M.H. Braff, M.A. Hawkins, A. Di Nardo, B. Lopez-Garcia, M.D. Howell, C. Wong, K. Lin, J.E. Streib, R. Dorschner, D.Y.M. Leung, R.L. Gallo. Structure-Function Relationships among Human Cathelicidin Peptides: Dissociation of Antimicrobial Properties from Host Immunostimulatory Activities. *Journal of Immunology* 174 (2005), 4271-4278.

[145] C. Röbke. Synthetische Derivate Des Humanen Cathelicidins Hcap18/Ll37 Sind Potentielle, Antitumorale Medikamente. *Dissertation*. Universität zu Lübeck. Lübeck 2011.

[146] D. Eisenberg, R.M. Weiss, T.C. Terwilliger, W. Wilcox. Hydrophobic Moments and Protein-Structure. *Faraday Symposia of the Chemical Society* (1982), 109-120.

[147] A. Tossi, L. Sandri.

http://Www.Bbcm.Univ.Trieste.It/~Tossi/Hydrocalc/Hydromcalc.Html#Run.

[148] C. Snider, S. Jayasinghe, K. Hristova, S.H. White. Mpex: A Tool for Exploring Membrane Proteins. *Protein Science* 18 (2009), 2624-2628.

[149] L. Whitmore, B. Woollett, A.J. Miles, R.W. Janes, B.A. Wallace. The Protein Circular Dichroism Data Bank, a Web-Based Site for Access to Circular Dichroism Spectroscopic Data. *Structure* 18 (2010), 1267-1269.

[150] L. Whitmore, B.A. Wallace. Protein Secondary Structure Analyses from Circular Dichroism Spectroscopy: Methods and Reference Databases. *Biopolymers* 89 (2008), 392-400.

[151] K. Park, A. Perczel, G.D. Fasman. Differentiation between Transmembrane Helices and Peripheral Helices by the Deconvolution of Circular Dichroism Spectra of Membrane Proteins. *Protein Science* 1 (1992), 1032-1049.

[152] T.V. Ovchinnikova, Z.O. Shenkarev, S.V. Balandin, K.D. Nadezhdin, A.S. Paramonov, V.N. Kokryakov, A.S. Arseniev. Molecular Insight into Mechanism of Antimicrobial Action of the Beta-Hairpin Peptide Arenicin: Specific Oligomerization in Detergent Micelles. *Biopolymers* 89 (2008), 455-464.

[153] L.N.M. Duysens. The Flattening of the Absorption Spectrum of Suspensions, as Compared to That of Solutions. *Biochimica et Biophysica Acta* 19 (1956), 1-12.

[154] S.M. Kelly, T.J. Jess, N.C. Price. How to Study Proteins by Circular Dichroism. *Biochimica et Biophysica Acta-Proteins and Proteomics* 1751 (2005), 119-139.

[155] R. Ziblat, L. Leiserowitz, L. Addadi. Crystalline Lipid Domains: Characterization by X-Ray Diffraction and Their Relation to Biology. *Angewandte Chemie-International Edition* 50 (2011), 3620-3629.

[156] L.K. Tamm, S.A. Tatulian. Infrared Spectroscopy of Proteins and Peptides in Lipid Bilayers. *Quarterly Reviews of Biophysics* 30 (1997), 365-429.

[157] M. Jackson, H.H. Mantsch. The Use and Misuse of FTIR Spectroscopy in the Determination of Protein-Structure. *Critical Reviews in Biochemistry and Molecular Biology* 30 (1995), 95-120.

[158] T. Buffeteau, E. Le Calvez, S. Castano, B. Desbat, D. Blaudez, J. Dufourcq. Anisotropic Optical Constants of A-Helix and β-Sheet Secondary Structures in the Infrared. *The Journal of Physical Chemistry B* 104 (2000), 4537-4544.

[159] T.R. Jensen, K. Kjaer, Structural Properties and Interactions of Thin Films at the Air-Liquid Interface Explored by Synchrotron X-Ray Scattering. in: D. Möbius, R. Miller (Eds.), Studies in Interface Science, 2001, pp. 205-254.

[160] J. Als-Nielsen, D. Jacquemain, K. Kjaer, F. Leveiller, M. Lahav, L. Leiserowitz. Principles and Applications of Grazing-Incidence X-Ray and Neutron-Scattering from Ordered Molecular Monolayers at the Air-Water-Interface. *Physics Reports-Review Section of Physics Letters* 246 (1994), 252-313.

[161] A. Hermelink. Phosphatidylinositole 3-Kinase Γ – Characterization of a Protein-Lipid Interaction. *Dissertation*. Humboldt-Universität. Berlin 2008.

[162] O.G. Travkova. Interactions of the Antimicrobial Peptide Arenicin with Amphiphiles at Planar and Curved Interfaces. *Dissertation*. Universität Potsdam. Potsdam 2010.

[163] J.S. Pedersen, I.W. Hamley. Analysis of Neutron and X-Ray Reflectivity Data. 2. Constrained Least-Squares Methods. *Journal of Applied Crystallography* 27 (1994), 36-49.

[164] E. Lacroix, A.R. Viguera, L. Serrano. Elucidating the Folding Problem of A-Helices: Local Motifs, Long-Range Electrostatics, Ionic-Strength Dependence and Prediction of Nmr Parameters. *Journal of Molecular Biology* 284 (1998), 173-191.

[165] S.W. Provencher. Contin - a General-Purpose Constrained Regularization Program for Inverting Noisy Linear Algebraic and Integral-Equations. *Computer Physics Communications* 27 (1982), 229-242.

[166] M. Hoernke, J.A. Falenski, C. Schwieger, B. Koksch, G. Brezesinski. Triggers for Beta-Sheet Formation at the Hydrophobic-Hydrophilic Interface: High Concentration, in-Plane Orientational Order, and Metal Ion Complexation. *Langmuir* (2011).

[167] A. Meister, A. Kerth, A. Blume. Interaction of Sodium Dodecyl Sulfate with Dimyristoyl-Sn-Glycero-3-Phosphocholine Monolayers Studied by Infrared Reflection Absorption Spectroscopy. A New Method for the Determination of Surface Partition Coefficients. *Journal of Physical Chemistry B* 108 (2004), 8371-8378.

[168] B. Zagrovic, G. Jayachandran, I.S. Millett, S. Doniach, V.S. Pande. How Large Is an Alpha-Helix? Studies of the Radii of Gyration of Helical Peptides by Small-Angle X-Ray Scattering and Molecular Dynamics. *Journal of Molecular Biology* 353 (2005), 232-241.

[169] C.R. Flach, F.G. Prendergast, R. Mendelsohn. Infrared Reflection-Absorption of Melittin Interaction with Phospholipid Monolayers at the Air/Water Interface. *Biophysical Journal* 70 (1996), 539-546.

[170] P. Calvez, S. Bussieres, E. Demers, C. Salesse. Parameters Modulating the Maximum Insertion Pressure of Proteins and Peptides in Lipid Monolayers. *Biochimie* 91 (2009), 718-733.

[171] P. Calvez, E. Demers, E. Boisselier, C. Salesse. Analysis of the Contribution of Saturated and Polyunsaturated Phospholipid Monolayers to the Binding of Proteins. *Langmuir* 27 (2011), 1373-1379.

[172] E. Boisselier, P. Calvez, E. Demers, L. Cantin, C. Salesse. Influence of the Physical State of Phospholipid Monolayers on Protein Binding. *Langmuir* 28 (2012), 9680-9688.

[173] T. Wieprecht, M. Dathe, E. Krause, M. Beyermann, W.L. Maloy, D.L. MacDonald, M. Bienert. Modulation of Membrane Activity of Amphipathic, Antibacterial Peptides by Slight Modifications of the Hydrophobic Moment. *FEBS Letters* 417 (1997), 135-140.

[174] T. Kiyota, S. Lee, G. Sugihara. Design and Synthesis of Amphiphilic Alpha-Helical Model Peptides with Systematically Varied Hydrophobic-Hydrophilic Balance and Their Interaction with Lipid- and Bio-Membranes. *Biochemistry* 35 (1996), 13196-13204.

[175] W.T. Heller, K. He, S.J. Ludtke, T.A. Harroun, H.W. Huang. Effect of Changing the Size of Lipid Headgroup on Peptide Insertion into Membranes. *Biophysical Journal* 73 (1997), 239-244.

[176] M. Hoernke, C. Schwieger, A. Kerth, A. Blume. Binding of Cationic Pentapeptides with Modified Side Chain Lengths to Negatively Charged Lipid Membranes: Complex Interplay of Electrostatic and Hydrophobic Interactions. *Biochimica et Biophysica Acta-Biomembranes* 1818 (2012), 1663-1672.

[177] C. Schwieger, A. Blume. Interaction of Poly(L-Arginine) with Negatively Charged DPPG Membranes: Calorimetric and Monolayer Studies. *Biomacromolecules* 10 (2009), 2152-2161.

[178] P. Bougis, H. Rochat, G. Pieroni, R. Verger. Penetration of Phospholipid Monolayers by Cardiotoxins. *Biochemistry* 20 (1981), 4915-4920.

[179] D. Gidalevitz, Y. Ishitsuka, A.S. Muresan, O. Konovalov, A.J. Waring, R.I. Lehrer, K.Y. Lee. Interaction of Antimicrobial Peptide Protegrin with Biomembranes. *Proceedings of the National Academy of Sciences of the United States of America* 100 (2003), 6302-6307.

[180] A. Meister, A. Kerth, A. Blume. Adsorption Kinetics of N-Nonyl-Beta-D-Glucopyranoside at the Air-Water Interface Studied by Infrared Reflection Absorption Spectroscopy. *The Journal of Physical Chemistry B* 109 (2005), 6239-6246.

[181] S.T.R. Walsh, R.P. Cheng, W.W. Wright, D.O.V. Alonso, V. Daggett, J.M. Vanderkooi, W.F. DeGrado. The Hydration of Amides in Helices; a Comprehensive Picture from Molecular Dynamics, IR, and NMR. *Protein Science* 12 (2003), 520-531.

[182] Y.P. Zhang, R.N.A.H. Lewis, R.S. Hodges, R.N. McElhaney. Interaction of a Peptide Model of a Hydrophobic Transmembrane Alpha-Helical Segment of a Membrane-Protein with Phosphatidylcholine Bilayers - Differential Scanning Calorimetric and Ftir Spectroscopic Studies. *Biochemistry* 31 (1992), 11579-11588.

[183] S. Mukherjee, P. Chowdhury, F. Gai. Infrared Study of the Effect of Hydration on the Amide I Band and Aggregation Properties of Helical Peptides. *Journal of Physical Chemistry B* 111 (2007), 4596-4602.

[184] M. Albrecht, C.A. Rice, M.A. Suhm. Elementary Peptide Motifs in the Gas Phase: Ftir Aggregation Study of Formamide, Acetamide, N-Methylformamide, and N-Methylacetamide. *Journal of Physical Chemistry A* 112 (2008), 7530-7542.

[185] R. Ludwig, O. Reis, R. Winter, F. Weinhold, T.C. Farrar. Quantum Cluster Equilibrium Theory of Liquids: Temperature Dependence of Hydrogen Bonding in Liquid N-Methylacetamide Studied by IR Spectra. *Journal of Physical Chemistry B* 102 (1998), 9312-9318.

[186] K. Hąc-Wydro, M. Flasiński, M. Broniatowski, P. Dynarowicz-Łątka, J. Majewski. Properties of B-Sitostanol/DPPc Monolayers Studied with Grazing Incidence X-Ray Diffraction (GIXD) and Brewster Angle Microscopy. *Journal of Colloid and Interface Science* 364 (2011), 133-139.

[187] K. Wagner, G. Brezesinski. Modifying Dipalmitoylphosphatidylcholine Monolayers by N-Hexadecanol and Dipalmitoylglycerol. *Chemistry and Physics of Lipids* 145 (2007), 119-127.

[188] Y.F. Li, X. Li, G.S. Wang. Cloning, Expression, Isotope Labeling, and Purification of Human Antimicrobial Peptide Ll-37 in Escherichia Coli for Nmr Studies. *Protein Expression and Purification* 47 (2006), 498-505.

[189] A.S. Ladokhin, S.H. White. Folding of Amphipathic Alpha-Helices on Membranes: Energetics of Helix Formation by Melittin. *Journal of Molecular Biology* 285 (1999), 1363-1369.

[190] B. Ramstedt, J.P. Slotte. Interaction of Cholesterol with Sphingomyelins and Acyl-Chain-Matched Phosphatidylcholines: A Comparative Study of the Effect of the Chain Length. *Biophysical Journal* 76 (1999), 908-915.

[191] X.-M. Li, M.M. Momsen, H.L. Brockman, R.E. Brown. Sterol Structure and Sphingomyelin Acyl Chain Length Modulate Lateral Packing Elasticity and Detergent Solubility in Model Membranes. *Biophysical Journal* 85 (2003), 3788-3801.

[192] C.E. Miller, D.D. Busath, B. Strongin, J. Majewski. Integration of Ganglioside Gt(1b) Receptor into DPPE and DPPC Phospholipid Monolayers: An X-Ray Reflectivity and Grazing-Incidence Diffraction Study. *Biophysical Journal* 95 (2008), 3278-3286.

[193] D. Vaknin, M.S. Kelley, B.M. Ocko. Sphingomyelin at the Air-Water Interface. *Journal of Chemical Physics* 115 (2001), 7697-7704.

[194] F. Evers, C. Jeworrek, K. Weise, M. Tolan, R. Winter. Detection of Lipid Raft Domains in Neutral and Anionic Langmuir Monolayers and Bilayers of Complex Lipid Composition. *Soft Matter* 8 (2012), 2170-2175.

[195] L.R. Arriaga, I. Lopez-Montero, J. Ignes-Mullol, F. Monroy. Domain-Growth Kinetic Origin of Nonhorizontal Phase Coexistence Plateaux in Langmuir Monolayers: Compression Rigidity of a Raft-Like Lipid Distribution. *Journal of Physical Chemistry B* 114 (2010), 4509-4520.

[196] P.R. Maulik, G.G. Shipley. Interactions of N-Stearoyl Sphingomyelin with Cholesterol and Dipalmitoyl Phosphatidylcholine in Bilayer Membranes. *Biophysical Journal* 70 (1996), 2256-2265.

[197] M. Broniatowski, M. Flasiński, P. Dynarowicz-Łątka, J. Majewski. Grazing Incidence Diffraction and X-Ray Reflectivity Studies of the Interactions of Inorganic Mercury Salts with Membrane Lipids in Langmuir Monolayers at the Air/Water Interface. *The Journal of Physical Chemistry B* 114 (2010), 9474-9484.

[198] P.R. Maulik, G.G. Shipley. X-Ray Diffraction and Calorimetric Study of N-Lignoceryl Sphingomyelin Membranes. *Biophysical Journal* 69 (1995), 1909-1916.

[199] N.R. Pallas, B.A. Pethica. Liquid-Expanded to Liquid-Condensed Transition in Lipid Monolayers at the Air/Water Interface. *Langmuir* 1 (1985), 509-513.

[200] E. Hatta, T. Nishimura. Distribution of Cooperative Unit Size of Amphiphilic Molecules in the Phase Coexistence Region in Langmuir Monolayers. *Journal of Colloid and Interface Science* 391 (2013), 111-115.

[201] J. Villalain, A. Ortiz, J.C. Gomezfernandez. Molecular-Interactions between Sphingomyelin and Phosphatidylcholine in Phospholipid-Vesicles. *Biochimica et Biophysica Acta* 941 (1988), 55-62.

[202] S.W. Chiu, S. Vasudevan, E. Jakobsson, R.J. Mashl, H.L. Scott. Structure of Sphingomyelin Bilayers: A Simulation Study. *Biophysical Journal* 85 (2003), 3624-3635.

[203] N. Kahya, D. Scherfeld, K. Bacia, B. Poolman, P. Schwille. Probing Lipid Mobility of Raft-Exhibiting Model Membranes by Fluorescence Correlation Spectroscopy. *Journal of Biological Chemistry* 278 (2003), 28109-28115.

[204] S.A. Pandit, E. Jakobsson, H.L. Scott. Simulation of the Early Stages of Nano-Domain Formation in Mixed Bilayers of Sphingomyelin, Cholesterol, and Dioleylphosphatidylcholine. *Biophysical Journal* 87 (2004), 3312-3322.

[205] J.C. Lawrence, D.E. Saslowsky, J.M. Edwardson, R.M. Henderson. Real-Time Analysis of the Effects of Cholesterol on Lipid Raft Behavior Using Atomic Force Microscopy. *Biophysical Journal* 84 (2003), 1827-1832.

[206] R.S. Petruzielo, F.A. Heberle, P. Drazba, J. Katsaras, G.W. Feigenson. Phase Behavior and Domain Size in Sphingomyelin-Containing Lipid Bilayers. *Biochimica et Biophysica Acta (BBA) - Biomembranes* 1828 (2013), 1302-1313.

[207] C. Chipot, A. Pohorille. Structure and Dynamics of Small Peptides at Aqueous Interfaces a Multi-Nanosecond Molecular Dynamics Study. *Journal of Molecular Structure: THEOCHEM* 398–399 (1997), 529-535.

[208] T. Gutsmann, M. Fix, J.W. Larrick, A. Wiese. Mechanisms of Action of Rabbit CAP18 on Monolayers and Liposomes Made from Endotoxins of Phospholipids. *Journal of Membrane Biology* 176 (2000), 223-236.

[209] F. Neville, Y. Ishitsuka, C.S. Hodges, O. Konovalov, A.J. Waring, R. Lehrer, K.Y. Lee, D. Gidalevitz. Protegrin Interaction with Lipid Monolayers: Grazing Incidence X-Ray Diffraction and X-Ray Reflectivity Study. *Soft Matter* 4 (2008), 1665-1674.

[210] F. Neville, A. Ivankin, O. Konovalov, D. Gidalevitz. A Comparative Study on the Interactions of SMAP-29 with Lipid Monolayers. *Biochimica et Biophysica Acta* 1798 (2010), 851-860.

[211] S.-F. Sui, H. Wu, Y. Guo, K.-S. Chen. Conformational Changes of Melittin Upon Insertion into Phospholipid Monolayer and Vesicle. *The Journal of Biochemistry* 116 (1994), 482-487.

[212] M.H. Park, M.S. Choi, D.H. Kwak, K.W. Oh, Y. Yoon do, S.B. Han, H.S. Song, M.J. Song, J.T. Hong. Anti-Cancer Effect of Bee Venom in Prostate Cancer Cells through Activation of Caspase Pathway Via Inactivation of NF-KB. *Prostate* 71 (2011), 801-812.

[213] A.S. Ladokhin, S.H. White. 'Detergent-Like' Permeabilization of Anionic Lipid Vesicles by Melittin. *Biochimica et Biophysica Acta* 1514 (2001), 253-260.

[214] E. Sevcsik, G. Pabst, A. Jilek, K. Lohner. How Lipids Influence the Mode of Action of Membrane-Active Peptides. *Biochimica et Biophysica Acta (BBA) - Biomembranes* 1768 (2007), 2586-2595.

[215] M.J. Gomara, S. Nir, J.L. Nieva. Effects of Sphingomyelin on Melittin Pore Formation. *Biochimica et Biophysica Acta-Biomembranes* 1612 (2003), 83-89.

[216] D.J. Son, J.W. Lee, Y.H. Lee, H.S. Song, C.K. Lee, J.T. Hong. Therapeutic Application of Anti-Arthritis, Pain-Releasing, and Anti-Cancer Effects of Bee Venom and Its Constituent Compounds. *Pharmacology & Therapeutics* 115 (2007), 246-270.

[217] Y. Cajal, M.K. Jain. Synergism between Melittin and Phospholipase A_2 from Bee Venom: Apparent Activation by Intervesicle Exchange of Phospholipids. *Biochemistry* 36 (1997), 3882-3893.

[218] S. Pochet, S. Tandel, S. Querriere, M. Tre-Hardy, M. Garcia-Marcos, M. De Lorenzi, M. Vandenbranden, A. Marino, M. Devleeschouwer, J.P. Dehaye. Modulation by LL-37 of the Responses of Salivary Glands to Purinergic Agonists. *Molecular Pharmacology* 69 (2006), 2037-2046.

[219] K. Wagner, B. Desbat, G. Brezesinski. Liquid–Liquid Immiscibility in Model Membranes Activates Secretory Phospholipase A_2. *Biochimica et Biophysica Acta (BBA) - Biomembranes* 1778 (2008), 166-174.

[220] K. Wagner. The Regulation of Phospholipase Activity by Lipid Membrane Structure. *Dissertation*. Universität Potsdam. Potsdam 2007.

[221] A. Arouri, M. Dathe, A. Blume. Peptide Induced Demixing in PG/PE Lipid Mixtures: A Mechanism for the Specificity of Antimicrobial Peptides Towards Bacterial Membranes? *Biochimica et Biophysica Acta* 1788 (2009), 650-659.

[222] M. Deleu, J. Lorent, L. Lins, R. Brasseur, N. Braun, K. El Kirat, T. Nylander, Y.F. Dufrene, M.P. Mingeot-Leclercq. Effects of Surfactin on Membrane Models Displaying Lipid Phase Separation. *Biochimica et Biophysica Acta (BBA)* 1828 (2013), 801-815.

[223] P. Schön, A.J. García-Sáez, P. Malovrh, K. Bacia, G. Anderluh, P. Schwille. Equinatoxin II Permeabilizing Activity Depends on the Presence of Sphingomyelin and Lipid Phase Coexistence. *Biophysical Journal* 95 (2008), 691-698.

[224] P. Wessman, A.A. Stromstedt, M. Malmsten, K. Edwards. Melittin-Lipid Bilayer Interactions and the Role of Cholesterol. *Biophysical Journal* 95 (2008), 4324-4336.

[225] R. Sood, P.K.J. Kinnunen. Cholesterol, Lanosterol, and Ergosterol Attenuate the Membrane Association of LL-37(W27F) and Temporin L. *Biochimica et Biophysica Acta-Biomembranes* 1778 (2008), 1460-1466.

[226] M. Dyck, A. Kerth, A. Blume, M. Losche. Interaction of the Neurotransmitter, Neuropeptide Y, with Phospholipid Membranes: Infrared Spectroscopic Characterization at the Air/Water Interface. *Journal of Physical Chemistry B* 110 (2006), 22152-22159.

[227] V.L.M. Kuzmin, A.V. Molecular Theory of Light Reflection and Applicability Limits of the Macroscopic Approach. *Optics and Spectroscopy-USSR* 51 (1981), 383-385.

[228] T.V. Ovchinnikova, Z.V. Shenkarev, K.D. Nadezhdin, S.V. Balandin, M.N. Zhmak, I.A. Kudelina, E.I. Finkina, V.N. Kokryakov, A.S. Arseniev. Recombinant Expression, Synthesis, Purification, and Solution Structure of Arenicin. *Biochemical and Biophysical Research Communications* 360 (2007), 156-162.

[229] E. Glukhov, L.L. Burrows, C.M. Deber. Membrane Interactions of Designed Cationic Antimicrobial Peptides: The Two Thresholds. *Biopolymers* 89 (2008), 360-371.

VIII. Appendix

VIII.1 Simulation of LL-32 at the Air/Water Interface

Figure A1 illustrates the IRRA spectrum of LL-32 adsorbed at the air/water interface compared to a simulated spectrum. The spectrum can be best described by an α-helix with its helical axis in the surface plane. The effective thickness of the monolayer was chosen to be 14 Å based on fits to the height of the OH stretching band in the IRRA spectra at 3600 cm^{-1}. The extinction coefficients of the peaks were chosen to best fit the experimental data (k_{max}(amide I) = 1.4 and k_{max}(amide II) = 0.67). The determined values are in good agreement with literature [158; 226]. The simulated spectra are in good agreement with the experimental IRRA spectra. Therefore, the comparison of measured spectra with simulated ones indicates that LL-32 forms an α-helix oriented parallel to the interface. In conclusion, using IRRA spectra acquired with p-polarized light at various angles of incidence shows that the peptide adsorbed at the interface forms an α-helix, although the peptide has a predominantly random coil conformation in buffer, as proved by CD spectroscopy.

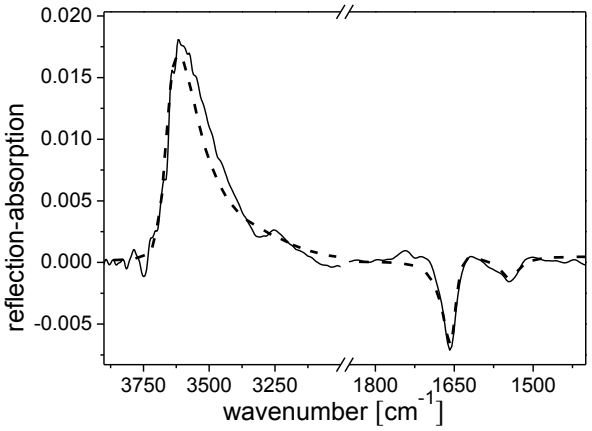

Figure A1: IRRA spectrum between 4000 cm^{-1} and 1400 cm^{-1} of LL-32 (5 mM HEPES, 100 mM NaCl, pH 7.4, 20 °C, 0.2 µM peptide in solution, π_{eq} = 24 mN/m) measured with p-polarized light at an incidence angle of 40° (solid line) compared to a simulated spectrum of an α-helix lying flat at the interface (dashed line).

The spectra were simulated with a program based on the formalism of Kuzmin and Michailov [227], written by Dr. Annabel Edwards.

VIII.2 Secondary Structure Calculation with DICHROWEB

Even though every conformation shows special absorption bands, the estimation of the content of helices, sheets and turns is quite sophisticated. Some algorithms exist and are provided by the DICHROWEB [149; 150]. The database is based on the known structures of big proteins, which were resolved by NMR. The comparison with the measured spectrum gives the composition of the secondary structure of the sample.

With the help of the CONTINLL [165] algorithm, we obtain a 5.6% α-helical, 38.4% β-sheet, 22.0% turn and 33.9% unordered contribution for LL-20 and a 15.0% α-helical, 21.8% β-sheet, 27.0% turn and 36.1% unordered contribution for LL-32. The algorithm does not consider a possible oligomerization of the peptides, which can lead to changes in the spectra [152]. Additionally, the shading of aggregated peptides can lead to a signal decrease [153]. The CD spectra for the peptides in water are typical for an unstructured conformation [154], therefore the DICHROWEB results were not used for interpretation of the data.

VIII.3 Effect of SDS and CTAB on LL-20 and LL-32

The interaction of LL-20 and LL-32 with amphiphiles was also investigated. The influence of sodium dodecylsulfate (SDS) and cetyltrimethylammonium bromide (CTAB) solutions, both below and above the critical micelle concentration (cmc), was analysed by circular dichroism spectroscopy (CD)[9].

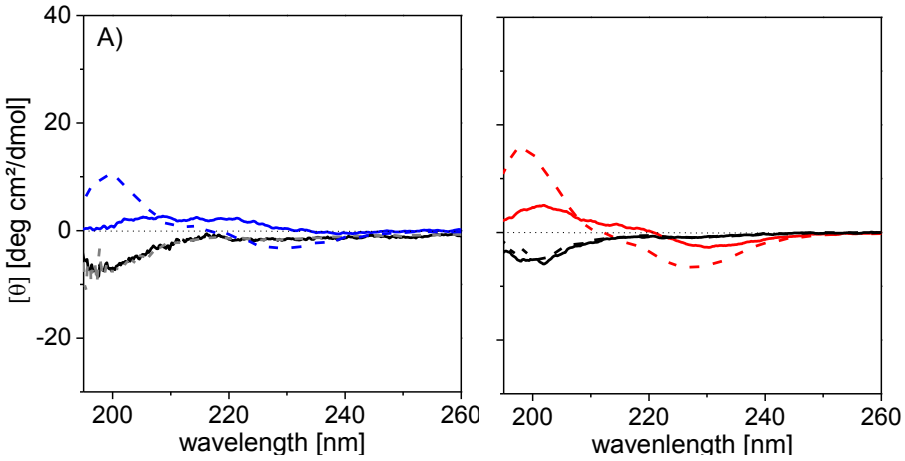

Figure A2: CD spectra of the peptides mixed with amphiphiles
A) LL-20 (- - -), LL-20/CTAB (—), LL-20/SDS below the cmc (—), LL-20/SDS above the cmc (- - -)
B) LL-32 (- - -), LL-32/CTAB (—), LL-20/SDS below the cmc (—), LL-32/SDS above the cmc (- - -).
Measurements were done in water at 20°C, 63 µM peptide in solution.

Neither the presence of CTAB monomers nor CTAB micelles had an effect on the secondary structure of the peptides (Figure A2). There is no change in the spectra compared to those in water. An increased noise level below 200 nm is due to the absorption of bromide (counterion in CTAB) and could not be eliminated by subtraction of the CD spectrum of the corresponding surfactant solution. For both peptides, an unspecific signal was detected when the peptides were in contact with SDS monomers. This loss of signal is the result of an irregular aggregation of the peptide with SDS monomers, followed by sedimentation. Above the cmc SDS induced a change in the CD spectra of LL-20 and LL-32 with a positive band at 200 nm and a small, but broad band at 230 nm. There is equilibrium of micelles and monomers in solution at the used SDS concentration of 15 mM. We expect an α-helical conformation for the peptide when in contact with SDS micelles, because CD measurements with POPG vesicles revealed a mainly α-helical conformation of both peptides. Therefore, we assume that the measured spectrum is a superposition of two spectra: An unspecific spectrum, as found for the peptides interacting with

[9] Sodium dodecylsulfate (SDS) was purchased from Sigma-Aldrich (Germany) and used in concentrations of 5 mM and 15 mM, respectively. Cetyltrimethylammonium bromide (CTAB) was obtained from Fluka (Germany) and used in concentrations of 0.5 and 1.5 mM, respectively.

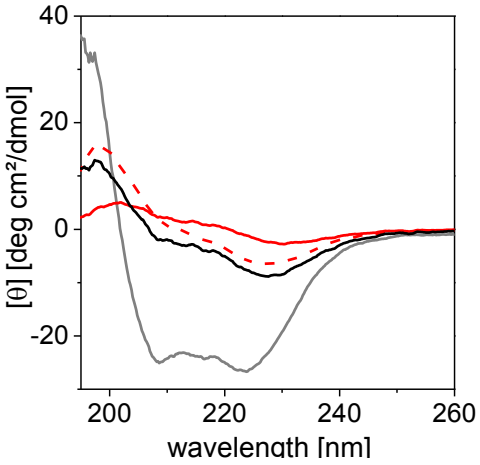

Figure A3: Simulation of the CD spectrum of LL-32/SDS above the cmc.
The best fit (—) to the measurement (- - -) is shown together with the spectrum of LL-32 bound to POPG vesicles (—) and and to SDS below the cmc (—). Measurements were done in water at 20°C.

SDS monomers, and an α-helical spectrum for the peptides interacting with SDS micelles. To proof this, I simulated the spectra by interfering the spectra of the helical and the aggregated LL-32 in different ratios. The best fit is shown in Figure A3 and was obtained by

Fit= 0.22((spectrum of helical LL-32)+6(spectrum of aggregated LL-32))

The factor of 0.22 correlates with a reduced the intensity of a spectrum by the shading of the aggregates [153]. This aggregation effect was not observed for other antimicrobial peptides, e.g Ar-2 [228], the α-helical porcine-derived NK-2 [31] or other CAP-derived peptides [229] and even LL-37, leaving an explanation open.

VIII.4 Isotherms

The pressure/area isotherm of DPPG is not shown in the chapters, so it is presented here in Figure A4. The isotherms of DPPC, DOPC and the mixtures with SM and DOPS are shown in chapter 5.

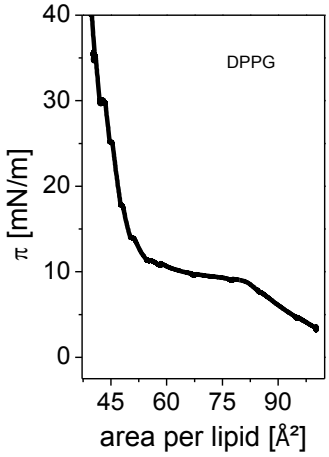

Figure A4: Isotherm of DPPG (5 mM HEPES, 100 mM NaCl, pH 7.4, 20°C).

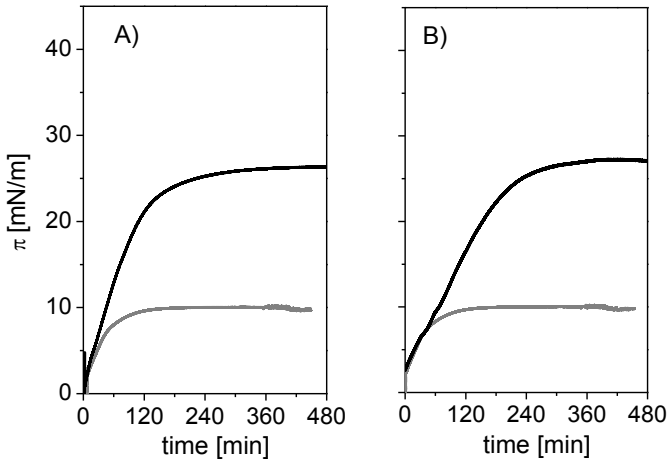

Figure A5: Time-dependent surface pressure π upon adsorption of LL-32 (—) and LL-20 (—) to A) DOPC/SM (50:50) and B) DOPC/SM/DOPS (45:45:10) monolayers.
(5 mM HEPES, 100 mM NaCl, pH 7.4, 20°C, 0.2 µM peptide in solution).

VIII.5 GIXD Data and Calculated Lattice Parameters

The position of the Bragg peak maxima Q_{xy} and Bragg rod maxima Q_z are listed in the tables below. The corresponding FWHM is denoted with ΔQ_{xy} and ΔQ_z, respectively. From these values, the lattice parameters and tilt angles were calculated. π is the surface pressure; a, b, and c are the length of the unit cell vector; α,β, and γ are angles between this vectors. A_0 is the in-plane area of one alkyl chain; A_{xy} is the projected area of the alkyl chain on the water surface. L_{xy} indicates the in-plane correlatiobn length, L_z the thickness of the scattering molecule.

Table A1: Maximum positions and FWHM of the Bragg peaks and Bragg rods for DPPC.

π [mN/m]	Q_{xy} [Å^{-1}]	ΔQ_{xy} [Å^{-1}]	Q_z [Å^{-1}]	ΔQ_z [Å^{-1}]
15	1.460	0.012	0	0.370
	1.309	0.068	0.783	
20	1.464	0.012	0	0.370
	1.320	0.067	0.768	
25	1.466	0.012	0	0.370
	1.338	0.064	0.705	
30	1.469	0.013	0	0.370
	1.355	0.053	0.705	
35	1.469	0.013	0	0.370
	1.362	0.073	0.727	

Table A2: Maximum positions and FWHM of the Bragg peaks and Bragg rods for DPPC/peptide mixed films.

	π [mN/m]	Q_{xy} [Å^{-1}]	ΔQ_{xy} [Å^{-1}]	Q_z [Å^{-1}]	ΔQ_z [Å^{-1}]
DPPC, LL-20	10	1.456	0.014	0	0.370
		1.290	0.056	0.662	
	30	1.465	0.015	0	0.370
		1.349	0.053	0.643	
DPPC, LL-32	26	1.462	0.058	0	0.370
		1.337	0.115	0.720	
	30	1.468	0.013	0	0.370
		1.365	0.055	0.668	

Table A3: Calculated lattice parameters and tilt angles for DPPC.

π [mN/m]	a,b [Å]	distortion	tilt	α, β	A_{xy} [Å^2]	A_0 [Å^2]	L_{xy} [Å]	L_z [Å]
15	5.78	0.150	35.8°	112.2	24.9	20.2	620.9	14.9
	5.18			123.9			81.9	
20	5.72	0.142	35.0°	112.6	24.5	20.1	669.1	14.9
	5.16			123.7			82.9	
25	5.61	0.125	32.2°	113.6	24.1	20.4	628.7	14.9
	5.12			123.2			87.0	
30	5.52	0.110	31.8°	114.3	23.6	20.1	541.8	14.9
	5.01			122.8			105.5	
35	5.48	0.103	32.4°	114.7	23.4	19.8	517.5	14.9
	5.08			122.6			76.2	

Table A4: Calculated lattice parameters and tilt angles for DPPC/peptide mixed films.

	π [mN/m]	a,b [Å]	distortion	tilt	α, β	A_{xy} [Å^2]	A_0 [Å^2]	L_{xy} [Å]	L_z [Å]
DPPC, LL-20	10	5.90	0.167	31.9°	111.3	25.5	21.6	480.6	14.9
		5.22			124.4			100.7	
	30	5.55	0.114	29.6°	114.1	23.8	20.7	435.5	14.9
		5.11			122.9			104.9	
DPPC, LL-32	26	5.61	0.123	32.8°	113.7	24.2	20.3	669.1	14.9
		5.13			123.2			96.3	
	30	5.46	0.099	30.1°	114.9	23.4	20.2	541.8	14.9
		5-08			122.5			101.6	

Table A5: Maximum positions of the Bragg peaks and Bragg rods for DPPG/peptide mixed films.

	π [mN/m]	Q_{xy} [Å^{-1}]	Q_z [Å^{-1}]
DPPG	30	1.470	0.032
		1.389	0.541
		1.361	0.627
	40	1.479	0.038
		1.425	0.499
		1.402	0.617
DPPG, LL-20	28	1.475	0.001
		1.433	0.442
		1.407	0.562
DPPG, LL-32	38	-	-

Table A6: Calculated lattice parameters and tilt angles for DPPG.

	π [mN/m]	a,b,c [Å]	distortion	tilt	α, β,γ	A_{xy} [Å^2]	A_0 [Å^2]
DPPG	30	5.00	0.093	26.9°	123.2	23.1	20.6
		5.11			121.4		
		5.41			115.4		
	40	4.94	0.064	25.2°	122.3	22.2	20.0
		5.03			120.8		
		5.22			116.9		
DPPG, LL-20	28	4.94	0.055	22.9°	122.1	22.1	20.3
		5.03			120.4		
		5.18			117.4		
DPPG, LL-32	38	0	-	-		-	-

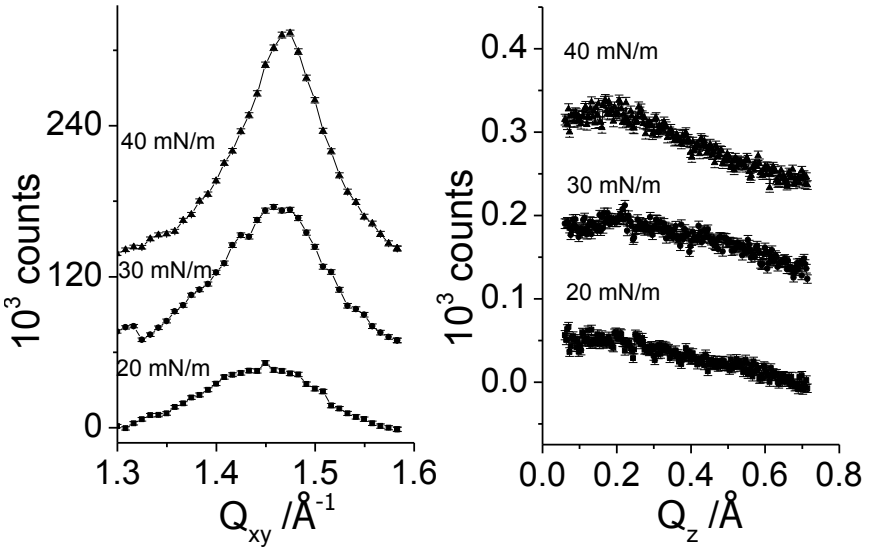

Figure A6: Background subtracted Bragg peaks (left) and Bragg rods (right) for SM.

Table A7: Maximum position and FWHM of the Bragg peaks and Bragg rods for SM.

π [mN/m]	Q_{xy} [Å^{-1}]	ΔQ_{xy} [Å^{-1}]	Q_z [Å^{-1}]	ΔQ_z [Å^{-1}]
20	1.416	0.131	0.537	0.185
	1.472	0.106	0.205	
30	1.456	0.098	0.477	0.200
	1.487	0.064	0.209	
40	1.418	0.237	0.422	0.171
	1.471	0.089	0.166	

Table A8: Calculated lattice parameters and tilt angles for SM.

π [mN/m]	a,b [Å]	distortion	tilt	α, β	A_{xy} [Å^2]	A_0 [Å^2]	L_{xy} [Å]	L_z [Å]
20	4.87	0.051	20.9°	122.5	21.6	20.2	74.1	29.8
	5.06			118.7			37.6	
30	4.85	0.028	18.1°	122.4	20.9	19.9	87.4	27.6
	4.95			119.3			56.7	
40	4.87	0.0483	18.4°	122.4	21.6	20.5	62.4	27.4
	5.05			118.8			23.3	

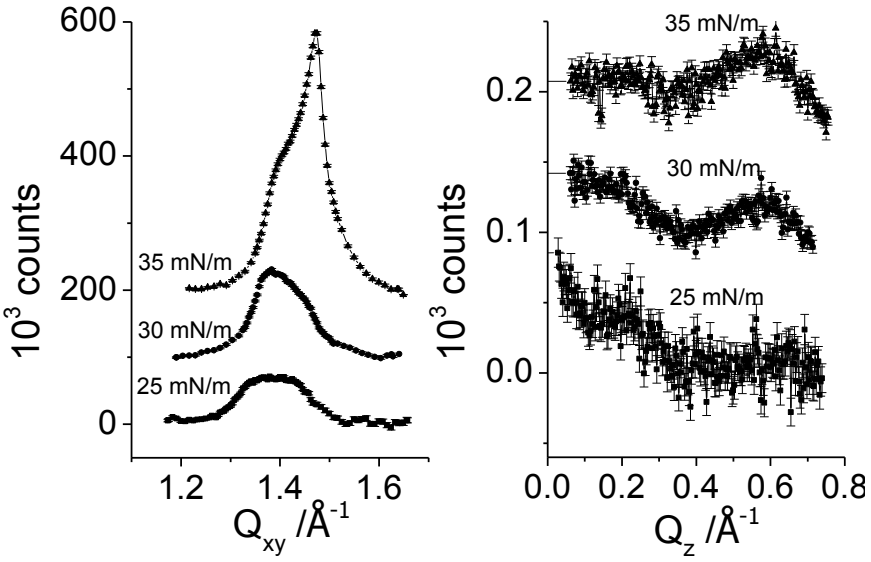

Figure A7: Background subtracted Bragg peaks (left) and Bragg rods (right) for mixed films of DPPC/SM (50:50).

Table A9: Maximum position and FWHM of the Bragg peaks and Bragg rods for mixed films of DPPC/SM.

π [mN/m]	Q_{xy} [Å^{-1}]	ΔQ_{xy} [Å^{-1}]	Q_z [Å^{-1}]	ΔQ_z [Å^{-1}]
25	1.472	0.036	0	0.334
	1.454	0.114	0.251	
	1.352	0.093	0.625	
30	1.470	0.034	0	0.334
	1.447	0.164	0.187	
	1.376	0.076	0.581	
35	1.474	0.028	0	0.334
	1.453	0.105	0.219	
	1.393	0.056	0.581	

Table A10: Calculated lattice parameters and tilt angles for mixed films of DPPC/SM.

π [mN/m]	a,b,c [Å]	distortion	tilt	α, β, γ	A_{xy} [Å^2]	A_0 [Å^2]	L_{xy} [Å]	L_z [Å]
25	4.84	0.011	24.9°	124.9	22.5	20.4	157.4	16.4
	5.21			118.2			48.6	
	5.27			116.8			59.6	
30	4.89	0.078	23.2°	123.7	22.3	20.5	166.5	16.4
	5.14			119.0			33.7	
	5.22			117.5			73.1	
35	4.88	0.070	22.8°	123.2	22.0	20.3	206.2	16.4
	5.09			119.2			52.6	
	5.17			117.7			100.5	

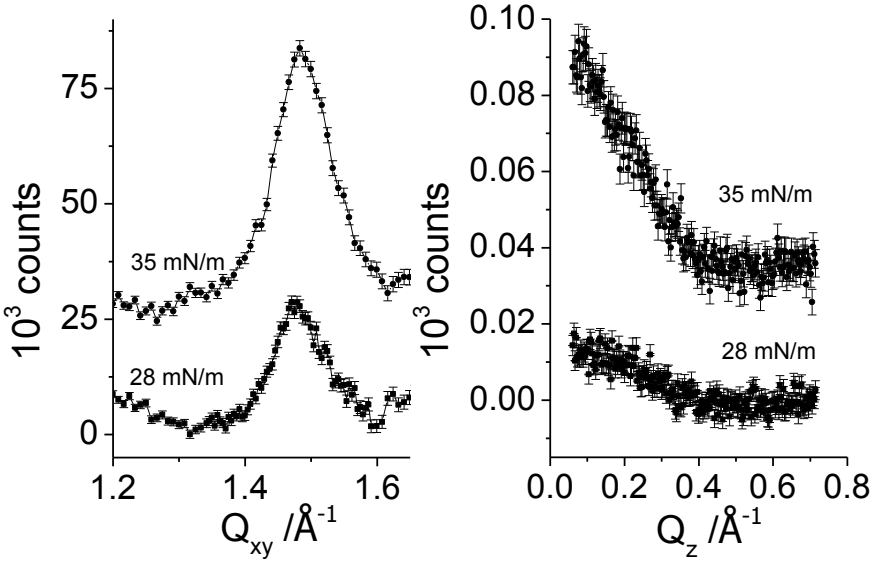

Figure A8: Background subtracted Bragg peaks (left) and Bragg rods (right) for mixed films of DPPC/SM (50:50) and LL-32.

Table A11: Maximum positions and FWHM of the Bragg peaks and Bragg rods for mixed films of DPPC/SM and LL-32.

π [mN/m]	Q_{xy} [Å^{-1}]	ΔQ_{xy} [Å^{-1}]	Q_z [Å^{-1}]	ΔQ_z [Å^{-1}]
28	1.516	0.102	0	0.238
	1.472	0.076	0.183	
35	1.506	0.115	0	0.238
	1.477	0.090	0.188	

Table A12: Calculated lattice parameters and tilt angles for mixed films of DPPC/SM and LL-32.

π [mN/m]	a,b [Å]	distortion	tilt	α, β	A_{xy} [Å^2]	A_0 [Å^2]	L_{xy} [Å]	L_z [Å]
28	4.98	0.040	8.3°	118.0	20.6	20.4	54.3	23.2
	4.83			121.0			73.1	
35	4.95	0.026	8.4°	118.7	20.6	20.4	48.2	23.2
	4.85			120.7			61.7	

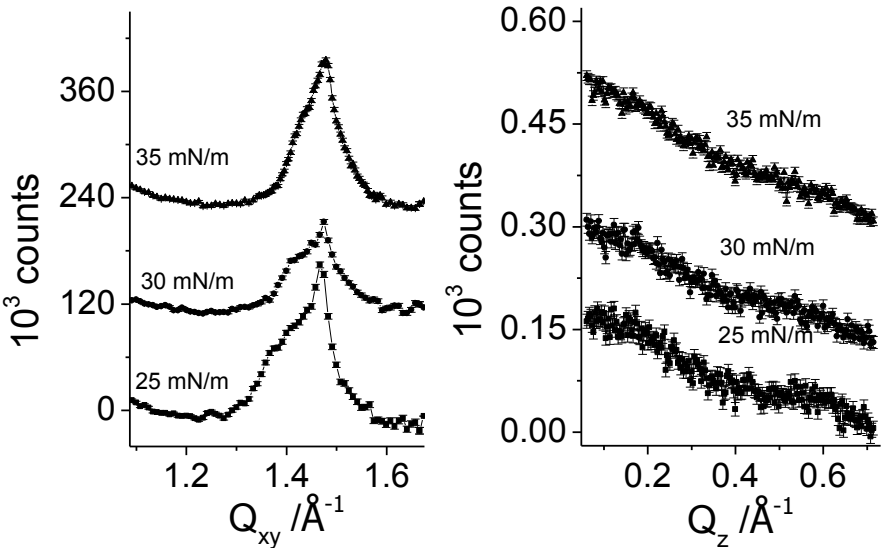

Figure A9: Background subtracted Bragg peaks (left) and Bragg rods (right) for mixed films of DPPC/SM/DOPS (45:45:10).

Table A13: Maximum position and FWHM of the Bragg peaks and Bragg rods for mixed films of DPPC/SM/DOPS.

π [mN/m]	**Q_{xy} [Å^{-1}]**	**ΔQ_{xy} [Å^{-1}]**	**Q_z [Å^{-1}]**	**ΔQ_z [Å^{-1}]**
25	1.470	0.033	0.161	0.251
	1.417	0.148	0.580	
30	1.471	0.050	0.134	0.274
	1.412	0.077	0.578	
35	1.475	0.070	0.139	0.271
	1.425	0.049	0.582	

Table A14: Calculated lattice parameters and tilt angles for mixed films of DPPC/SM/DOPS.

π [mN/m]	**a,b [Å]**	**distortion**	**tilt**	**α, β**	**A_{xy} [Å^2]**	**A_0 [Å^2]**	**L_{xy} [Å]**	**L_z [Å]**
25	4.88	0.048	22.2°	122.4	21.6	20.0	214.3	22.0
	5.06			118.8			37.5	
30	4.86	0.053	22.3°	122.6	21.7	20.1	111.9	20.1
	5.07			118.7			72.3	
35	4.86	0.046	22.2°	122.2	21.5	19.9	115.1	20.4
	5.04			118.9			79.3	

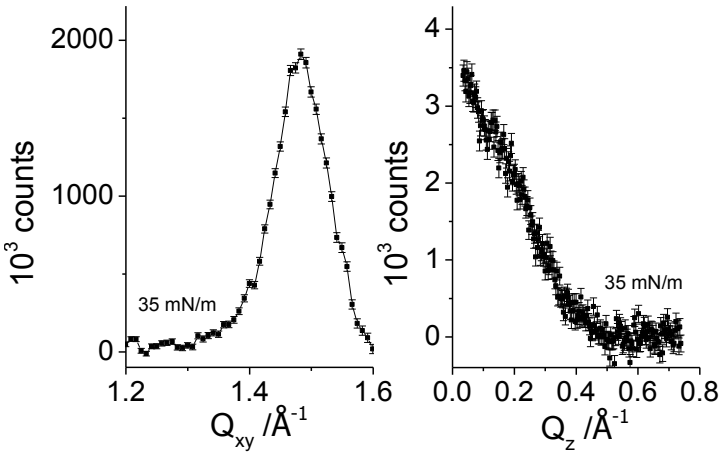

Figure A10: Background subtracted Bragg peaks (left) and Bragg rods (right) for mixed films of DPPC/SM/DOPS (45:45:10) and LL-32 at π = 35 mN/m.

Table A15: Maximum position and FWHM of the Bragg peaks and Bragg rods for mixed films of DPPC/SM/DOPS and LL-32.

π [mN/m]	Q_{xy} [Å^{-1}]	ΔQ_{xy} [Å^{-1}]	Q_z [Å^{-1}]	ΔQ_z [Å^{-1}]	π [mN/m]
23	-	-	-	-	-
35	1.520	0.056	0	0.202	0.238
	1.475	0.101	0.194		

Table A16: Calculated lattice parameters and tilt angles for mixed films of DPPC/SM/DOPS and LL-32.

π [mN/m]	a,b [Å]	distortion	tilt	α, β	A_{xy} [Å^2]	A_0 [Å^2]	L_{xy} [Å]	L_z [Å]
23	-	-	-	-	-	-	-	-
35	4.97	0.04	8.7°		20.5	20.3	100.3	23.2
	4.82						54.9	

VIII.6 IRRA Spectra

In order not to reduce the number of graphics in the chapter to the most informative ones, some spectra were not shown. They are shown here.

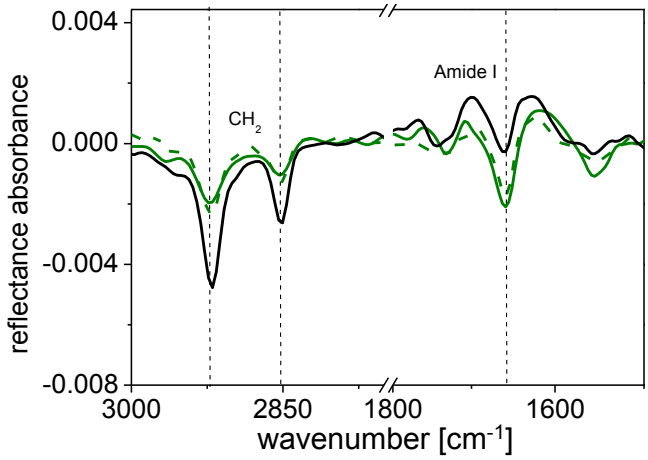

Figure A11: IRRA spectra of mixed films of DPPC/SM/ LL-32 at π_{eq} = 26 mN/m (—), π_1 = 30 mN/m (- - -) and π_2 = 35 mN/m (—).

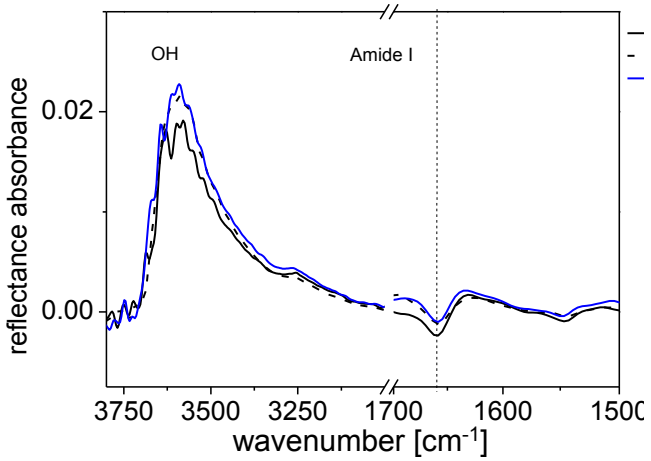

Figure A12: IRRA spectra of mixed DOPC/SM/LL-32 films at π_{eq} = 26 mN/m) (—) and π_1 = 30 mN/m (---) and π_2 = 35 mN/m (—). The compression of the film does not lead to a complete squeeze-out of the peptide, since the OH-band intensity is comparable to the straight lipid film and amide bands are still present.

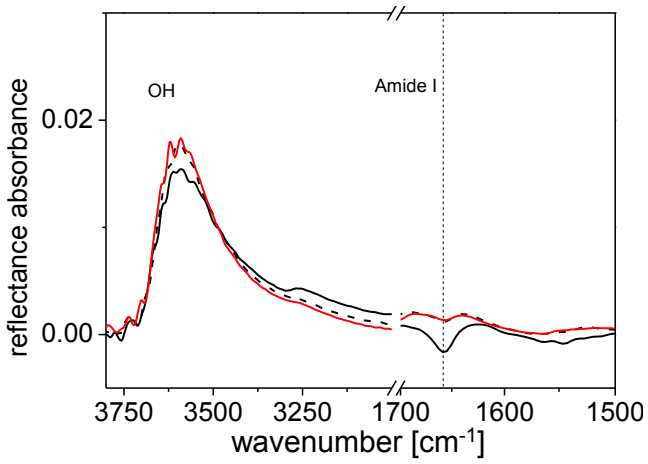

Figure A13: IRRA spectra of mixed DOPC/SM/DOPS/LL-32 films at π_{eq} = 26 mN/m (—), π_1 = 30 mN/m (- - -) and π_2 = 35 mN/m (—). The compression of the film does not lead to a complete squeeze-out of the peptide, since the OH-band intensity is comparable to the pure lipid film and amide bands are still present.

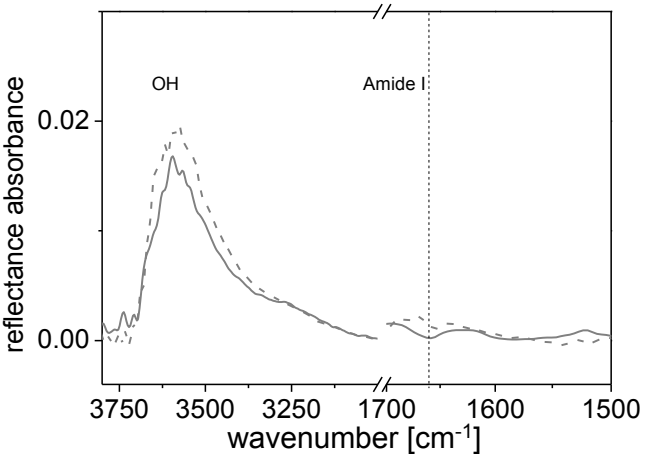

Figure A14: IRRA spectra of mixed DOPC/SM/LL-20 films at π_{eq} = 10 mN/m (—) and π_1 = 25 mN/m (- - -). The compression of the film leads to a squeeze-out of the peptide, since the amide I band intensity almost vanishes

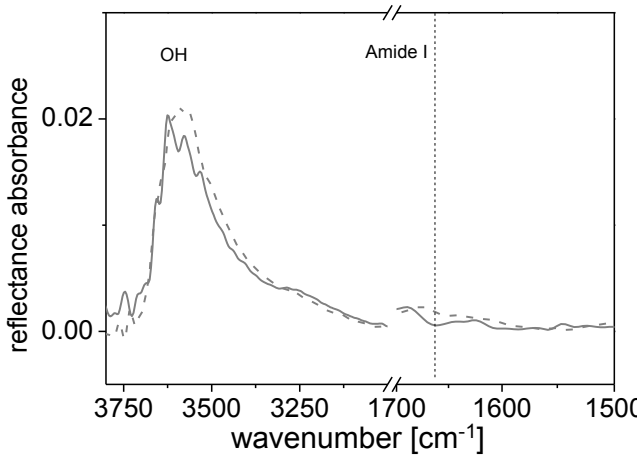

Figure A15: IRRA spectra of DOPC/SM/DOPS/LL-20 mixed films at π_{eq} = 10 mN/m) (—) and π_1 = 25 mN/m (- - -). The compression of the film leads to a squeeze-out of the peptide, because the amide I band intensity almost vanishes

Danksagung

Ich möchte allen Menschen danken die mich sowohl direkt, als auch indirekt bei der Fertigstellung dieser Arbeit unterstürzt haben.

Zuerst möchte ich Prof. Dr. Helmuth Möhwald für die vielen wissenschaftlichen Ratschläge und Möglichkeit, die Arbeit am MPI für Kolloid-und Grenzflächenforschung anzufertigen, bedanken.

Prof. Dr. Gerald Brezesinski danke ich für die Bereitstellung des Themas, die vielen Diskussionen und die Unterstützung während der gesamten Zeit.

Prof. Dr. Thomas Gutsmann möchte ich für die Bereitstellung der Peptide und die zahlreichen Hinweise zur Biologie des Themas danken.

Irina Berndt möchte ich danken für die gute Laune und die Organisation der zwischenmenschlichen Dinge innerhalb der Gruppe. Nicht zuletzt möchte ich mich für die Unterstützung der Laborarbeit während meiner Schwangerschaft bedanken.

Für zahlreiche Diskussionen und Hilfe bei Messungen möchte ich mich bei Dr. Maria Hörnke, Dr. Oksana Travkova und Janos Keller bedanken. Außerdem bei Dorota Pawlowska dafür, dass ich ständig um Rat bei Problemen mit Origin und der Auswertung der Röntgendaten fragen konnte. Ich danke Dr. Matthias Kietzmann für die Hilfe an BW1.

I would like to thank my colleagues from the Brezesinski group, and especially the girl's office for a nice working atmosphere.

Ich danke Katharina Lemmnitzer für die Erklärung von NMR-Artikeln, Jonathan Brox für die Diskussion über eine mögliche Aggregation meiner Peptide.

Andreas Jaekel und Anne Bremer danke ich besonders für Vergleichsmessungen.

Für das Korrekturlesen *und die aufmunternden Worte* danke ich speziell Dr. Julia Schneider, Dr. Maria Hörnke und Agnieszka Gojzewska.

Für seelischen Beistand möchte ich ganz besonders meiner Familie und meinen Freunden danken. Außerdem Alexander Rettig fürs Rücken freihalten. Nicht zuletzt danke ich meinem Sohn Ruben für das abendliche Ablenken mit Feuerwehrbüchern und viel Speiseeisssss.

Namaste.

.

Eigenständigkeitserklärung

Hiermit versichere ich die vorliegende Arbeit selbstständig und lediglich unter Verwendung der genannten Quellen und Hilfsmittel angefertigt zu haben. Die Arbeit wurde an keiner weiteren Hochschule als Dissertation eingereicht. Die gültige Promotionsordnung habe ich zur Kenntnis genommen.

Potsdam, April 2013